Metal Surface Tolerant Conformal Low-Profile Plastic Embedded Antennas for Automotive Applications

Doctoral thesis
for attaining the academic degree of

Doctor of Engineering (Dr. -Ing.)

presented to the Faculty of Electrical Engineering and Information Technology
Technische Universität Ilmenau

by M.Sc. Jasmeet Singh

1. Reviewer: Univ.-Prof. Dr. rer. nat. habil. Matthias A. Hein
2. Reviewer: Prof. Dr.-Ing. Matthias Geissler
3. Reviewer: Univ.-Prof. Dr. Jan Hesselbarth

Submitted on: 15.07.2022
Defended on: 13.04.2023

DOI: 10.22032/dbt.57612
URN: urn:nbn:de:gbv:ilm1-2023000163

Acknowledgements

This work was carried out at the RF and Microwave Research Group at the Technische Universität Ilmenau, as a part of the projects "Kunststoff-basierte integrierte KFZ-Antennen" (KUBINKA) and "Smarte integrierte Funksysteme für vernetzte Mobilität und Logistik" (SISYVOS). These projects were funded by the Federal State of Thuringia, the Thüringer Aufbaubank, and the European Regional Development Fund (EFRE) under the grants 2015 FE 9042 and 2018 FE 9031.

I would like to extend my heartiest gratitude to my doctoral adviser Univ.-Prof. Dr. rer. nat. habil. Matthias Hein for providing me the opportunity to work on these exciting, industry-relevant projects related to automotive antenna design and measurements. We had many interesting discussions over the years, and his encouragement, insightful and practical suggestions, and overall excellent guidance is a major factor behind the successes presented in this doctoral work.

I am also especially indebted to Dr.-Ing. Ralf Stephan; his ever-enthusiastic guidance, understanding and support were paramount to the successes achieved in this work. The support and cooperation of our industry partners WIEGAND and Antennentechnik Bad Blankenburg was also indispensable to the progress of this work, for which I am grateful as well.

I would like to thank Prof. Dr.-Ing Matthias Geissler and Univ.-Prof. Dr. Jan Hesselbarth for kindly accepting to be the external reviewers of my thesis, and Prof. Dr. rer. nat. Jochen Seitz, Univ.-Prof. Dr.-Ing. Giovanni Del Galdo, and Dr.-Ing. Christian Bornkessel for accepting to be the additional required members of the doctoral commission.

For the development of many of my antenna prototypes over the last years, and the preparation of the antenna measurement lab (AML) for their measurement, I would like to express my gratefulness to Mr. Michael Huhn. My thanks goes also to Dr.-Ing. Tobias Nowack for his invaluable help with setting up the measurements in the "virtual road simulation and test area" (VISTA).

I also had great pleasure of working with wonderful, supportive and motivated colleagues in our group. In particular, I would like to thank Philipp Berlt, Berk Altinel, Sreehari Buddappagari Jayapal Gowdu, Muhammad Ehtisham Asghar, Syed Naser Hasnain, and Umais Tayyab for the interesting technical conversations and exchange of knowledge.

Lastly, I would like to thank my family and friends for their support, encouragement, and unwavering belief in my abilities.

Jasmeet Singh
Hildesheim, 17.06.2023

Declaration/Erklaerung

I confirm that I have carried out this thesis without the unauthorised assistance of third parties and without the use of other than the stated aids. Data and concepts taken directly or indirectly from other sources have been duly cited. For the creation and evaluation of the following material, the persons/sources listed below have assisted me in the manner described in each case, without any payment:

1. This doctoral thesis were performed under the guidance of Univ.-Prof. Dr. rer. nat. habil. Matthias Hein and Dr.-Ing. Ralf Stephan.
2. Michael Huhn set up the antenna measurement lab (AML) for the radiation pattern measurements of the bare and car door frame integrated versions of the antennas presented in this thesis. He was also responsible for the in-house printing of the di-patch antenna and the multiband patch antenna samples.
3. Dr-Ing. Tobias Nowack assisted in setting up the virtual road simulation and test area (VISTA) for the antenna far-field measurements including the car.
4. The in-house antenna measurement data processing tool, ADAPT, developed by Muhammad Ehtisham Asghar was used to extract the radiation patterns and antenna efficiencies from the AML and VISTA measurement data.
5. Philipp Berlt helped with the set up of the LTE MIMO data rate measurements in VISTA, presented in the subsection 6.3.1 of chapter 6 of this thesis. He was also kind enough to provide the scripts necessary for evaluating the data obtained from these measurements.
6. The project partners at Wiegand were responsible for embedding the antenna samples into the B-column plastic covers of the car.
7. The project partners at Antennentechnik Bad Blankenburg performed the LTE MIMO data rate field tests discussed in subsection 6.3.2 of chapter 6.
8. The V2V communication field tests discussed shortly in section 6.4 of chapter 6 were conducted in collaboration with Berk Altinel. He supported with the measurement set up and also provided the scripts necessary for evaluating the field test results.

No other persons were involved in the composition of the content or material of this thesis. In particular, I have not made use of the paid assistance of intermediary or advisory services (doctoral consultants or other persons). No one has received from me, directly or indirectly, any pecuniary benefits for any work in connection with the content of the dissertation submitted.

This thesis has not been submitted before this point to an examination authority in the same or a similar form, either in Germany or abroad. I have been informed that the incorrectness of the above declaration will be assessed as an attempted deception and will result in the termination of the doctoral examination procedure in accordance with § 7 Para. 10 of the doctoral regulations.

Jasmeet Singh
Hildesheim, 17.06.2023

Abstract

With a rapid increase in the number of wireless services, and the utilization of antenna diversity techniques to achieve enhanced data rates or service reliability, the number of antennas that need to be installed in passenger cars is not insignificant any more, and only sees a rising trend. At the same time, finding suitable mounting locations for these antennas has become ever more challenging, because the number of such locations on a car has not grown parallelly to the number of antennas that need to be installed; cars are still mostly metal boxes, with a few plastic parts and the glass windows that allow for antenna integration. While most of these parts have already been utilized for embedding antennas, the plastic parts that were overlooked till now were the B-column plastic covers. In addition to highlighting the advantages of using the B-column plastic covers as an antenna embedding location over other locations, this work takes a comprehensive look into the challanges associated with the same, specifically the limited space for antenna integration and the close proximity of the embedded antenna to the car metal chassis. The latter introduces a strong electromagnetic coupling between the antenna and the car body, consequently impacting antenna properties like impedance matching and realized gain. The upcoming chapters present the underlying design principles, theory, and measurements of novel, low-profile, conformal and metal surface tolerant mobile communications antennas, namely, the single band di-patch antenna and a co-planar stacked microstrip line coupled multi-band antenna, that suitably address and overcome the aforementioned challenges. Additionally, a high impedance surface based dipole antenna solution is also presented in the later half of this thesis. The simulation and measurement results of the bare and the integrated versions of the presented antennas, including LTE-MIMO data rate measurements presented in the penultimate chapter, not only speak for the suitability of these antennas for low-profile, close-to-metal surface applications in general, but also show that the B-column plastic covers present a highly suitable new antenna integration location for automotive mobile communications applications.

Kurzfassung

Mit der rasanten Zunahme drahtloser Dienste und dem Einsatz von Antennendiversitätstechniken zur Erzielung höherer Datenraten oder Dienstzuverlässigkeit ist die Zahl der in Pkw zu installierenden Antennen nicht mehr unbedeutend und nimmt weiter zu. Gleichzeitig wird es immer schwieriger, geeignete Montageplätze für diese Antennen zu finden, da die Zahl der Montageplätze im Auto nicht parallel zur Zahl der zu installierenden Antennen gewachsen ist; Autos sind nach wie vor meist Metallkästen, mit einigen wenigen Kunststoffteilen und Glasscheiben die die Integration von Antennen ermöglichen. Die meisten dieser Teile wurden bereits zu diesem Zweck verwendet, die B-Säulen-Kunststoffabdeckungen wurden jedoch bisher nicht für die Antennenintegration berücksichtigt. In dieser Arbeit werden nicht nur die Vorteile der B-Säulen-Kunststoffabdeckungen als An-tenneneinbauort gegenüber anderen Orten hervorgehoben, sondern auch die damit verbundenen Herausforderungen untersucht, insbesondere der begrenzte Platz für die Antennenintegration und die unmittelbare Nähe der eingebauten Antenne zum Metallchassis des Fahrzeugs. Letzteres führt zu einer starken elektromagnetischen Kopplung zwischen der Antenne und der Fahrzeugkarosserie, was sich auf die An-tenneneigenschaften wie Impedanzanpassung und realisierten Gewinn auswirkt. In den folgenden Kapiteln werden die zugrundeliegenden Entwurfsprinzipien, die Theorie und die Messungen neuartiger, flacher, konformer und metalloberflächentoleranter Mobilfunkantennen vorgestellt, nämlich die Einzelband-Di-Patch-Antenne und eine koplanar gestapelte, mit Mikrostreifenleitungen gekoppelte Multibandantenne, die die oben genannten Herausforderungen adressieren und überwinden. Zusätzlich wird in der zweiten Hälfte dieser Arbeit eine high impedance surface basierte Dipolantennenlösung vorgestellt. Die Simulations- und Messergebnisse der nicht integrierten und der integrierten Versionen der vorgestellten Antennen, einschließlich der LTE-MIMO-Datenratenmessungen, die im vorletzten Kapitel vorgestellt werden, sprechen nicht nur für die Eignung dieser Antennen für flache, metallnahe Oberflächenanwendungen im Allgemeinen, sondern zeigen auch, dass die B-Säulen-Kunststoffabdeckungen einen sehr geeigneten neuen Antennenintegrationsort für mobile Kommunikationsanwendungen im Automobil darstellen.

Contents

List of Abbreviations/Symbols

3GPP	3rd generation partnership project
ABS	acrylonitrile butadiene styrene
AML	antenna measurement lab
AUT/DUT	antenna under test/device under test
CDMA	code division multiple access
CQI	channel quality indicator
C-V2X	cellular-vehicle to everything communication
DL/UL	downlink/uplink
EMC	electromagnetic compatibility
ETSI	european telecommunications standards institute
FEM	finite element method
GPS	global positioning system
HIS	high impedance surface
HSPA	high speed packet access
IoT	internet of things
ITS-G5	intelligent transport systems
LTE	long term evolution
MIMO	multiple input multiple output
MLFMM	multi-level fast multi-pole method
OTA	over-the-air
PIFA	planar inverted F antenna
PMMA	polymethyl methacrylate
QAM	quadrature amplitude modulation
QPSK	quadrature phase shift keying
RFID	radio frequency identification
SINR	signal-to-interference-plus-noise-ratio
SISO	single input single output
TDMA	time division multiple access
UMTS	universal mobile telecommunications system
V2V	vehicle to vehicle communication
V2X	vehicle to everything comunication
VISTA	virtual road simulation and test area
WAVE	wireless access in vehicular environment
WLAN	wireless local area network

δ	dielectric loss angle (radians)
ϵ_r	relative permittivity
Ω	resistance (ohms)
λ_0	free-space wavelength (metres)

Chapter 1

Introduction

Today the saying that we live in a connected world almost sounds like a cliché, which is good, because, among other things, it is a testament to how far we have progressed in the field of communications technology; talking to friends and relatives across continents is as normal as drinking water, being aware of occurrences around the world in real-time is hardly surprising any more. One of the most exciting parts about it is that such connectivity is not limited to just within the confines of one's home, but is maintainable on-the-move as well. We progressed from telegraphy and fixed telephony to mobile phones and laptops quite a long time ago, and these enable us to be mobile as well as connected to the rest of the world at the same time. While the exchange of information between humans is one aspect, modern devices can also exchange useful information among themselves. For example, WiFi/bluetooth transfer of photos from a digital camera to a laptop, or commanding a networked smart speaker to turn on/off lights in one's home, and many of these tasks can be automated or scheduled so that the devices exchange the intended information with minimal further human intervention. Of course, people communicating on the move, or a smart speaker controlling a light bulb are things that happen wirelessly and the most fundamental link in any wireless communication chain is an antenna that performs the transformation between space waves and guided waves. Antennas have permeated a lot of our devices, and with the advent of the internet of things (IoT) era, the possibilities are only limited by our imagination.

The automotive sector has not remained untouched by the advancements in wireless communications either. We spend a sizeable chunk of our times commuting, and a lot of the digital services that we use in our daily lives have trickled down into the cabins of contemporary passenger cars. Cars are no longer just simple modes of transportation, and now contain a multitude of antennas to enable wireless access to a variety of infotainment and safety oriented services for the driver and the passengers, so much so that nowadays the lack/presence of many of these comforts is a deciding factor in the purchase of a new vehicle [1,2, 121]. These services are spread over a wide spectrum and include, but are not limited to, AM-radio reception at 0.5 MHz to radar based collision detection at 77 GHz [95]. The number of antennas in a car is actually larger than in any typical mobile phone, and new technologies like connected and automated driving coupled with 5G will further increase the demand for vehicular antennas, as may also be seen in the conclusion of [3]. Automotive antenna design is, therefore, a highly active field with its specific challenges. This work presents novel low-profile conformal plastic embedded antenna designs operational in the LTE and V2X frequency bands and thereby increases the repertoire of antenna choices available for automotive applications, particularly for challenging mounting locations wherein the antenna would lie parallel to and closely above the metal chassis of a car.

1.1 Automotive antennas: design trends, requirements, challenges

One may think that since cars are relatively large in size, finding mounting spaces for all of the current and the upcoming antennas would not pose a challenge. However, one factor that plays a key role in the purchase decision of a vehicle is its appearance; potential buyers want a car that is not only functional, but also looks stylish, sleek and aerodynamic. Nobody would like to purchase a car with a multitude of monopole antennas protruding from its roof. At the same time, antennas like rooftop monopoles are not robust, can be vandalized, and are exposed to the elements. Keeping in line with the desired aesthetics of a car, automotive antennas need to be conformal and low-profile, so that they may be embedded into/hidden behind the available plastic/glass parts in a typical passenger car. However, such locations, as indicated in Fig. 1.1 (a) and (b), are limited in number and are already occupied by a host of antennas. LTE-MIMO antennas are considered at the rear view mirror in [4], LTE and V2X antennas have been designed for the spoiler in [5,6], antennas for broadcast services like AM, FM, digital audio broadcast, TV and so on are usually embedded in the rear windscreen and the fixed side windows [7,8,9,10], broadcast, mobile communication, and RFID antennas have been designed for the side mirrors in [11,12], plastic bumpers are favoured locations for collision avoidance radars [13,14,15], and shark fin housings hide a variety of antennas including, but not limited to, LTE, AM/FM, V2X and GPS [16,17,18].

Furthermore, nearly all of the cases above use a diversity of antennas for each wireless service to ensure a near omnidirectional coverage around the car. This is because at locations other than the car rooftop, a single antenna is not sufficient for an omnidirectional coverage due to the blockage of the antenna radiation in certain directions by the car chassis. In such a case the SNR can be drastically reduced in the direction(s) of the pattern null(s). Secondly, Rayleigh fading in urban environments means that multiple copies of the same signal received by the single antenna may add destructively leading to deep fades in the signal reception. Using two antennas in spatially separated complementary locations, as exemplified in Fig. 1.1 (c), not only provides a nearly omnidirectional coverage, but as the signals arrive at these antennas through independently fading channels, techniques like switched combining or maximal-ratio combining may be employed to mitigate the effects of multipath fading. Fulfilling the diversity requirement further exacerbates the space crunch for car antennas, because an antenna installed on one side of a car for a particular wireless service would most likely be repeated at a complementary location on the opposite side.

The reader may also infer from the cited literature that due to the scarcely available possible/favourable installation locations, such locations end up incorporating a multiplicity of antennas for different wireless services; Fig. 1.1 (d) is a good example, and there are shark fin housings with an even larger number of antennas underneath them. The antenna designers are consequently faced with the challenge of maintaining suitable levels of isolation between these antennas, especially if these operate in closely spaced frequency bands, or if there is an overlap in the used frequency spectrum. This is in addition to the electromagnetic influence of the car chassis on the performance of these antennas, which needs to be accounted for in any case.

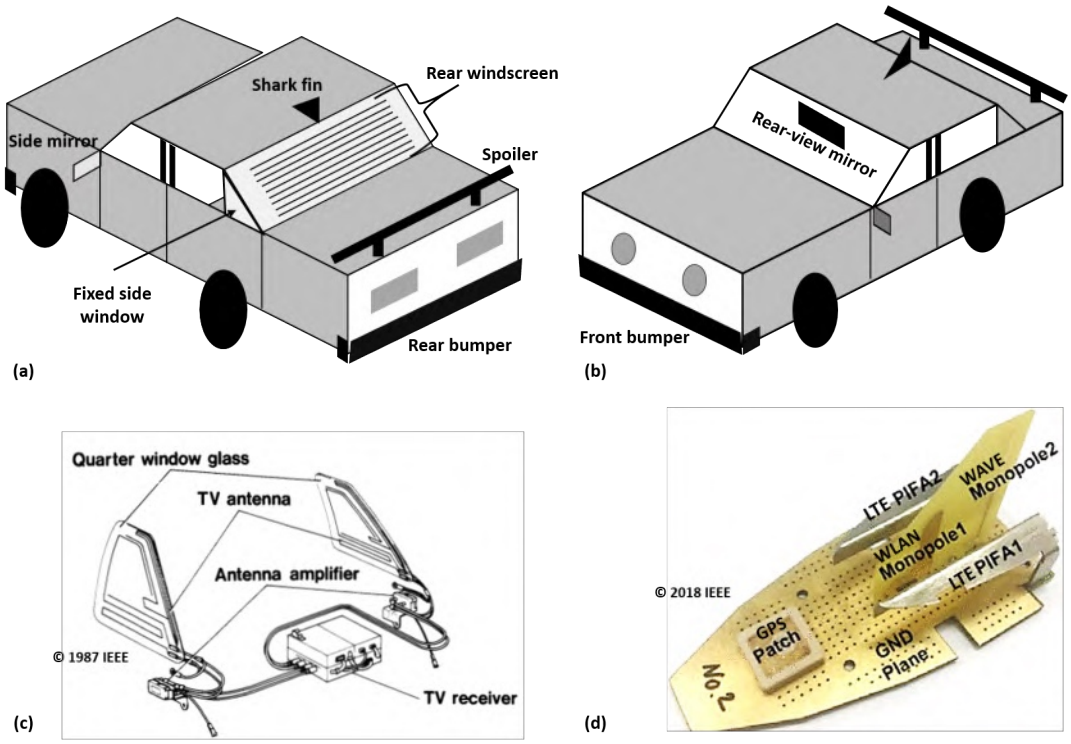

FIGURE 1.1: (a), (b): Typical antenna locations on a passenger car. (c) Diversity TV antennas printed on the opposing fixed side windows [10] ©1987 IEEE. (d) Examples of antennas hidden underneath a shark fin housing [18] ©2018 IEEE.

1.2 Motivation and aim of this work

It follows from the preceding discussion that finding new locations on a car for a conformal and hidden integration of antennas would be of utmost benefit. For one, this could allow for a redistribution of some of the antennas from the otherwise congested existing mounting locations, and secondly, and more importantly, we would simply have more room for antennas for future wireless services. If possible, the new location should satisfy two main characteristics:

(i) It would be favourable if the location already exists on typical cars, i.e., we do not have to modify the car structure to create this new location, which would be highly beneficial for car manufacturers from an economic standpoint, as they could continue using the existing car designs.

(ii) It should exist on complementary sides of a car, so that the requirements of diversity and a close to omnidirectional coverage around the car may be fulfilled.

At a first glance, it is difficult to imagine that there could be previously unused locations that fulfil these two characteristics, especially considering the breadth of all the locations that have been covered in the aforementioned literature. Herein come the B-column plastic covers found on all passenger cars, as illustrated in Fig. 1.2 for an Audi A1 - the car for which we designed our antennas. To the best of the author's knowledge and literature research, the exploitation of these plastic covers for a hidden integration of antennas was not considered before, perhaps because there are additional antenna design challenges associated with this location, in particular the proximity of the plastic covers to the car chassis. These challenges are addressed

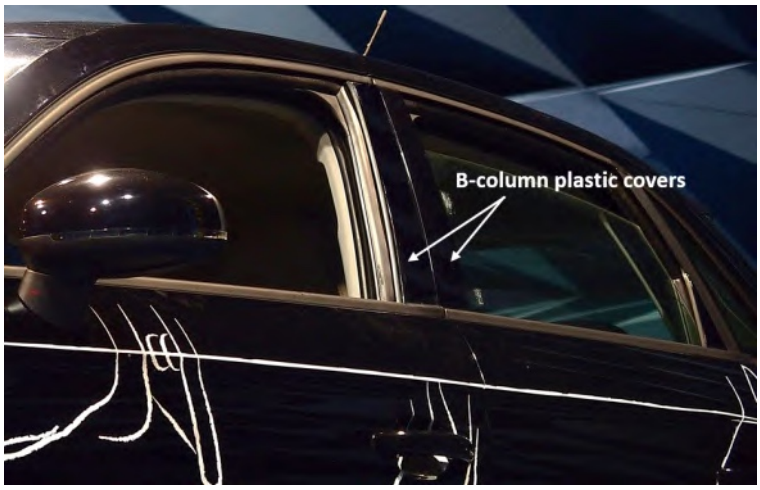

FIGURE 1.2: B-column plastic covers on an Audi A1.

comprehensively in the next chapters, but at this junction the important highlight is that the B-column plastic covers satisfy both the desirable characteristics mentioned before. That most of the cars have two of them on the driver and the passenger side forms a third advantage: the front plastic cover pair could integrate antennas for different wireless services compared to the back plastic cover pair.

The identification of this new antenna embedding location motivated the design of innovative antennas that could function irrespective of their extreme proximity to the car metal chassis at this location, rendering such plastic covers usable for future automotive wireless communication applications. This thesis presents both single-band and multi-band antenna designs, whereby the single band antennas were designed to be operational in the LTE-2600 band, 2.5...2.69 GHz, whereas the multi-band antenna covered the LTE/UMTS frequencies ranging from 1.71...2.69 GHz. These frequencies were chosen because of a few reasons enlisted ahead. For one, the necessary hardware to perform SISO/MIMO data rate measurements at these frequencies was available, so the antenna characterization would not remain limited to radiation pattern and reflection coefficient measurements. Secondly, although these are 4G frequencies, these would also be reused/refarmed for 5G; 5G has introduced additional frequency bands in the sub-6 GHz spectrum to meet the growing data rate needs, but will utilize the earlier allocated bands as well. Also, the antennas presented can simply be re-scaled to shift the frequency response as desired, important was to demonstrate that an appropriately designed antenna can function at this new mounting location.

1.3 Outline

- **Chapter 2: Background.** In this chapter, a short overview of the current mobile communications and V2X standards is provided, and their importance and usability is discussed, which further motivates our antenna design for these services. Moving onwards, a discussion on the choice of the B-column plastic cover as the antenna embedding location, and the repercussions of this choice for the antenna design and performance as opposed to the existing antenna mounting locations is presented. Thereafter, various available numerical simulation techniques are summarized along with their applicability, and the effect of the model complexity on the simulated results is elaborated. The chapter

concludes with an overview of the two antenna measurements facilities at our university that we used for characterizing the radiation performance of our antennas, namely, the antenna measurement lab (AML), and the virtual road simulation and test area (VISTA).

- **Chapter 3: Di-patch antenna.** This is the longest chapter in the thesis and concerns itself with the novel di-patch antenna that offers distinct advantages over a typical patch antenna, namely twice the impedance bandwidth, nearly half the total surface area, but no compromise of the achieved gain. The chapter opens with an interesting discourse on patch antenna equivalent modelling using half-wave electrical dipole antennas and half-wavelength folded electrical dipole antennas. This discussion leads on to the equivalent source modelling of the di-patch antenna, wherein the evolution of a di-patch antenna from a full-wavelength electrical dipole antenna above a ground plane is elucidated. This is followed by a sensitivity analysis of the di-patch antenna to small design parameter variations, as well as a characterization of its curvature tolerance to gauge its suitability for demanding conformal applications. Thereafter, the various simulation and measurement results of the di-patch antenna are compared, and the chapter is closed with an interesting simulation based comparison between a series-fed 1×2 di-patch array and patch array.

- **Chapter 4: Co-planar stacked microstrip line coupled multi-band patch antenna.** In this chapter another novel antenna design is presented, wherein through the combination of corner excitation and co-planar stacking of patches a multi-band antenna design covering the LTE-1800, UMTS-1900/2100, and LTE-2600 frequency bands was achieved. The design principle is explained in detail, before proceeding with sensitivity analysis of the antenna to design parameter variations. Thereafter the simulation and measurement results of the bare antenna and embedded antenna are discussed, concluding the chapter.

- **Chapter 5: High impedance surface based dipole antenna.** High impedance surfaces (HIS) present an attractive means to use half-wavelength electrical dipole antennas closely above metallic surfaces. The chapter begins with a concise introduction to the theoretical fundamentals of such surfaces. Following this, the simulation based design, sensitivity analysis to parametric variations, and curvature tolerance analysis of a HIS-dipole operational in the LTE-2600 band are considered. The chapter concludes with the comparisons of the simulated and measured results similar to the previous chapters.

- **Chapter 6: System aspects and LTE MIMO measurements.** The previous chapters focused on the design of three different antenna types suitable for operation closely above the car chassis, and each of these was embedded in one of the B-column plastic covers on the driver side. This chapter considers MIMO data rate measurements in the 1800 MHz LTE downlink (DL) band performed under semi-anechoic conditions in VISTA. For this two multi-band patch antennas from chapter 4 were embedded into two adjacent B-column plastic covers on the driver side, and one into the B-column plastic cover on the passenger side. The DL data rate obtained with the driver side antenna combination and the driver-passenger side antenna combination was compared to the reference data rate measured with two monopole antennas mounted at the centre of the car roof. The results were interpreted with the measured radiation patterns of the considered antennas in conjunction with multipath

effects in the measurement environment. Furthermore, the VISTA results were compared with the results from an independent field test with the same antenna set up on the car. In both the cases, the performance of the left side - right side embedded antenna combination was found to be comparable to the rooftop monopole antennas, which further enhanced the suitability of the B-columns for antenna integration. The chapter ends with a brief discourse on another field test conducted later on, but this time to judge the V2V performance of B-column integrated antennas. The conclusion here was the same, that B-columns are a promising location with respect to V2V performance as well.

- **Chapter 7: Conclusion and outlook.** The implications of the presented findings are discussed and some ideas are provided for future work.

1.4 List of the author's contributions

This work refers to and expands upon the author's patent and publications enlisted below. The numbers within the square brackets are the numbers at which these publications appear in the bibliography at the end of this thesis. Please note that no content from [129] has been presented in this thesis, as it did not fit within the framework of SISYVOS and KUBINKA. [32] has been fleetingly referred to in chapter 2, but no results from this publication have been presented or discussed in this thesis. [32] was based upon a master thesis work conducted under the author's supervision, and presents a 2 x 2 Ka-band patch antenna array that was embedded in the B-column plastic cover. For the interested reader, [32] provides an insight into the link budget requirements for car-to-LEO satellite communication, simulation and measurement results of the bare/plastic embedded array radiation pattern and reflection coefficient, as a well a simulation based analysis of the extent of beam steering achievable with the designed array.

Patent

- [53] "Strahlungselement", by J. Singh, M. A. Hein, R. Stephan. (2021, Oct. 28), Patent DE102017011225A1 [online]. Available: https://patents.google.com/patent/DE102017011225A1/de

Publications

1. [54] J. Singh, R. Stephan and M. A. Hein, "Low-Profile Wideband Differentially Fed Di-Patch Antenna Closely Above Metallic Ground", in *IEEE Antennas and Wireless Propagation Letters*, vol. 18, no. 5, pp. 976-980, May 2019, doi: 10.1109/LAWP.2019.2906825.

2. [94] J. Singh, R. Stephan and M. A. Hein, "Low-Profile Penta-Band Automotive Patch Antenna Using Horizontal Stacking and Corner Feeding", in *IEEE Access*, vol. 7, pp. 74198-74205, 2019, doi: 10.1109/ACCESS.2019.2919730.

3. [55] J. Singh, A. Neumann, T. Wack, T. Koppe, R. Stephan and M. A. Hein, "Novel conformal automotive di-patch antenna verified through car door frame measurements", *IET Conference Proceedings*, Birmingham, November 2019, doi: 10.1049/cp.2019.0700.

4. [96] J. Singh, K. S. Alam, R. Stephan and M. A. Hein, "Metal Chassis Tolerant Conformal High Impedance Surface Based LTE-2600 Automotive Antenna", *2018 IEEE MTT-S International Conference on Microwaves for Intelligent Mobility (ICMIM)*, Munich, 2018, pp. 1-4, doi: 10.1109/ICMIM.2018.8443545.

5. [41] J. Singh, A. Asgharzadeh, R. Stephan and M. A. Hein, "Influence of Car Body Modeling on the Gain Patterns of Automotive Antennas", *2017 IEEE 85th Vehicular Technology Conference (VTC Spring)*, Sydney, NSW, 2017, pp. 1-5, doi: 10.1109/VTCSpring.2017.8108214.

6. [120] J. Singh, B. Altinel, C. Bornkessel, R. Stephan and M. A. Hein, "V2V communication performance of conformal plastic-embedded side-mount antennas investigated with field-operational tests," *2021 IEEE 93rd Vehicular Technology Conference (VTC2021-Spring)*, 2021, pp. 1-5, doi: 10.1109/VTC2021-Spring51267.2021.9448811.

7. [34] M. E. Asghar, F. Wollenschläger, A. Asgharzadeh, J. Singh and M. A. Hein, "Influence of antenna mounting location on the radiation pattern of an automotive antenna", *12th European Conference on Antennas and Propagation (EuCAP 2018)*, London, 2018, pp. 1-5, doi: 10.1049/cp.2018.1000.

8. [32] U. Tayyab, A. Kumar, Y. Li, R. Stephan, M. A. Hein and J. Singh, "Plastic-embedded Patch Antenna Array for Automotive Satellite Communication in the Ka-band", *2021 1st International Conference on Microwave, Antennas & Circuits (ICMAC)*, 2021, pp. 1-4, doi: 10.1109/ICMAC54080.2021.9678254.

9. [129] A. Asgharzadeh, J. Singh, P. Hofmann, G. Reichert and M. A. Hein, "Design approach towards automotive FM broadcast antennas based on characteristic modes", *2017 IEEE-APS Topical Conference on Antennas and Propagation in Wireless Communications (APWC)*, Verona, 2017, pp. 57-60, doi: 10.1109/APWC.2017.8062240.

Chapter 2

Background

2.1 Mobile communications: 0G to 5G, ITS-G5 and C-V2X

As this thesis deals with the design of mobile communications antennas, a short overview of the history of mobile communications would be interesting and also further motivate the development of new antenna solutions for the future.

The so called 'generation zero' began with bulky radio telephones available after the second world war, however, there were no such concepts as roaming or handovers and the call was maintained only within the coverage of the transmitting station. The system being analog, its capacity was limited as well, as each call required its own frequency channel. The first generation also supported only analog voice, but taking advantage of the cellular concept, frequency reuse was possible, which enabled an increased system capacity compared to generation zero. Connectivity could be maintained moving across the cells, but roaming was mostly still not possible, as the 1G technology was distinct in different countries. For example, advanced mobile phone service (AMPS) in the US operated in the 850 MHz band, employing full duplex channels with 30 KHz channel bandwidth, whereas C-Netz in Germany was operational in the 450 MHz band with a 20 KHz channel bandwidth. [19]

Digital transmission for signalling as well as traffic was first utilized in the second generation (2G) [19]. This led to a considerable increase in the system capacity, because in addition to the use of cellular concept, each frequency channel within a cell could be divided between several users using time-division multiple access (TDMA) or code-division multiple access (CDMA) techniques [19]. Global system for mobile communications (GSM) is TDMA based [19], and was specified by the European Telecommunications Standards Institue (ETSI), with main operating frequencies around 900 MHz and 1800 MHz and data rates up to 384 kbit/s [121]. The author of [121] further writes, "The development of the third generation (3G) mobile network (Universal Mobile Telecommunication System, UMTS) was motivated by new kinds of data services (mostly mobile internet) as well as restrictions from its predecessor 2G wireless technology. At the end of 1990, the first UMTS standard was completed. Together with modifications introduced by High Speed Packet Access (HSPA) concerning modulation, coding and scheduling, data rates up to 14 Mbit/s could be achieved in the downlink and 5.76 Mbit/s in the uplink. With long term evolution (LTE), the 3rd generation partnership project (3GPP) released the fourth generation of cellular communication systems. The motivation for the new standard of mobile wireless networks is based on a simplified flat packet-oriented network architecture, high data rates up to 300 Mbit/s in the downlink with 4x4 MIMO, reduced latency, scalable use of bandwidths from 1.25 MHz to 20 MHz and the use of Orthogonal Frequency Division Multiple Access (OFDMA) for downlink. In Europe LTE operates at frequencies around 800 MHz, 1800 MHz and 2600 MHz. Additionally, LTE relies on advantages offered by utilization of Multiple-Input-Multiple-Output

(MIMO) systems and thus exploits diversity in space, polarization or radiation pattern of multiple antennas at the same time". Further information on these topics may be found in [19-24]. Under rich multipath conditions, an $m \times n$ MIMO antenna configuration, with m , $n > 1$, can provide a $min(m, n)$-folds increase in data rate over a Single-Input-Single-Output (SISO) antenna configuration. The MIMO capabilities of LTE are discussed in more detail in chapter 6.

We have now entered the 5G era, wherein, as an example, using 100 MHz channel bandwidth in conjunction with 4 x 4 MIMO would enable data rates of up to 2 Gbps at 3.5 GHz. Furthermore, the use of mmWave frequencies in the 24.25...29.5 GHz range would allow for hot spots with data rates up to 20 Gbps. The frequencies below 3 GHz will not be be discarded though; they may not offer as high data rates, but are essential in terms of ensuring network connectivity over larger distances than possible with the higher frequency bands. [122]

While enabling mobile communications for passengers inside a car provides access to typical services that we already use in our day to day lives, car-to-everything communications open another realm of wide-ranging applications encompassing traffic safety, route optimization and navigation, and analysis of environmental data gathered by cars [25-27]. In this regard, there are two main approaches for V2X communication, both centred at around 5.9 GHz: The first is the ETSI ITS-G5 defined in 2004 which is an extension of the general WiFi standard modified and optimized for operation in a dynamic automotive environment [123, 124]. The second is the cellular-V2X or C-V2X, which is a recent extension of 4G-LTE that allows for the cars to communicate with mobile base stations as well [123, 124]. With the incorporation of base stations, C-V2X would be particularly useful for relaying information over larger distances than possible with ITS-G5. More information about these protocols and technologies may be found in the respective documentation [28-31, 125]. In order to counter the problems of dead spots in terrestrial networks, these technologies would also be supplemented with mmWave low earth orbit (LEO) satellite communication in the Ka-band [32, 33].

We see that over the course of these developments, a number of new frequency bands has been introduced, in addition to the earlier allocated frequency bands, and there is an ever increasing utilization of MIMO for enhanced data rates. The communications capabilities of modern cars have to keep up with all these developments, which makes the recognition of additional antenna mounting locations on cars, as well as the design of antennas suited for these locations an interesting and relevant area of research.

2.2 B-column plastic cover as antenna embedding location

In the last chapter, we noticed that a wealth of antennas has to be incorporated in a variety of locations distributed around the car. The radiation pattern and the efficiency of an automotive antenna are influenced by the electromagnetic interaction between the chassis and the antenna, and the extent of this influence varies depending upon the location of the antenna on the car, as well as the orientation of the antenna at that location. For example, [34] shows that shifting a vertically oriented wideband monopole antenna to different positions on a sedan rooftop results in non-negligible, frequency-dependent differences in the shape of its radiation pattern, as the operation frequency increases from 700 MHz to 5870 MHz. This study already effectively shows that an automotive antenna cannot be designed standalone and expected to perform just the same following installation on a car. For an accurate antenna design, the

antenna and at least a partial model of the car need to be simulated together, to take into account the electromagnetic interaction between them.

For antennas like half-wavelength electrical dipoles, an orientation directly above and parallel to the car metal chassis is particularly damaging, if the antenna is not at least $\lambda_0/6$ apart from the metal surface. At this distance from the ground plane, a half-wavelength dipole antenna has a theoretical input resistance of 50 Ω (refer Table 10-1 in [127]). As one starts to go below this distance, the destructive interference between the currents on the actual monopole and the image currents becomes increasingly stronger, which significantly deteriorates the input impedance of the dipole, leading to a poor reflection coefficient. Orienting a quarter-wavelength monopole antenna parallel to the car chassis in an 'inverted-L' form would also lead to the same problem of a low input impedance [35]. A low-radiation resistance would also imply a high quality factor, and therefore a narrow impedance bandwidth. These aspects, among other things, are discussed extensively in chapter 3, section 3.2.

The discussion above, coupled with the schematic in Fig. 2.1, lays bare the challenges associated with designing an antenna for embedding in the B-column plastic cover. We can see that an antenna embedded in the plastic cover of an Audi A1 will be barely 2...3 mm apart from the chassis metal after the plastic cover is mounted onto the car. For the 1.71...2.69 GHz LTE design frequencies considered in this work, a $\lambda_0/6$ distance from the car chassis lies between 29...19 mm. This rules out using typical planar half-wavelength dipole antennas. Patch antennas could be used at such a location, but such a solution would be lacking both in novelty and achieved impedance bandwidth. Clearly expressed, there are three main challenges:

- The first and the primary challenge with the considered embedding location is the design of new types of antennas that are tolerant against the proximity to the underlying chassis metal and can offer more bandwidth than typical low-profile patch antennas.

- The second is the reflection of radiation from the car chassis located immediately behind the antenna, which leads to the creation of a pattern null along the driving direction, as will be seen in the next chapters. The coverage of a plastic cover mounted antenna is therefore not omnidirectional like that of a rooftop monopole antenna. But as will be seen in chapter 6, this did not have any major impact on the LTE MIMO data rate performance when compared to rooftop monopole antennas.

- The third challenge arises due to the large difference in the electrical size of the antenna at these frequencies and the size of the car. The length of the Audi A1, for example, varies from $23 \cdot \lambda_{1.71\ GHz}$...$36 \cdot \lambda_{2.69\ GHz}$. This has consequences in the form of extended simulation times and demanding computation power requirements.

But, as mentioned before, such a simulation is necessary to correctly characterize and optimize the automotive antenna performance. Mainly the antenna dimensions need to be optimized/antenna needs to be tuned to nullify the shift in the resonance frequency due to plastic embedding and the electromagnetic coupling between the chassis and the antenna. From the conducted simulations, it could be ascertained that an antenna embedded in the plastic cover had a $\approx$5...7% backwards shift in the resonance frequency. There is a reduction in the antenna efficiency as well due to the additional dielectric/conductive losses contributed by the plastic cover/car chassis. These details are presented and discussed in the upcoming chapters.

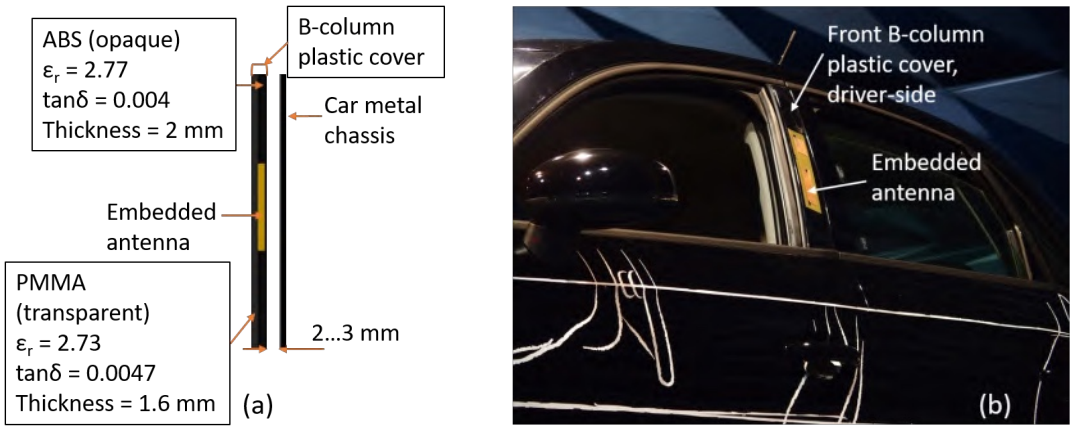

FIGURE 2.1: (a) Antenna mounting situation in the B-column plastic cover. (b) B-column plastic cover with an antenna embedded in the transparent PMMA layer mounted on the driver side front door.

One may argue on the basis of the listed challenges, that designing a functional antenna for the B-column plastic cover is more challenging compared to designing antennas for mobile phones, if not in all, but in many instances. Although mobile phones offer limited integration space as well, many of these have a plastic back with the obvious glass front screen. In these cases, challenge 1 simply does not appear and challenge 2 is also resolved as without any metal plane blocking the antenna, an omnidirectional pattern is easier to achieve. At the same time, as a mobile phone is minuscule compared to a car, simulations at the same set of frequencies are far less resource intensive and far quicker compared to car simulations, so challenge 3 is also drastically reduced.

The next section presents the simulation methodology followed in this work for an accurate antenna design considering the mentioned simulation challenges, and this approach is novel and original in itself.

2.3 Simulation and measurement considerations

2.3.1 Simulation tools and electromagnetic solvers

CST microwave studio [36] was used for all simulations in this thesis, unless otherwise stated. There are other electromagnetic simulation tools like Ansys HFSS or FEKO also available in the market [37, 38]. Regardless of these choices, all such software includes three main types of full-wave solvers for electromagnetic problems, namely, the time-domain solver based upon the finite difference time domain (FDTD) method or finite integration technique (FIT), the frequency-domain solver based upon the finite element method (FEM), and the integral equation solver based upon the method of moments (MoM). Depending upon the electrical size, the simulation model complexity, and the frequency bandwidth of the electromagnetic problem under consideration, one of these solvers, or a combination of these for a hybrid simulation approach may be used. Some general guidelines for which solver to use when are provided in [39] and [40].

As the antennas presented in this thesis were resonant in nature, the frequency domain solver was the appropriate choice at least for the simulations of the bare antenna and where the simulation model dimensions did not exceed $10 \cdot \lambda_0$. For simulations models that are electrically even larger in comparison to the size of the

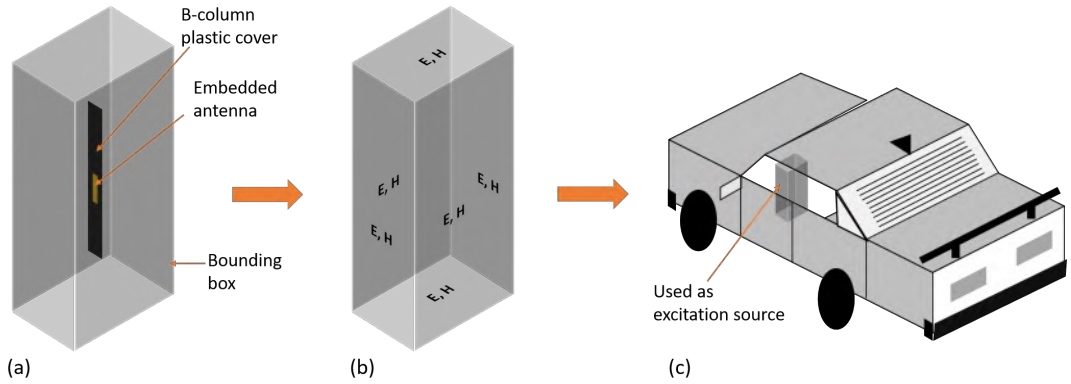

FIGURE 2.2: Hybrid simulation procedure. (a) The plastic cover and the embedded antenna are simulated using FEM. (b) The complex electric and magnetic fields recorded on the walls of the bounding box are exported as an excitation source. (c) The excitation source is placed at the relevant location on the car body for an MLFMM based simulation.

installed antenna, surface mesh based multilevel fast multipole method (MLFMM), an extension of the MoM, is recommended in conjunction with either the time domain or frequency domain solver for a hybrid simulation. The small antenna along with a portion of the large structure can, for example, be simulated with the frequency domain solver, and complex electric and magnetic fields captured on the bounding box of this sub-problem are then used as an excitation source in an MLFMM simulation of the complete model. This procedure is illustrated in the form of a schematic in Fig. 2.2.

2.3.2 Influence of simulated model complexity

The more detailed the simulation model, the more accurate would be the simulation results. However, highly complex computer aided design (CAD) models pose the previously mentioned challenges of increased computational resource requirement and simulation time. There could be instances where, depending upon the electrical size of the problem at hand, the computational resources would be just enough to simulate a complex CAD model, but that would imply that other users on the same server would not have the possibility to run their own simulations. Therefore, we need to come to some sort of a compromise in terms of the complexity of the CAD model used for simulations. Naturally, this entails a reduction in the accuracy of the simulation results, but it must be noted that we do not just rely on simulation results for characterizing the antenna performance, but necessarily perform measurements in an anechoic chamber as well, and these two in conjunction provide the complete picture.

Examples pertaining to the influence of car model complexity on the radiation characteristics of an automotive antenna can be found in [41, 42], among other such sources. In [41], the author's own publication for instance, the influence of car model complexity reduction on the radiation pattern of a rear windscreen embedded FM antenna was considered. The choice of an FM antenna for this analysis was motivated by the fact that the dimensions of a typical passenger car are comparable to the FM wavelength ($\approx$ 3 m), and in that the simulation of a relatively detailed CAD model of a car as a reference for comparisons would not be so resource intensive.

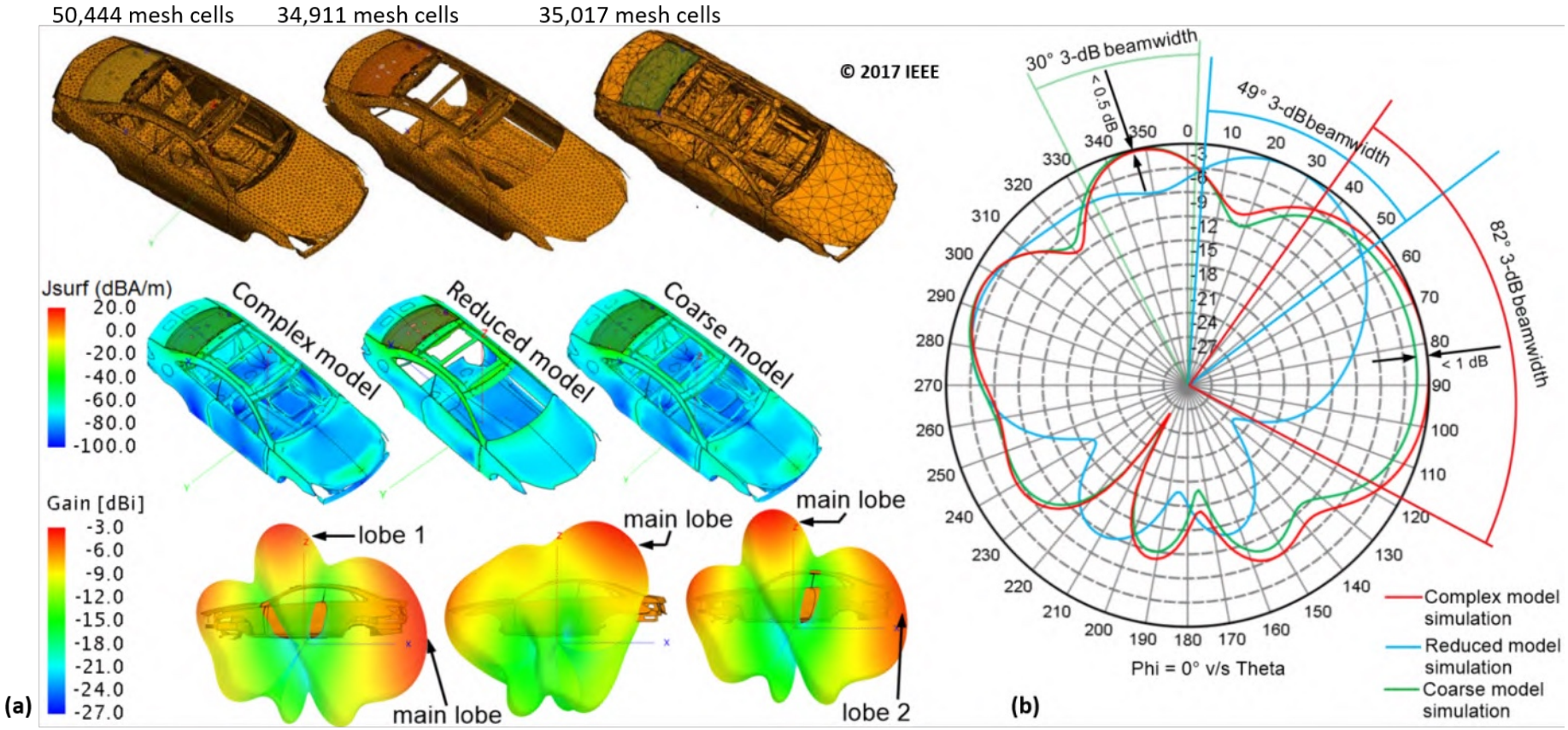

FIGURE 2.3: (a) Car models of differing complexities and the corresponding surface current distributions and realized gains at 98 MHz for an FM antenna embedded in the rear windscreen of the car. (b) Comparison of the normalized radation pattern cuts along the length of the car for the three simulated models. [41] ©2017 IEEE

The simulations were carried with the MoM solver of FEKO, and the results are summarized in Fig. 2.3. Considered first in Fig. 2.3 (a) is the simulation of the complex model mesh provided by an automotive manufacturer, then the simulation with some low current density parts removed form the car cabin while maintaining the same mesh fineness on the remaining portions of the car, followed by a simulation wherein nothing was removed from the car, but the mesh was coarsened everywhere except for the windscreen embedded antenna. It must be mentioned here that the mesh cannot simply be coarsened arbitrarily; the longest edge of any mesh cell must be $\leq \lambda_0/10$ in length, where λ_0 is the wavelength at the considered simulation frequency. The fields computed for each such tiny mesh cell are added together respecting the electromagnetic boundary conditions at the edges between the mesh cells to provide the complete field distribution on the simulation model. Fig. 2.3 (b) is a comparison of the normalized vertical cuts of the three radiation patterns, taken along the length of the car.

We can see that removing the low current density parts from the complex model led to a different current distribution in the reduced model. As a result, the obtained antenna radiation pattern was also unlike the original radiation pattern. This is clear because the far field is the Fourier transform of the near field distribution; changes in the near field are correspondingly transformed into changes in the far field. However, we took note of the fact that the complex mesh was overall much finer with respect to the $\lambda_0/10$ mesh cell side length limit stated above. This provided some leeway to coarsen the mesh on the car body. The windscreen embedded antenna being the primary radiator, its mesh was not coarsened, as that would have certainly contributed to differences in the far field results. It can be observed that the coarse model and complex model results are very similar.

Let us consider the computation time and memory requirements listed in Table 2.1 for each of these simulations, that were performed on a workstation comprising two Intel Xeon X5680 3.33 GHz hexacore processors and 96 GB RAM. Parallel computation capabilities of FEKO were used for all of these simulations. There were 6 parallel processes, with one process running on each of the six cores of one of the Intel Xeon X5680 processors of the workstation. We see that as the number of mesh cells in the reduced model and the coarse model was nearly the same, the computation time and the memory required for these simulations was also similar, and considerably less than that required for simulating the complex model. Therefore, considering that the simulation time and resource requirement are entirely dependent on the number of unknowns or mesh cells in a simulation, it is a better strategy to keep the number of mesh cells low by not over-finely meshing the all parts of the simulation model, rather than by removing parts with a lower surface current density.

These were simulation examples, where the operational wavelength and the dimensions of the car were comparable. Now if the operational wavelength were to be 10...30 times longer, as in the case of mobile communication frequencies,

TABLE 2.1: Computational time and memory requirements for the simulated models [41] ©2017 IEEE

Model type	Number of mesh cells	Simulation duration (hours)	Memory used (GB)
Complex model	50,444	11.72	65.4
Reduced model	34,911	3.97	26.7
Coarse model	35,017	3.92	28.1

we would quite quickly reach the limits of the available computational resources even with the coarse car model, unless hybrid simulation methods compris-ing a FEM - MLFMM or FDTD - MLFMM combination are employed. While hybrid simulation methods are certainly faster and less resource intensive, one drawback with them is that they do not consider material losses in the computation. We are only provided with the current distribution on the considered model and the directivity pattern of the antenna at the conclusion of the simulation. Considering this aspect, and the fact that a complete model of of a car comprising every possible detail would anyway not be simulated, implies that the results obtained through such a simulation procedure would be more qualitative in nature, but in any case useful enough to gain some insight into the interaction between the antenna and the car as will be seen in the upcoming chapters.

2.3.3 Simulation and measurement methodology followed in this work

It can be noted from the previous discussion that computational resource and time restrictions would not permit the design of B-column plastic cover embedded mobile communications antennas with the whole car in the simulation domain. Therefore, a three step approach, as depicted in Fig. 2.4, was adopted for the design and evaluation of the antenna performance. The first step comprised the simulation of the bare antenna, the second involved the simulation of a simplified door frame structure with the embedded antenna, and the third was the simulation of the car chassis using a FEM - MLFMM hybrid simulation methodology. The plastic cover with the embedded antenna was solved separately with FEM, and the near field captured on the bounding box of this problem was used as an excitation source for the car chassis in an MLFMM simulation. The first two steps allow one to observe the variation in the antenna reflection coefficient going from the bare configuration to the embedded configuration, while the three steps as a whole enable us to see how, at the same frequency, the radiation pattern changes from the first to the last configuration. As each simulation also produced electric field/surface current distributions, commenting upon origin of the radiation pattern differences was also possible based upon the consideration of these distributions.

In correspondence, three types of measurements were performed in anechoic chambers - a smaller chamber for the bare antenna and the door frame, whereas a larger one for measurements with the car. The characteristics of the these chambers are described ahead.

2.3.4 Measurements in the antenna measurement lab (AML)

AML is a fully anechoic chamber that allows for the full (except for the small region where the positioner shadows the antenna) three-dimensional spherical near-field/ far field measurement of the antenna-under-test (AUT)/device under test (DUT), and is based upon the roll over azimuth principle [43]. This principle and a snapshot from the AML are depicted in Fig. 2.5. The AUT is mounted on a rotator capable of rotation between -180°... + 180° in the azimuth plane. A vertical arm affixes the AUT rotator to another rotator at the bottom that enables rotation over a 360° range in the elevation plane. This allows for the gathering of data around an imaginary spherical surface that surrounds the AUT. This anechoic chamber was used for the measurements of the bare antennas and the partial door frame mounted antennas for this thesis. The key characteristics of the AML are listed in the first column of Table 2.2, and further details are available in [44].

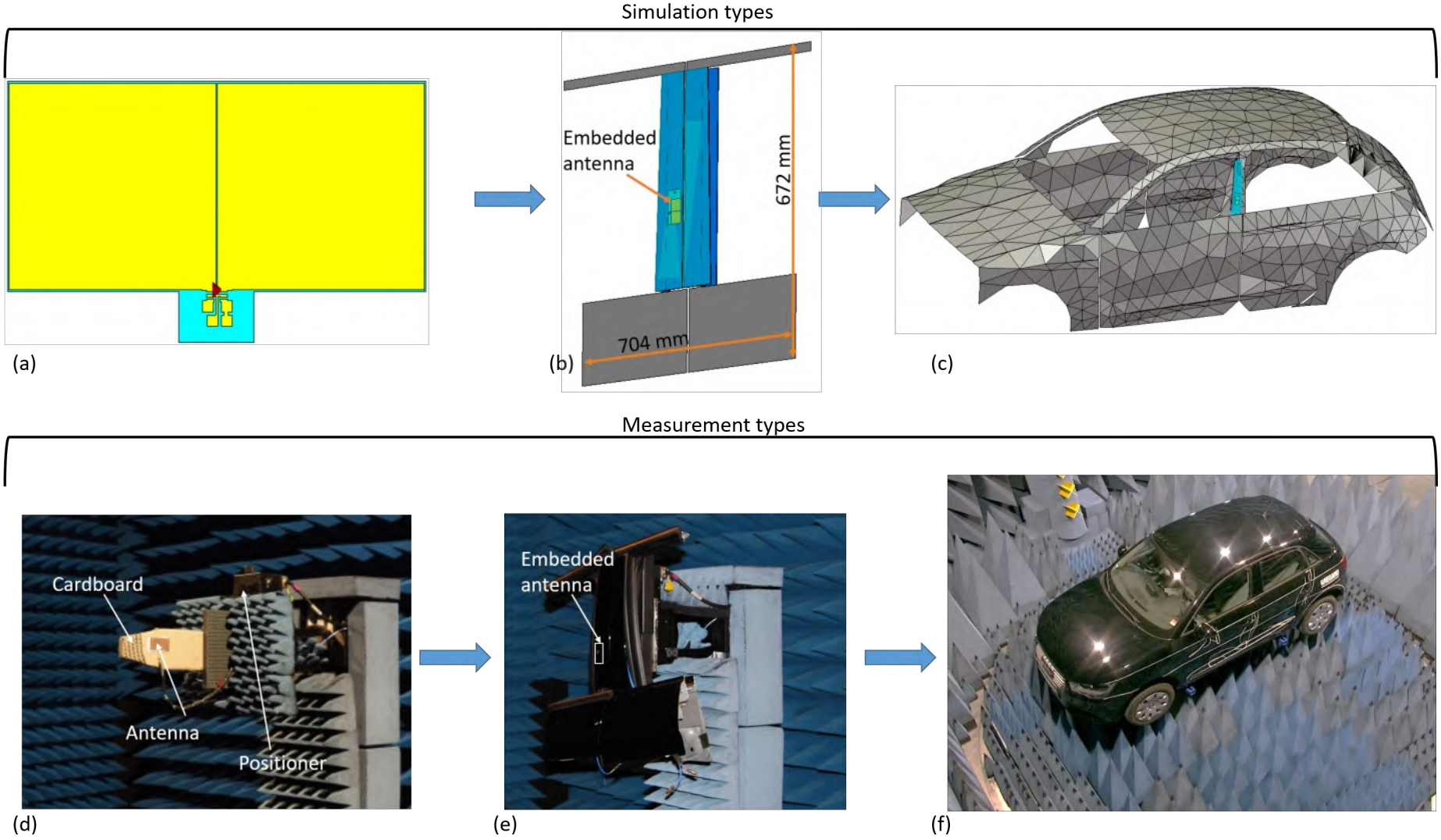

FIGURE 2.4: (a) Bare antenna simulation model. (b) The antenna embedded in a simplified simulation model of the partial door frame. (c) A simplified simulation model of the car chassis including the plastic embedded antenna. (d), (e), (f) Anechoic chamber measurements corresponding to the conducted simulations.

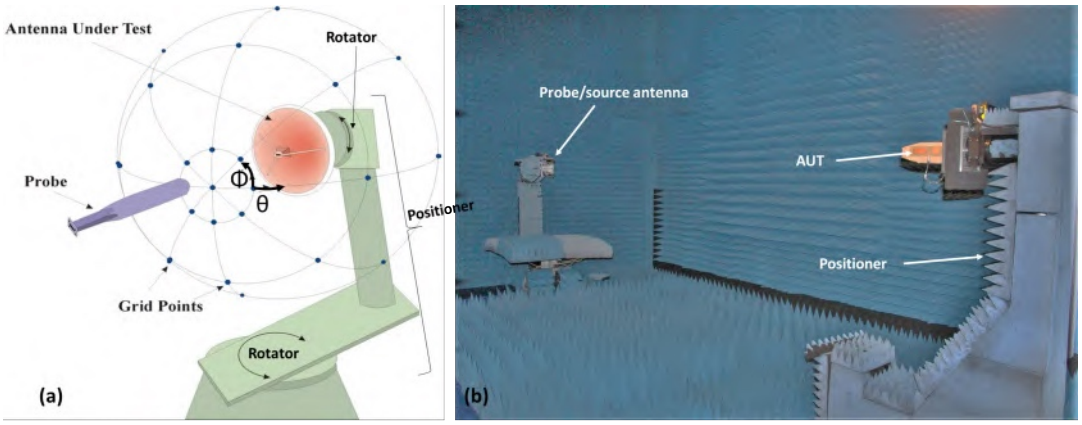

FIGURE 2.5: (a) The roll over azimuth configuration [43]. (b) A snapshot from the AML, showing the positioner with the mounted AUT, as well as the source antenna.

TABLE 2.2: Some of the key characteristics of the AML and VISTA

Measurement facility	AML	VISTA
Frequency range (GHz)	0.8...110	0.07...6
Measurement type	Spherical near/far field	Spherical near/far field
		OTA performance tests
		EMC
Gain measurement uncertainty	±1 dB	0.07...0.22 GHz: ±4.6 dB
		0.22...0.4 GHz: ±3.3 dB
		0.4...0.7 GHz: ±1.9 dB
		0.7...6 GHz: ±1.4 dB
Dimensions (L x W x H) (m^3)	9.2 x 5.2 x 5.2	16 x 12 x 9
Turntable diameter (m)	—-	6.5
Maximum DUT weight (kg)	≤ 10	≤ 2500

2.3.5 Measurements in the virtual road simulation and test area (VISTA)

A snapshot from VISTA is presented in Fig. 2.6, and it differs from the AML in several key points. It is not only used for the spherical near-field measurements of AUTs/DUTs, which are usually passenger cars with installed antennas, but also for over-the-air (OTA) performance tests [45], as well as for electromagnetic compatibility and interference (EMC) compliance tests [46]. Depending upon the type of measurement under consideration, VISTA may be used as a fully anechoic chamber or as a semi anechoic chamber by the partial or complete removal of the pyramidal absorbers from the floor. For radiation pattern measurements, the car with the installed antenna(s) is placed on the turntable, which is then raised such that the installed antennas are roughly at the geometrical centre of the probe arch. The arch is split into two halves: the left half comprises 111 probes with an angular spacing $\Delta\theta = 1^\circ$ that cover the upper frequency range 0.4...6 GHz, while the right half comprises 22 probes with an angular resolution $\Delta\theta = 5^\circ$ that cover the lower frequency range 0.07...0.4 GHz. We can also notice that the arch is truncated below $\theta = 110^\circ$ on either side. As the transformation from the near-field to the far field requires near-field data over the entire sphere, the missing near-field data in the truncated region may be extrapolated using techniques such as iterative modal filtering, among others [47],

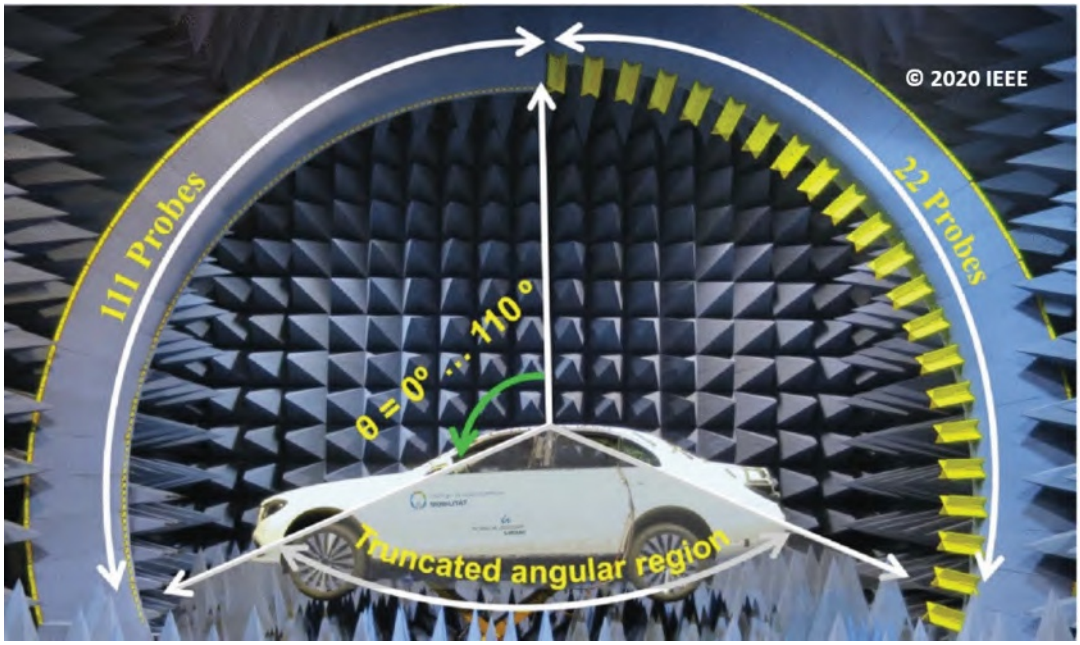

FIGURE 2.6: A snapshot from VISTA, with a passenger car on the raised turntable [47] ©2020 IEEE. The probes on either side of the arch cover the elevation range $\theta = 0°...110°$; beyond that the arch is truncated. The 111 probes on the left cover the frequency range 0.4...6 GHz, whereas the 22 probes on the right cover the frequency range 0.07...0.4 GHz.

which is better than simply padding zeros in place of the missing data. However, many of these advanced extrapolation algorithms were introduced at a stage when nearly all the measurements presented in this work were already completed and evaluated. As a result, the radiation patterns presented in this work are strongly truncated in the truncation region. For antennas that radiate predominantly into the upper hemisphere, this is of minor consequence. But B-column antennas are located on the sides of the car, and have a portion of radiation in the lower hemisphere as well. Truncation of this portion implies that the antenna efficiency associated with this portion is not accounted for as well, and would therefore appear to be lower than it actually is. This has been discussed in sufficient detail in [47], and provides some explanation for the differences in the antenna efficiency obtained with the partial door frame measurements in the AML and the car measurements in VISTA presented in the chapters ahead. For this thesis, VISTA was used in both the configuration; fully-anechoic for radiation patterns measurements, and semi-anechoic for LTE-MIMO performance evaluation of the antennas installed on the car. These and some of the other key characteristics of VISTA are listed in the second column of Table 2.2, with further details available in [44, 106].

Chapter 3

Di-patch antenna

3.1 Novelty and design description

When we think of a simple, planar, conformal, metal surface tolerant and robust antenna, a patch antenna is an almost immediate thought. Since its introduction in 1953 [48], these characteristics have enabled patch antennas to amass a wide application base including, but not limited to, satellite communication, missile telemetry, mobile communications, and automotive GPS and radar. But, just as with everything, a patch antenna is not without its shortcomings. The principle among them is its low impedance bandwidth of roughly 2% for a typical substrate thickness of $\approx \lambda_0/20$, λ_0 being the free-space wavelength at the resonance frequency [49, 63].

In comparison, we have the half-wavelength dipole antenna, one of the oldest antennas, first used by Hertz in 1886 to demonstrate the existence of radio waves [50]. A typical half-wavelength dipole has around 10% fractional bandwidth [51], radiates omnidirectionally in one plane, and offers a 2.15 dBi peak directivity, which is approximately 5...6 dB lower than directivity of a typical patch antenna. This is understandable, as a patch is fundamentally a broadside array of two equivalent magnetic dipoles radiating in half-space [52]. The directivity of a half-wavelength dipole can be more than doubled by arranging it horizontally above a metallic reflector (Fig. 3.3 and the associated text) , but as the distance between the reflector and the dipole becomes $\ll \lambda_0$, the driving-point impedance of the dipole becomes negligible, and the dipole turns into an inefficient r adiator. The driving-point impedance is defined as the input impedance of the antenna in the presence of the other elements or obstacles, in this case the metallic ground. This is in contrast to the self-impedance of the antenna, which is its input impedance in free-space.

So, on the one hand, is a patch antenna inherently metal-surface tolerant but with a poor bandwidth, and on the other hand, we have a half-wavelength dipole antenna which has a much larger impedance bandwidth but poor metal surface tolerance. What would be desirable is an antenna that is metal surface tolerant, but has a larger bandwidth than a typical patch antenna. There are multi-band enhancements to the patch antenna, and there are high impedance surface solutions to the poor metal surface tolerance of a half-wavelength dipole, as discussed in chapters 4 and 5 respectively. But these are more involved and complex in their design.

The di-patch antenna, first presented in the author's publications [53, 54, 55], and sketched in Fig. 3.1, provides an extremely simple to design, and novel antenna solution that is metal surface tolerant like a patch antenna, but offers other advantages as well. Not only does it have twice the impedance bandwidth and at least 40% smaller total surface area, there is also no compromise of directivity/gain compared to a patch antenna at the same frequency for the same substrate permittivity and thickness. The antenna comprises two half-wavelength square metallic patches

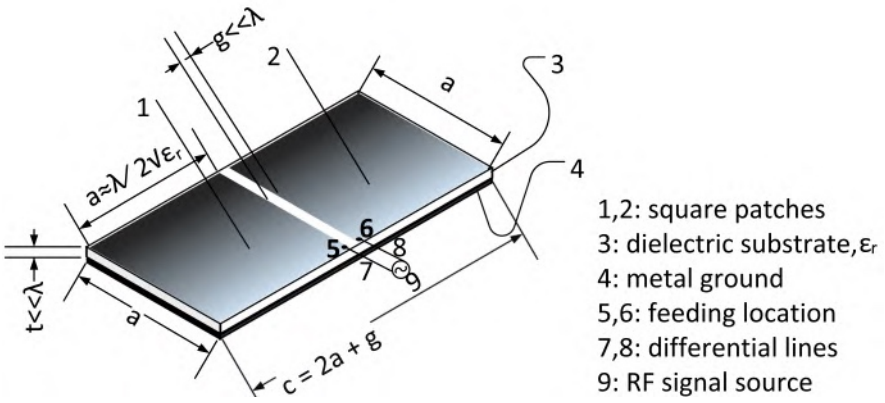

FIGURE 3.1: Schematic of a di-patch antenna; details provided in the legend and the main text [54] ©2019 IEEE.

separated by an electrically small gap of width 'g'. The total length of the antenna is therefore one wavelength (plus 'g'). The two patches are fed differentially at the points 5 and 6, and form the upper side of a grounded dielectric substrate of thickness 't'. Differential feeding provides the added benefit of common-mode noise rejection. The ground is a floating ground - there is neither a shorting post nor any other sort of electrical connection between the patches and the ground.

Discovery of the di-patch antenna: In literature, both old and contemporary, the dipole antenna that is most discussed and presented is the half-wavelength electrical dipole antenna, as such a dipole antenna can provide a 50 Ω input impedance in free-space. The full-wavelength dipole antenna plays second fiddle in comparison, because its input impedance in free-space is thousands of ohms [56, 57], leading to impedance matching challenges. For this thesis though, the input impedance behavior of an antenna closely above a ground plane was of primary concern, and not its input impedance in free space. In that regard, as already mentioned, the half-wavelength dipole is practically short-circuited at close proximity to a metal sheet. A similar behavior is predicted in literature, cited in the later sections, for a full-wavelength dipole antenna above a ground plane. But curiously it was observed in the author's simulations that the input impedance of a full-wavelength dipole did not drop to zero closely above a ground plane, but rather increased much beyond its value in free-space. This was an exciting observation, because now one could ask the question if it would be possible to bring down the input impedance of the full-wavelength dipole above the ground plane to 50 Ω through modifications in its design/shape. It was seen that by modifying the thin cylindrical dipole antenna into the form as depicted in Fig. 3.1 this target could be achieved. This was a first of its kind result, and exactly applicable for B-column integration, considering the proximity of the B-column plastic cover to the car chassis. Although differentially-fed planar antenna configurations do exist in literature [58-62], either the distance between the antenna arms/patches is a half-wavelength, one or both the patches are shorted to the ground, one or more parasitic elements are employed, and/or the design of the feed lines is complex.

The remainder of the chapter proceeds as follows:

- First, some interesting insights from the electromagnetic behaviour of a dipole antenna in its fundamental mode above a metallic ground are presented. An understanding of how a dipole antenna in its fundamental mode can act as an equivalent source model for describing the electrical behaviour of a typical

patch antenna is developed and described. The radiation patterns of the patch antenna and the half-wavelength dipole closely above a ground plane were identical. In terms of impedance matching closely above a ground plane, the half-wavelength dipole antenna was of course practically short-circuited, as opposed to a patch antenna that can easily achieve a 50 Ω impedance above a ground plane. In this respect, it was shown (elaborating upon and taking hints from [74]) that a half-wavelength folded dipole antenna with an appropriate number of arms not only achieves a 50 Ω input impedance above a ground plane, but also has a radiation pattern identical to that of a patch at the same frequency and at the same height above a ground plane. These approaches differ from the traditional resonant cavity model approach followed for patch antennas in standard books like [52], and offer a fresh perspective on patch antenna modeling.

- Taking the learning points from patch antenna modeling, it is shown that how starting with a thin dipole antenna in its second harmonic mode one can arrive at the di-patch antenna configuration of Fig. 3.1. It is interesting to note the contrast to the previous point here. In the former point, it was desired to raise the input impedance of a half-wavelength dipole above a ground plane to 50 Ω from nearly 0 Ω, which could be achieved by folding the dipole. For this point, the input impedance of a full-wavelength dipole antenna needed to be reduced to 50 Ω from the initial several thousands ohms above the ground plane. These di-patch antenna modeling considerations are followed by a sensitivity analysis of the di-patch antenna to parameter changes. Thereafter, the performance of a di-patch antenna is compared with a patch antenna, and the simulation and measurement results of a plastic cover embedded di-patch antenna with the partial door frame and the whole car are presented. The last section presents a 1×2 series-fed di-patch array made using principles known from similar patch arrays, and provides a succinct simulation based comparison between the two array types.

3.2 Di-patch antenna equivalent model

3.2.1 Half-wavelength dipole above metal ground and patch equivalence

Consider a half-wavelength dipole at a distance h above an infinite metallic ground as in Fig. 3.2 (a). This system satisfies the boundary condition $\hat{z}\times\ \mathbf{E} = 0$ at z = 0, i.e., on the plane AA′. We are interested in the **E** and **H** fields above AA′. We can use image theory to convert this complex half-space problem into a simple to solve free-space problem. As long as the free-space problem contains the original dipole source, and the tangential components of the electric field vanish at the interface AA′, the free-space problem will be equivalent to the original half-space problem. The equivalent problem is shown in Fig. 3.2 (b). We remove the ground plane and introduce a virtual dipole source dipole at a distance h from the interface AA′. The virtual dipole has the same magnitude but opposite phase as the actual dipole. It is now quite simple to show that the tangential field components disappear along AA′ [64-66], but what is more interesting are the advantages from this simpler equivalent system. One can see that the equivalent problem is similar to an end-fire array of two dipoles with a separation '2h' between them, and this has two consequences:

1. The electric field at any far-field point 'P' above the interface AA′ is the vector sum of the contributions from the actual dipole and the virtual dipole.

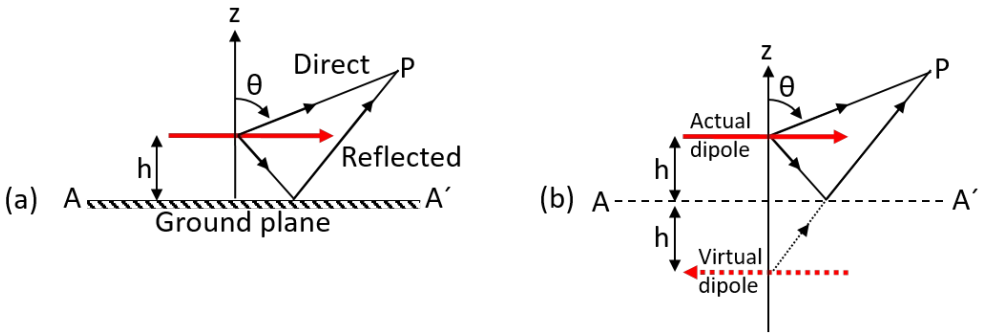

FIGURE 3.2: (a) Original problem: Half-wavelength dipole at a height h above an infinite metallic ground. (b) Equivalent problem: Infinite ground replaced by an oppositely oriented virtual dipole at a distance $2h$ from the actual dipole.

2. The influence of the ground on the self-impedance of the dipole can be quantified in terms of the mutual electrical interaction between the actual dipole and the virtual dipole, as explained later.

As the interest lies in demonstrating the equivalence between a half-wavelength dipole above a ground and a typical patch antenna, it is necessary to compare their directivities, radiation patterns, surface current/electric field distributions, and resonance conditions. First consider point 1. Assuming that the dipoles in Fig. 3.2 (b) are infinitesimal, [64] shows that the peak directivity, D_0, dependent upon h is given by the equations 3.1 and 3.2:

$$D_0 = \begin{cases} \dfrac{4 \cdot sin^2(\beta h)}{\frac{2}{3} - \frac{sin(2\beta h)}{2\beta h} - \frac{cos(2\beta h)}{(2\beta h)^2} + \frac{sin(2\beta h)}{(2\beta h)^3}} & h \leq \lambda_0/4 \quad (3.1) \\ \dfrac{4}{\frac{2}{3} - \frac{sin(2\beta h)}{2\beta h} - \frac{cos(2\beta h)}{(2\beta h)^2} + \frac{sin(2\beta h)}{(2\beta h)^3}} & h > \lambda_0/4 \quad (3.2) \end{cases}$$

where β is the wavenumber.

It can be determined that as $h \to \infty$, D_0 of the Hertzian dipole approaches 7.78 dBi. Considering that the free-space directivity of a Hertzian dipole is 1.76 dBi, this is an increase of slightly more than 6 dB. It is then natural to conclude that the directivity of a half-wavelength long dipole antenna would slightly exceed this value as $h \to \infty$, as free space directivity of such a dipole is 2.15 dBi to begin with. In any case, the directivity values for $0 < h \leq 0.1\lambda_0$ are of prime importance for the purpose of comparison with a patch antenna, as typical patch antenna substrate height, h_{patch} corresponds to this range. D_0 for a Hertzian dipole varies from 8.5...8.75 dBi in this height range, and would be accordingly slightly higher for a half-wavelength dipole antenna above a ground plane, as may also be inferred from the orange shaded region in Fig. 3.3 [74]. These directivity values for a half-wavelength dipole antenna above ground in the orange region are very close to those predicted by the cavity resonator model [52] for a patch antenna, which is briefly outlined next.

As per [52, 93], a patch antenna can be modelled by a dielectric-loaded cavity with two perfectly conducting electric walls (patch at top, infinite ground at bottom with a separation h_{patch} between the two), and four perfectly conducting magnetic walls on the sides. The dielectric in this case is assumed to be vacuum. The four side walls represent four slots which may or may not contribute to radiation, depending upon

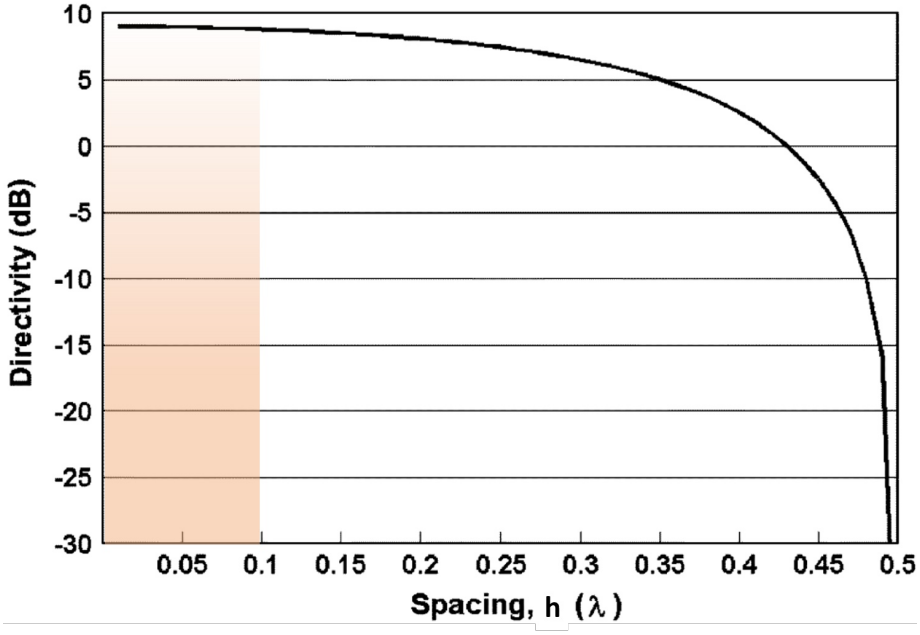

FIGURE 3.3: Simulated directivity in the broadside direction for half-wavelength electrical dipole antenna arranged horizontally above an infinite ground plane, as a function of the distance between the dipole and the ground plane (adapted from [74] ©2004 IEEE). The region of interest for comparison with a patch antenna has been shaded orange. (At 0.5 λ_0 spacing, the dipole and ground interfere destructively in the broadside, hence the large drop in directivity.)

the orientations and the magnitudes of the magnetic current densities on these slots. Applying image theory, this half-space problem can be converted into a free-space problem, in that the ground plane is removed while doubling the magnetic current densities on each of the four side walls of the patch antenna. The magnetic current densities along the slots indicated in Fig. 3.4 are equal in phase and magnitude, and form a broadside array that radiates into the upper half space.

Assuming that $h_{patch} << \lambda_0$, the peak directivity of a patch antenna can be expressed [52] as:

$$D_0 = \begin{cases} 6.6\ (linear) = 8.2\ dBi & W << \lambda_0 \quad (3.3) \\ 8\left(\frac{W}{\lambda_0}\right) & W >> \lambda_{0.} \quad (3.4) \end{cases}$$

Realistically, W is neither too small, so as to avoid a reduction in the radiation efficiency, nor is it larger than λ_0, so as to prevent the excitation of higher order modes. In other words, with vacuum as the substrate, a realistically dimensioned patch antenna, with $h_{patch} << \lambda_0$, will have a directivity slightly larger than 8.2 dBi. Referring back to Fig. 3.3, we see that the directivity of a thin dipole in the orange region is indeed comparable to the patch antenna directivity predicted through the cavity resonator model.

However, the preceding was only a comparison of the peak values of directivity. Next, the normalized radiation patterns and electric field distributions of a patch antenna and a dipole antenna are compared in Fig. 3.5. The peak directivity to which the patterns were normalized was chosen to be the maximum of the peak directivities obtained for the dipole and the patch in each case. The analysis/comparisons were

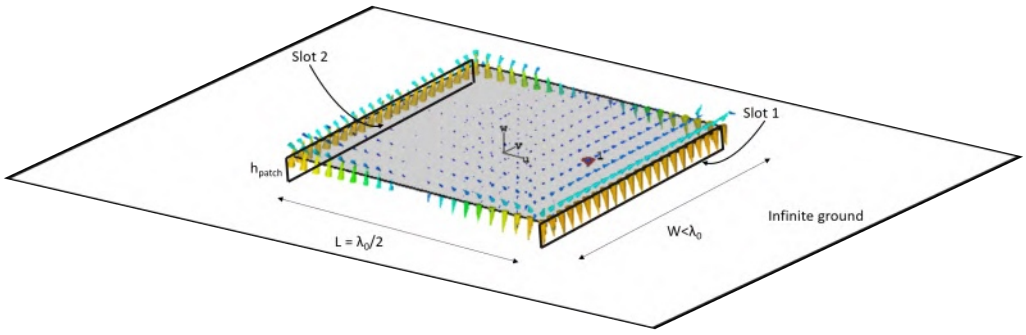

FIGURE 3.4: A patch antenna simulated above an infinite ground plane, depicting the TM_{010} fundamental mode **E**-field distribution. Slots 1 and 2 add in phase and lead to radiation in the far-field.

carried out at 2.6 GHz, corresponding to $\lambda_0 = 115$ mm. The height h of the dipole above the infinite ground plane and the substrate thickness h_{patch} of the patch antenna were kept the same at 1.6 mm, which at 2.6 GHz is approximately $0.015\lambda_0$.

Fig. 3.5 (a) compares a typical half-wavelength dipole antenna with a patch antenna in half space. An excellent agreement can be observed between the normalized radiation patterns, and the electric field distributions considered at the same phase. The agreement between the electric fields was similarly good at all other phases. However, the seemingly perfect patch-dipole equivalence demonstrated above suffered from the following limitations:

1. The equivalence between the radiation patterns and the electric field distributions holds only at antenna lengths that are odd multiples of the fundamental mode, i.e., at $(2n+1)(\lambda_0/2)$, where $n \in \mathbb{W}$. At $2p(\lambda_0/2)$ physical lengths, where $p \in \mathbb{N}$, the electric field distribution, and therefore the radiation pattern are starkly different compared to a patch antenna of comparable physical length. Two examples are provided in Fig. 3.5 (b) and (c), where 2.6 GHz is a higher-order mode resonance. The first example shows the disagreement between the patch antenna and the dipole antenna patterns and fields for $L = 2(\lambda_0/2)$. Although both the patch and the dipole have a voltage maximum at their centre in this mode, the presence of the feed-gap in case of the dipole causes the electric field to distribute differently from the patch, which does not have a feed-gap. The second example shows the reinstatement of the agreement between the results at $L = 3(\lambda_0/2)$. This trend continued like this, and furthermore it was noted that at $2p(\lambda_0/2)$ lengths, the patch antenna radiation pattern always had twice the number of lobes in the E-plane as compared to the corresponding dipole antenna radiation pattern at the same frequency.

2. If the dipole antenna port in Fig. 3.5 (b) was shifted a quarter-wavelength off-centre, where the voltage minimum lay, then the electric field distributions, and therefore the radiation patterns of the dipole antenna and the patch antenna at $L = 2(\lambda_0/2)$ were in perfect agreement. Through such a procedure, an agreement could be established between a patch antenna and a dipole antenna electric fields at any physical length $L = 2p(\lambda_0/2)$ at the corresponding $2p^{th}$ harmonic resonance. But the agreement was then lost at lengths that were odd multiples of half-wavelength.

3. A point can be found between the patch and ground where the patch offers a 50 Ω self-impedance. However, at the considered small distances to the ground,

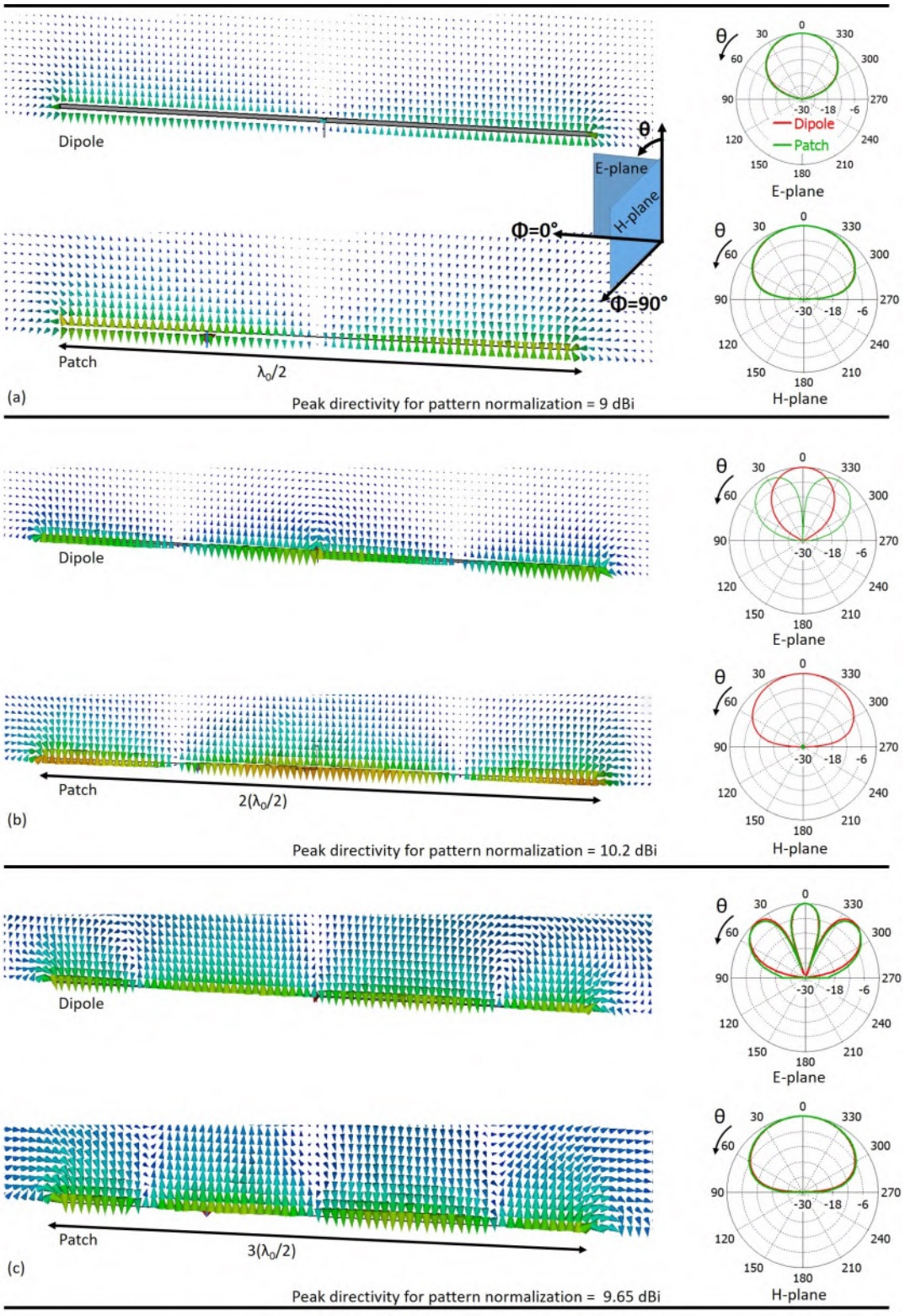

FIGURE 3.5: (a), (b), and (c) compare the electric field distributions in the E-plane and the normalized radiation patterns in the E- and H-planes for dipole antennas and patch antennas of lengths $\lambda_0/2$, $2(\lambda_0/2)$, and $3(\lambda_0/2)$. The comparison is at 2.6 GHz, which is the fundamental, second, and third harmonic resonance in (a), (b), and (c) respectively. The antennas lie in the $\theta = 90°$ plane, 1.6 mm above a perfect electric boundary, and are oriented along the $\phi = 0°$ axis.

a $(2n+1)\lambda_0/2$ length electrical dipole has a very low driving-point impedance, and is a poor radiator.

3.2.2 Half-wavelength folded dipole as patch antenna equivalent

Considering the preceding limitations, a more comprehensive dipole antenna equivalent for a patch antenna was desirable. The advanced model should take into account impedance matching, and reconcile the differences in the electric field distributions and radiation patterns at $2p(\lambda_0/2)$ antenna lengths. Let us first see how a half-wavelength dipole antenna can be modified to achieve a 50 Ω input impedance above a ground plane. To achieve this, referring back to Fig. 3.2 (b), the impact of the mutual impedance, Z_{21}, between the actual dipole and the image dipole, on the self-impedance, Z_{S1}, of the actual dipole needs to be first understood. Let the actual dipole be initially in free space, with a voltage V_1 across its terminals, and a current I_1 along its length. Now this dipole is brought close to a ground plane as in Fig. 3.2 (a). Then the equivalent scenario comprises a parallel image dipole, as in Fig. 3.2 (b), that carries an equal magnitude but opposite phase current I_2 along its length. Due to the interaction between these two dipoles, the voltage on the actual dipole becomes

$$V_1 = I_1 Z_{S1} + I_2 Z_{21} = I_1 (Z_{S1} - Z_{21}) \tag{3.5}$$

as $I_2 = -I_1$. Therefore, the driving point impedance, Z_{D1}, of the actual dipole may be given as

$$Z_{D1} = \frac{V_1}{I_1} = Z_{S1} - Z_{21}\ \Omega \tag{3.6}$$

Z_{D1}, Z_{S1} and Z_{21} may be calculated using the following formulas presented in [68, 127], for a dipole antenna of radius a.

$$\begin{aligned} R_{S1} =& 30\left[\left(1-\cot^2\beta L/2\right)\overline{\mathrm{Ci}}2\beta L + 4(\cot^2\beta L/2)\overline{\mathrm{Ci}}\beta L \right. \\ &\left. + 2(\cot\beta L/2)(\mathrm{Si}\,2\beta L - 2\,\mathrm{Si}\,\beta L)\right]\ \Omega \end{aligned} \tag{3.7}$$

and

$$\begin{aligned} X_{S1} =& 30\left[\left(1-\cot^2\beta L/2\right)\mathrm{Si}\,2\beta L + 4(\cot^2\beta L/2)\,\mathrm{Si}\,\beta L \right. \\ &\left. + 2\cot\beta L/2\{2\overline{\mathrm{Ci}}\beta L - \overline{\mathrm{Ci}}2\beta L - 2\log(L/2a)\}\right]\ \Omega \end{aligned} \tag{3.8}$$

Taking $H = 2h$ as the separation between the actual dipole and the image dipole in Fig. 3.2 (b), the real/imaginary components of Z_{21} may be defined as:

$$\begin{aligned} R_{21} = 30&\frac{1}{\sin^2(\beta L/2)}\left\{2(2+\cos\beta L)\mathrm{Ci}\beta H \right. \\ &- 4\cos^2\frac{\beta L}{2}\left[\mathrm{Ci}\frac{\beta}{2}(\sqrt{4H^2+L^2}-L) + \mathrm{Ci}\frac{\beta}{2}(\sqrt{4H^2+L^2}+L)\right] \\ &+ \cos\beta L[\mathrm{Ci}\beta(\sqrt{H^2+L^2}-L) + \mathrm{Ci}\beta(\sqrt{H^2+L^2}+L)] \\ &+ \sin\beta L[\mathrm{Si}\,\beta(\sqrt{H^2+L^2}+L) - \mathrm{Si}\,\beta(\sqrt{H^2+L^2}-L) \\ &\left. -2\,\mathrm{Si}\frac{\beta}{2}(\sqrt{4H^2+L^2}+L) + 2\,\mathrm{Si}\frac{\beta}{2}(\sqrt{4H^2+L^2}-L)\right]\Big\}\ \Omega \end{aligned} \tag{3.9}$$

and

$$
\begin{aligned}
X_{21} = 30\frac{1}{\sin^2(\beta L/2)}\Bigg\{ & -2(2+\cos\beta L)\,\mathrm{Si}\,\beta H \\
& + 4\cos^2\frac{\beta L}{2}\left[\mathrm{Si}\,\frac{\beta}{2}(\sqrt{4H^2+L^2}-L)+\mathrm{Si}\,\frac{\beta}{2}(\sqrt{4H^2+L^2}+L)\right] \\
& - \cos\beta L[\mathrm{Si}\,\beta(\sqrt{H^2+L^2}-L)+\mathrm{Si}\,\beta(\sqrt{H^2+L^2}+L)] \\
& + \sin\beta L[\mathrm{Ci}\,\beta(\sqrt{H^2+L^2}+L)-\mathrm{Ci}\,\beta(\sqrt{H^2+L^2}-L) \\
& -2Ci\frac{\beta}{2}(\sqrt{4H^2+L^2}+L)+2Ci\frac{\beta}{2}(\sqrt{4H^2+L^2}-L)\Bigg]\Bigg\}\ \Omega
\end{aligned}
\tag{3.10}
$$

where

$$
\overline{\mathrm{Ci}}x = \int_0^x \frac{(1-\cos u)}{u}du,\ \ \mathrm{Ci}(x) = -\int_x^\infty \frac{\cos(u)}{u}du,\ \ \mathrm{Si}(x) = \int_0^x \frac{\sin(u)}{u} \tag{3.11}
$$

These formulas are for a center-fed dipole antenna, where the current distribution is assumed to be sinusoidal. From [69, 70, 126], and other sources that may be found within these papers, it is known that only a dipole antenna of vanishing radius can have an exactly sinusoidally distributed current, but it has been shown to be a fair approximation for dipoles that are $\leq \lambda_0/2$ in length.

The real and imaginary components of Z_{D1}, Z_{21}, and Z_{S1} are plotted in Fig. 3.6 for two parallel half-wavelength dipoles, as a function of the spacing $H = 2h$ between them. It was shown earlier that such a system of dipoles is equivalent to a dipole arranged at a height h above an infinite metallic ground. Since the dipole antenna in this case is at $h = 1.6$ mm $= 0.015\lambda_0$ (at 2.6 GHz) above the ground, the corresponding equivalent value of the theoretical impedance for the dipole may be read at $H = 2h = 0.03\lambda_0$ in Fig. 3.6 (a) and (b). As it is the real part of impedance that contributes to radiation, and the imaginary part can be nullified through minor adjustments in the length of the dipole, the value of $Re\{Z_{D1}\}$ at $H = 2h = 0.03\lambda_0$ in Fig. 3.6 (a) is of primary interest. We can see that it is just 0.41 Ω.

A couple of points need to be considered at this junction. The curves presented in Fig. 3.6 are for a half-wavelength dipole made out of a perfectly conducting material, therefore, the plotted driving-point resistance, $Re\{Z_{D1}\} = R_{D1} = R_{rad,D1} + R_{loss}$, contains no contribution from any loss mechanism, i.e. $R_{loss} = 0$, and as a result the antenna radiation efficiency (excluding mismatch losses) would still be 100%. Here $R_{rad,D1}$ represents the radiation resistance part of the driving-point resistance. But there is no such thing as a perfect electric conductor in nature; a typical dipole antenna is made of copper wire which has an extremely high, but finite conductivity of $5.8 \cdot 10^7$ S/m, and therefore some loss is to be expected. Consider the simulated data in Table 3.1 for a half-wavelength dipole antenna at its resonance at ≈ 2.6 GHz. We can see that the conduction losses due to copper are extremely small, but when the antenna is situated closely above a ground plane, the driving-point radiation resistance becomes comparable to the loss resistance, leading to a significant drop in the radiation efficiency. (The loss resistance could be isolated by comparing the simulated input resistance of a perfect electric conductor based dipole to that of a copper based dipole, all other things being constant.)

The situation does not appear dire due to the still sufficient radiation efficiency above the ground, and one may think that matching the low driving-point impedance

TABLE 3.1: Simulated resistance values for a half-wave dipole antenna of length = 55.7 mm, radius = 0.2 mm, feed gap width = 0.2 mm, resonant at 2.6 GHz.

Dipole location	Dipole material	$R_{rad,D1}$ (Ω)	R_{loss} (Ω)	Radiation efficiency (%)
Free space	Perfect electric conductor	71	0	100
Free space	Copper	71	0.3	$\approx$ 100
1.6 mm above infinite ground	Copper	0.45	0.3	60

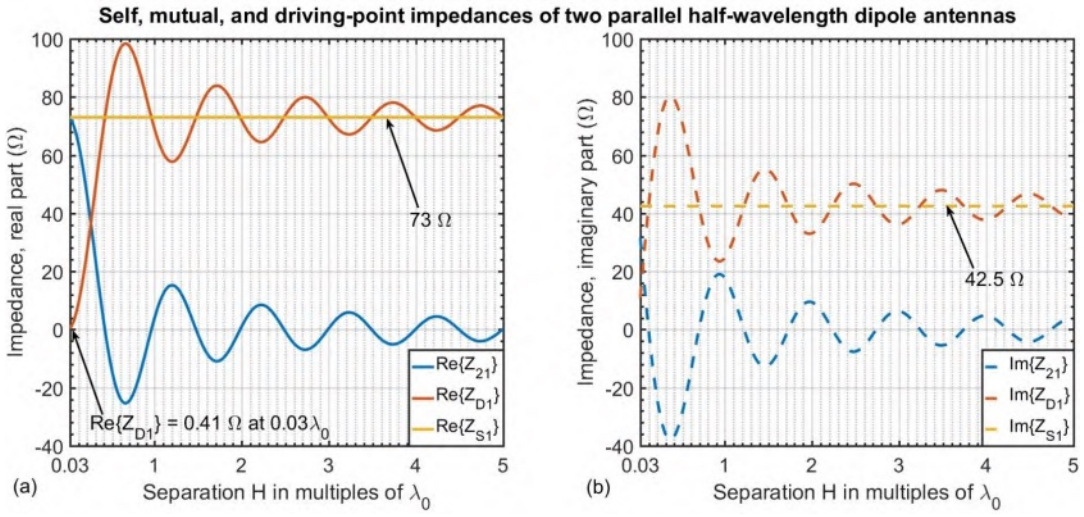

FIGURE 3.6: (a) and (b) present the theoretical real and imaginary components of Z_{D1}, Z_{21}, and Z_{S1} for two parallel half-wavelength dipoles as a function of the separation H between them, and have been plotted using equations 3.6...3.10 [68, 127]. The dipoles are assumed to be made up of perfect electric conductor.

to 50 Ω would make the antenna usable. But such a matching is not practically feasible, as it would require a matching network with unrealisable inductance/capacitance values. Even if hypothetically the matching were possible, the achieved impedance bandwidth would be extremely narrow, as firstly, L-C networks are inherently narrow band, and secondly, a low driving-point resistance of the antenna is indicative of a large Q-factor [71]. In addition, only copper losses were considered until now; the dipole antenna may be printed on a substrate material, in which case the dielectric losses will further deteriorate the radiation efficiency. Therefore, a method needs to be found that raises the driving-point radiation resistance component of the driving-point resistance of a dipole antenna located closely above a ground plane.

One solution to this problem is to recognize the fact that no matter how small, as long as $h \neq 0$, the value $Re\{Z_{D1}\} = Re\{(Z_{S1} - Z_{21})\}$ remains finite and positive. We just need to make this difference sufficiently larger at $H = 2h = 0.03\lambda_0$. Going back to Fig. 3.6 (a), if the difference were 100...120 times larger, then $Re\{Z_{D1}\}$ at that H would lie between 41...49 Ω, in which case the antenna would not need any impedance matching network. Of course, Fig. 3.6 assumes a lossless antenna, but, as we will see soon, a substantial increase in the driving-point radiation resistance of a copper antenna does not correspond to a substantial increase in the loss resistance.

In this regard, let us take a look at the folded dipole antenna [72] as sketched in Fig. 3.7 (a). Its operation may be understood by decomposing the current into two distinct modes: a transmission line mode, and an antenna mode. Assuming Z_{SF} to be the self-impedance of the half-wavelength folded dipole, it can be shown that:

$$Z_{SF} = q^2 \cdot Z_{S1}\ \Omega \tag{3.12}$$

where q represents the number of branches in the folded dipole, and Z_{S1} is the self-impedance of a typical half-wavelength dipole.

Furthermore, the results of [73] regarding the mutual impedance between between two $q = 2$ parallel half-wavelength folded dipoles with a separation H between them could be easily generalized (see appendix I), and an expression for the mutual impedance, Z_{21F}, for any $q \geq 2$ could be obtained:

$$Z_{21F} = q^2 \cdot Z_{21}\ \Omega \tag{3.13}$$

where Z_{21} is the mutual impedance between two typical half-wavelength dipoles at a distance H from each other, as computed in Fig. 3.6.

Then considering eq. 3.12 and 3.13, and substituting from eq. 3.6, the driving-point impedance, Z_{DF} of the folded dipole at a distance $h = H/2$ from an infinite metallic ground may be written as:

$$Z_{DF} = (Z_{SF} - Z_{21F}) = q^2 \cdot (Z_{S1} - Z_{21}) = q^2 \cdot Z_{D1}\ \Omega \tag{3.14}$$

Therefore, with $q = 10$, at $h = H/2 = 0.015\lambda_0$ above an infinite ground, a half-wavelength folded dipole will theoretically offer a 100 times larger driving-point impedance compared to a typical centre-fed half-wavelength dipole antenna. As shown in Fig. 3.7 (b), such a folded dipole was designed, simulated and compared to a patch antenna of the same dimensions. In comparison to the theoretically expected driving-point resistance of 41 Ω for the folded dipole (100 times the value indicated in Fig. 3.6 (a)), the simulated driving-point resistance amounted to 64 Ω. The difference between the expected value from the formula and the simulated value may be understood by considering that these formulas hold for a dipole antenna of vanishing radius, and in the case of folded dipole antennas, the various arms of the folded dipole are assumed to be resonant in the same phase. However, as dipole radius is always finite, and the various arms in the case of a folded dipole antenna will have some phase difference relative to each other, the resulting driving-point impedance is expected to deviate from the theoretical prediction.

The reflection coefficients are compared in Fig. 3.7 (c). The typical half-wavelength dipole had a poor impedance matching to 50 Ω, but the folded dipole and the patch were well matched, which is in accordance with their corresponding driving-point resistances. The antennas in these simulations were made of perfect electric conductor.

TABLE 3.2: Simulated resistance values at the resonance for a half-wave dipole antenna and a folded dipole antenna made of copper and located 1.6 mm above an infinite ground.

Dipole type	Dipole material	$R_{rad,D1}$ (Ω)	R_{loss} (Ω)	Radiation efficiency (%)
Typical	Copper	0.45	0.3	60
Folded (10 arms)	Copper	64	3	≈ 95.5

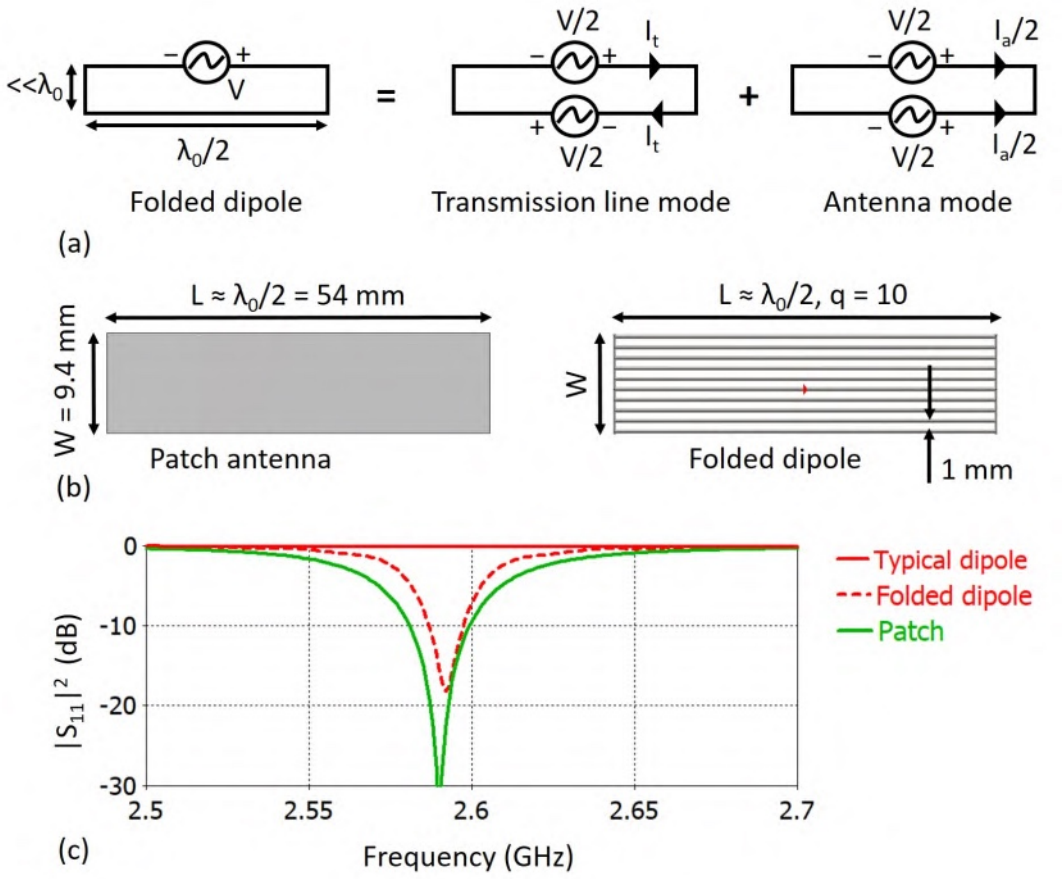

FIGURE 3.7: (a) Theoretical model of a folded dipole [72]. (b) Dimensions of the simulated half-wavelength patch and folded dipole with $q = 10$. (c) Simulated reflection coefficients. The antennas are made out of perfect electric conductor.

Next, the material of the folded dipole was changed to copper and the simulation was repeated. It was noticed that the driving-point resistance amounted this time to 67 Ω, which implied that the loss resistance due to copper was just 3 Ω. Now looking at the data in Table 3.2, we observe what was pointed out earlier; a large growth in the driving-point radiation resistance does not imply a large growth in the loss resistance. This also makes intuitive sense, because at the same frequency, the radiation resistance of a dipole grows as L^2, while the loss resistance scales as L. The considered folded dipole had 10 arms, and was therefore 10 times longer than the typical dipole at the same frequency. This led to a somewhat larger than a 100 fold radiation resistance (difference between theory and reality), but the loss resistance grew only 10 fold.

The electric field distributions and the radiation patterns for the half-wavelength folded dipole and the patch antenna matched the ones presented in Fig. 3.5 (a). Also at $3\lambda_0/2$ length, there was a one-to-one correspondence between the patch antenna results and folded dipole antenna results at 2.6 GHz, similar to the case in Fig. 3.5 (c). However, it was at $(2p)\lambda_0/2$ lengths that the similarity between the electric fields and the radiation patterns of the patch antenna and the typical centre-fed dipole antenna fell away (Fig. 3.5 (b)). So, as the next step, the field distributions and radiation patterns were compared at 2.6 GHz at $p = 2$ for the patch antenna and the folded dipole antenna . The results are presented in Fig. 3.8. There was a good

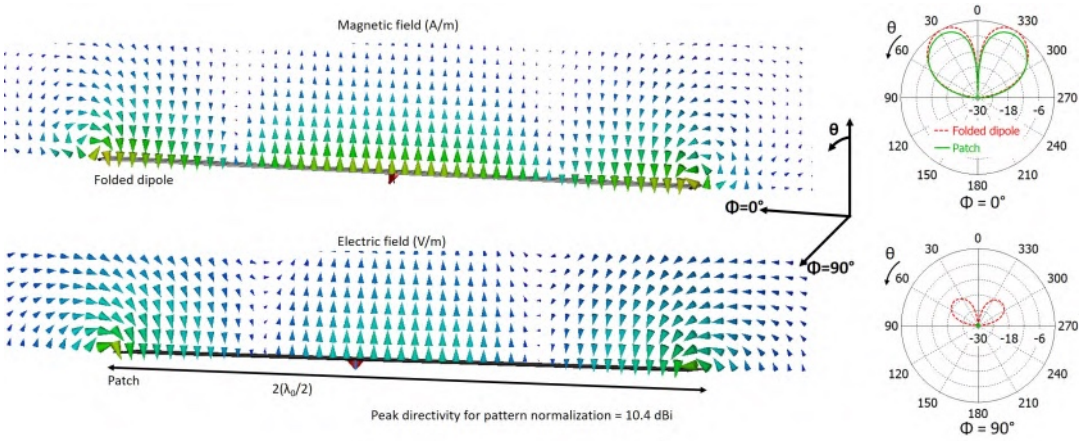

FIGURE 3.8: Comparison of the magnetic/electric field distributions and the normalized radiation patterns for a folded dipole antenna and patch antenna of length $2(\lambda_0/2)$. The comparison is at 2.6 GHz. The antennas lie in the $\theta = 90^\circ$ plane, 1.6 mm above a perfect electric boundary, and are oriented along the $\phi = 0^\circ$ axis.

agreement between the radiation patterns at this even mode, but it was the magnetic field of the folded dipole and the electric field of the patch antenna that were similarly distributed. Further higher even modes were not analyzed, but it is reasonable to expect that the trend may continue like this between a patch antenna and a folded dipole, that the radiation patterns are comparable at all modes, but orthogonal to one another at even modes.

At this point, it must be reiterated that the question of whether a folded dipole antenna could be used above a ground plane was actually first considered in [74], but the author was mainly interested in showing if a folded dipole with a certain number of arms could radiate efficiently closely above a ground plane; no clear explanation with which the requisite number of arms could be estimated in relation to the antenna distance above the ground was presented. This thesis fills out that gap by a very nominal generalization of the result in [73] (see appendix I), that leads to equation 3.14. In order to obtain $Re\{Z_{DF}\} \approx 50\ \Omega$ for a folded dipole antenna closely above a ground plane, one simply needs to consult the value of $Re\{Z_{D1}\}$ at that separation from the ground plane from Fig. 3.6 (a). Subsequently, it is simple to choose a q, such that $Re\{Z_{DF}\} = q^2 \cdot Re\{Z_{D1}\} \approx 50\ \Omega$. Additionally considered in this thesis was the question of how closely a folded dipole represents an equivalent to a typical patch antenna at different harmonic lengths. Furthermore, a closer look into the influence of copper losses on the performance of the folded dipole was taken.

In the view of the observations presented above, if we restrict ourselves to the fundamental mode operation of a patch antenna, then with reference to the radiation pattern, both the typical half-wavelength dipole and half-wavelength folded dipole form good equivalent models to a patch. But if we also want reflection coefficient equivalence, then the half-wavelength folded dipole compares overall better to a patch antenna. It becomes obvious through this discussion that just like a half-wavelength dipole/folded dipole models a patch antenna, a one-wavelength dipole antenna should be a reasonable model for the di-patch antenna that also measures one-wavelength in length. This is discussed in the next section and it is shown how one can modify the driving point impedance of a one-wavelength dipole antenna so that it becomes usable closely above a metallic ground.

3.2.3 One-wavelength dipole above metal ground and di-patch equivalence

The equations 3.7...3.10 assume a sinusoidal current distribution on the dipole antenna. The problem with this assumption appears when calculating the input impedance of dipole antennas of lengths $L = (2p)\lambda_0/2$. As soon as $L = \lambda_0$ is plugged into equations 3.1..3.10, the value that is returned is infinity, independent of the dipole wire radius. But in reality, no full-wavelength dipole antenna of a finite wire radius has an infinite input impedance; it runs into thousands of ohms, but never infinite. Therefore, the equations 3.7...3.10 are insufficient for characterizing the impedance behavior of a full-wavelength electrical dipole antenna.

The equations that come up ahead will rectify the aforementioned problem, and will be applicable to thin dipole antennas of any length. The ultimate aim of this exercise is to compute the theoretical driving-point impedance of a full-wavelength dipole antenna closely above a ground and compare it to the corresponding values obtained from simulations. This would highlight the discrepancy mentioned in the introduction of this chapter, that the simulated driving-point impedance of a full-wavelength dipole above a ground plane runs into thousands of ohms and does not drop to zero as the theory predicts. Subsequent to this observation, the full-wavelength dipole antenna design could be modified (to the di-patch antenna), such that impedance closely above the ground plane dropped down to 50 Ω from several thousands ohms.

Moving onto the topic of the improvised impedance equations for a dipole antenna, Hallén did not make any assumptions about the current distribution on finite-radius cylindrical dipole antennas, but treated such dipoles as a boundary value problem, as mentioned in [67, 126]. This resulted in the following general formula for the self-impedance of a centre-fed cylindrical dipole antenna:

$$Z_{S1} = -j60\tau \left\{ \frac{\cos \beta L/2 + \alpha_1/\tau + \alpha_2/\tau^2 + \cdots}{\sin \beta L/2 + \zeta_1/\tau + \zeta_2/\tau^2 + \cdots} \right\} \ \Omega \tag{3.15}$$

where $\tau = 2ln(L/a)$, and α_1 and ζ_1 are defined as:

$$\begin{aligned} \alpha_1 &= \alpha_1^{\mathrm{I}} + j\alpha_1^{\mathrm{II}} \\ \alpha_1^{\mathrm{I}} &= (1/2)[\cos \beta L/2(\overline{\mathrm{Ci}}2\beta L - 2\overline{\mathrm{Ci}}\beta L) - \sin \beta L/2\,\mathrm{Si}\,2\beta L] \\ \alpha_1^{\mathrm{II}} &= (1/2)[\cos \beta L/2(\mathrm{Si}2\beta L - 2\mathrm{Si}\beta L) + \sin \beta L/2\overline{\mathrm{Ci}}2\beta L] \end{aligned} \tag{3.16}$$

and

$$\begin{aligned} \zeta_1 &= \zeta_1^{\mathrm{I}} + j\zeta_1^{\mathrm{II}} \\ \zeta_1^{\mathrm{I}} &= (1/2)[\cos \beta L/2(4\,\mathrm{Si}\,\beta L/-\mathrm{Si}2\beta L) + \sin \beta L/2\left(2\overline{\mathrm{Ci}}\beta L - \overline{\mathrm{Ci}}2\beta L + 4\log_{\mathrm{e}} 2\right)] \\ \zeta_1^{\mathrm{II}} &= (1/2)[\cos \beta L/2(\overline{\mathrm{Ci}}2\beta L - 4\overline{\mathrm{Ci}}\beta L) + \sin \beta L/2(2\,\mathrm{Si}\,\beta L - \mathrm{Si}\,2\beta L)] \end{aligned} \tag{3.17}$$

The components taking into account the internal impedance per unit length of a cylindrical conductor have not been included in equations 3.16 and 3.17 as they are sufficiently small to be negligible for most practical purposes.

Provided $1/\tau$ is small but finite, i.e. the radius of the dipole is much smaller compared to its length, the condition in equation 3.18 is a reasonable approximation.

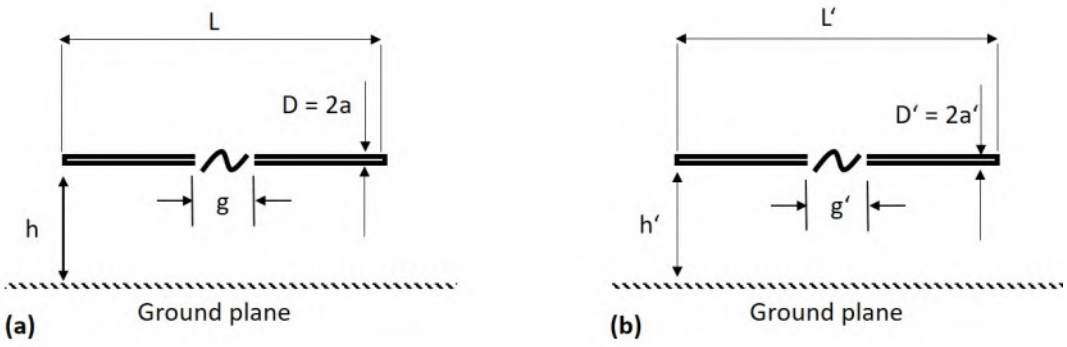

FIGURE 3.9: (a) Dipole 1 is a half-wavelength dipole, h wavelengths above an infinite ground plane. (b) Dipole 2 is a one-wavelength dipole, h' wavelengths above an infinite ground.

TABLE 3.3: Specifications of the dipoles in Fig. 3.9. The resonance frequencies and impedances are simulated free-space values.

Dipole 1					
L = $\lambda_0/2$ (mm)	a (mm)	g (mm)	Frequency corresponding to λ_0 (GHz)	Resonance (fundamental) (GHz)	Impedance at resonance (Ω)
52.5	0.35	1.05	2.84 GHz	2.6	67

Dipole 2					
L' = $\lambda_0^{'}$ (mm)	a' (mm)	g' (mm)	Frequency corresponding to $\lambda_0^{'}$ (GHz)	Resonance (2^{nd} order) (GHz)	Impedance at resonance (Ω)
87.9	0.59	0.87	3.41	2.6	778

$$\begin{aligned} |\cos \beta L/2 + \alpha_1/\tau| &\gg |\alpha_2/\tau^2| \\ |\sin \beta L/2 + \zeta_1/\tau| &\gg |\zeta_2/\tau^2| \end{aligned} \tag{3.18}$$

Subject to this condition, the real and imaginary parts of equation 3.15 may be written as:

$$R_{S1} = 60\tau \left\{ \frac{\alpha_1^{\mathrm{II}} \left(\tau \sin \beta L/2 + \zeta_1^{\mathrm{I}}\right) - \zeta_1^{\mathrm{II}} \left(\tau \cos \beta L/2 + \alpha_1^{\mathrm{I}}\right)}{\left(\tau \sin \beta L/2 + \zeta_1^{\mathrm{I}}\right)^2 + \left(\zeta_1^{\mathrm{II}}\right)^2} \right\} \Omega \tag{3.19}$$

$$X_{S1} = -60\tau \left\{ \frac{\left(\tau \cos \beta L/2 + \alpha_1^{\mathrm{I}}\right) \left(\tau \sin \beta L/2 + \zeta_1^{\mathrm{I}}\right) + \alpha_1^{\mathrm{II}} \zeta_1^{\mathrm{II}}}{\left(\tau \sin \beta L/2 + \zeta_1^{\mathrm{I}}\right)^2 + \left(\zeta_1^{\mathrm{II}}\right)^2} \right\} \Omega \tag{3.20}$$

The equations 3.19 and 3.20 are a better approximation to the self-impedance in comparison to the equations 3.7 and 3.8, and are valid for thin cylindrical dipole antennas of any electrical length. Blake [67], for example, analyzed antennas for $10 \leq \tau \leq 30$. For larger wire radii, higher powers (≥ 2) of $1/\tau$ will not be negligible any more.

Now, consider two dipole antennas as in Fig. 3.9 with $\tau = 10$, both resonant in free-space (ground planes absent in this case) at ≈ 2.6 GHz, but in the fundamental mode and the second harmonic mode respectively. We know that the actual length

of a half-wavelength/full-wavelength dipole antenna is shorter than the exact half-wavelength/full-wavelength corresponding to its resonant frequency. This is also evident from the simulated data presented in Table 3.3. The length of dipole 1, L = 52.5 mm corresponds to an exact half-wavelength at 2.84 GHz, whereas its fundamental resonance is at 2.6 GHz. Similarly, the length of dipole 2, L = 87.9 mm corresponds to an exact wavelength at 3.41 GHz, but its second harmonic resonance lies at 2.6 GHz. We can notice that the shortening in length in case of second-order resonance is more significant than in case of fundamental resonance. These free-space simulated resonance values and impedances are well aligned with the theoretical values presented in [76] for a dipole antenna with the same τ (see Fig. 1 in [76]).

We would now like to know the impact on the driving-point resistance of these antennas if they are brought close to a ground plane. Given R_{S1} from equation 3.15, R_{21} is needed to compute the driving-point resistance R_{D1}. Tai [75], improving upon the results in [69], derived the first order driving-point impedance, $Z_{D1} = Z_{S1} - Z_{21}$, of two parallel anti-symmetrically driven dipole antennas at a distance $H = 2h$ from each other (refer Fig. 3.9, apply image theory) as in equation 3.21. The expanded expressions for κ_1 and ρ_1 can be found in the mentioned reference (see equation 63 in [75] and the associated text that leads to the anti-symmetrically driven case for two parallel dipoles).

$$Z_{D1} = -j60\psi \left\{ \frac{\cos \beta L/2 + \frac{1}{\psi}(\alpha_1 - \kappa_1)}{(2 - \frac{\tau}{\psi}) \sin \beta L/2 + \frac{1}{\psi}(\zeta_1 - \rho_1)} \right\} \ \Omega \tag{3.21}$$

where, in the case that the two dipole antennas are closely coupled, [75] defines $\psi = 2ln(\frac{H}{a})$ (see equation 38 in [75]).

Let us now take a look at the various parts in Fig. 3.10 one after the other. Fig. 3.10 (a) compares the theoretical driving-point radiation resistance from equation 3.21 to its simulated counterpart for dipole 1 lying h wavelengths above an infinite ground plane. The driving-point radiation resistance is considered at 2.84 GHz, at which dipole 1 is exactly half-wavelength long, and therefore not resonant. There is some disagreement between the results, particularly at larger distances from the ground, but nothing too drastic. On the other hand, the corresponding theoretical and simulated driving-point radiation resistances for the one-wavelength dipole, dipole 2, in Fig. 3.10 (b) seem to have more significant differences. The simulated resistance curve is flatter in profile; the antenna would need to be insensibly close to the ground, for the simulated curve to drop to 0 Ω. In any case, for an antenna, we are more interested in the driving-point resistance at the resonance, because we operate antennas at their resonance frequency. If we shift our attention to Fig. 3.10 (c), we can notice that the simulated driving-point resistance at the fundamental resonance of dipole 1 follows a similar trend to Fig. 3.10 (a). But there was no such correspondence at all between Fig. 3.10 (b) and Fig. 3.10 (d), that depicts the simulated driving-point resistance of dipole 2 at its second harmonic resonance. At the second harmonic resonance, the driving-point resistance was extremely high closely above a ground plane. These were very interesting observations, and form partially the basis of why and how the di-patch antenna functions. Fig. 3.10 (e) and (f) represent the fundamental resonance and second order resonance frequencies of dipole 1 and dipole 2 respectively. We can observe that the resonance frequency is influenced by the distance between the ground plane and the antenna, therefore it was not possible to use equation 3.21 to produce theoretical driving-point resistance curves in Fig 3.10 (c) and (d). The frequency at which a dipole is exactly a half-wavelength or a full-wavelength in length remains the same irrespective of how close the antenna is to

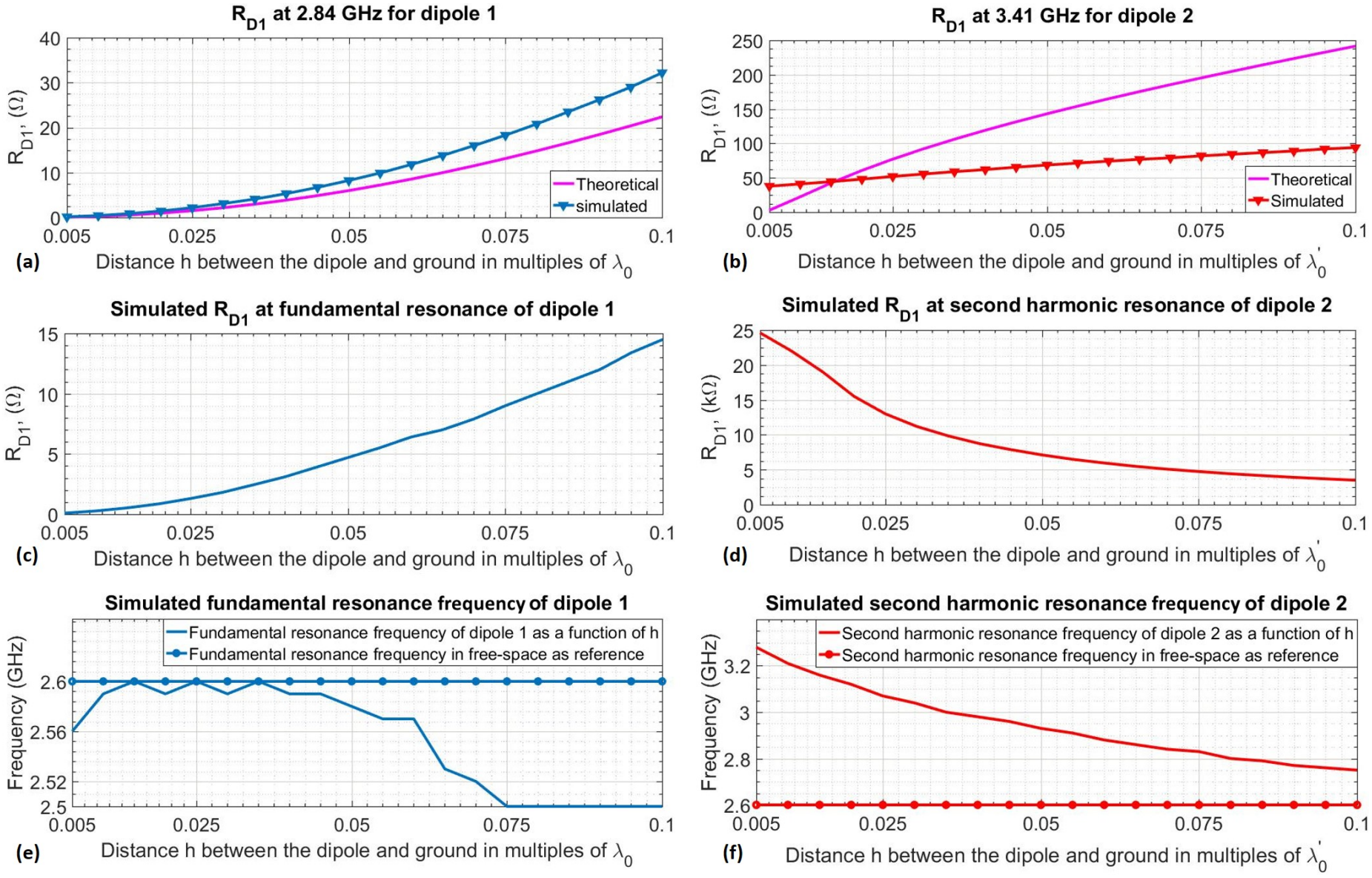

FIGURE 3.10: As a function of the distance between the antenna and the ground: (a) Simulated and theoretical driving-point resistance at the exact $\lambda_0/2$ frequency for dipole 1. (b) Simulated and theoretical driving-point resistance at the exact $\lambda_0^{'}$ frequency for dipole 2. (c), (d) Simulated driving-point resistance at the fundamental/second resonance of dipole 1/dipole 2. (e), (f) Fundamental/second resonance frequency of dipole 1/dipole 2.

the ground, because the actual length of the antenna remains unchanged, and therefore equation 3.21 could be readily applied for obtaining theoretical curves as in Fig. 3.10 (a) and (b). While the results in the above figures pertain to cylindrical dipole antennas, they are also applicable to strip-dipole antennas. A strip dipole, where strip width is small compared to strip length, is electrically equivalent to a cylindrical dipole of radius equal to one-fourth the strip width [77]. This is important, because as we will see ahead, as a planar antenna, the di-patch is an evolution from a full-wavelength strip-dipole, and not a cylindrical dipole.

From full-wavelength dipole to di-patch: Coming back to Fig. 3.10 (c) and (d), there is a stark contrast in the resistance behavior at the fundamental resonance and the second harmonic resonance with the antenna above a ground plane. To operate a dipole antenna in fundamental mode closely above a ground plane, we need to raise its driving-point resistance from nearly 0 Ω to 50 Ω, which may be achieved by considering the idea of folded dipoles as in the last section. However, at the second harmonic resonance, the driving-point resistance needs to be lowered from an exorbitant value to 50 Ω, and this could be achieved in a surprisingly rather simple manner which resulted in the so-called di-patch antenna. For this we need to shift our focus to the three full-wavelength antennas presented in Fig. 3.11 (a) and their corresponding $\angle Z_{D1}$ versus frequency curves. All three cases have one common zero-crossing/resonance at point P1. The antennas lie 1.6 mm above an infinite ground plane, with vacuum as the in-between substrate. Case 1 represents a very narrow full-wavelength strip-dipole antenna, and as expected from the previous results, the driving-point resistance, $Re\{Z_{D1}\}$, at P1 was extremely high. It was found that by broadening the arms of the thin lambda dipole as in case 2, $Re\{Z_{D1}\}$ was drastically reduced to 370 Ω, but not yet low enough for a good impedance match. Before widening the arms further, we wanted to see if the port location had an influence on the impedance matching. It was very interesting to note that as the differential port was shifted from the centre in case 2, to the antenna corners in case 3, an additional zero-crossing point P2 appeared in the phase curve, where $Re\{Z_{D1}\}$ was 50 Ω. To summarize, looking at case 1 and case 3 in Fig. 3.11 (a), it is clear that if the di-patch becomes too thin, the point P2 will be lost. Therefore the di-patch must be broad, and considering cases 2 and 3, it must be fed at its corners to obtain the point P2. One could argue that if the centre-fed antenna in case 2 was made even broader, the input impedance would reduce further, and probably a good match to 50 Ω could be obtained. However, such a step, even if successful, would make the antenna unnecessarily larger in size. Besides, centre-feeding the antenna in case 2 is impractical, while corner feeding is straightforward.

From the point of view of electric field distributions and radiation patterns, the thin full-wavelength strip-dipole of case 1 is itself a good equivalent to the di-patch antenna of case 3. This is evident if we compare the electric field distributions of the two antennas in Fig. 3.11 (b) and (c), and the normalized patterns of the directivities in Fig. 3.11 (d) and (e). In both cases, the peak directivity and gain were $\approx$ 10.5 dBi, as there were no lossy materials in these simulation models. The directivity and electric field at the point P1 for case 1 was compared to the directivity and electric field at point P2 for case 3, whereby these results at the points P1 and P2 for case 3 were essentially indistinguishable, except for the difference in the driving-point resistance. Further, in Fig. 3.11 (f), the reflection coefficient of the di-patch antenna is presented. While vacuum substrate can be closely approximated by air, there is no such thing as an infinite ground plane in reality. Therefore, the curves 2 and 3 in Fig. 3.11 (f) present the reflection coefficient for a more realistic electrically large ground plane measuring $5\lambda \times 5\lambda$, and additionally for a $\lambda \times \lambda/2$ ground plane, i.e., with exactly the

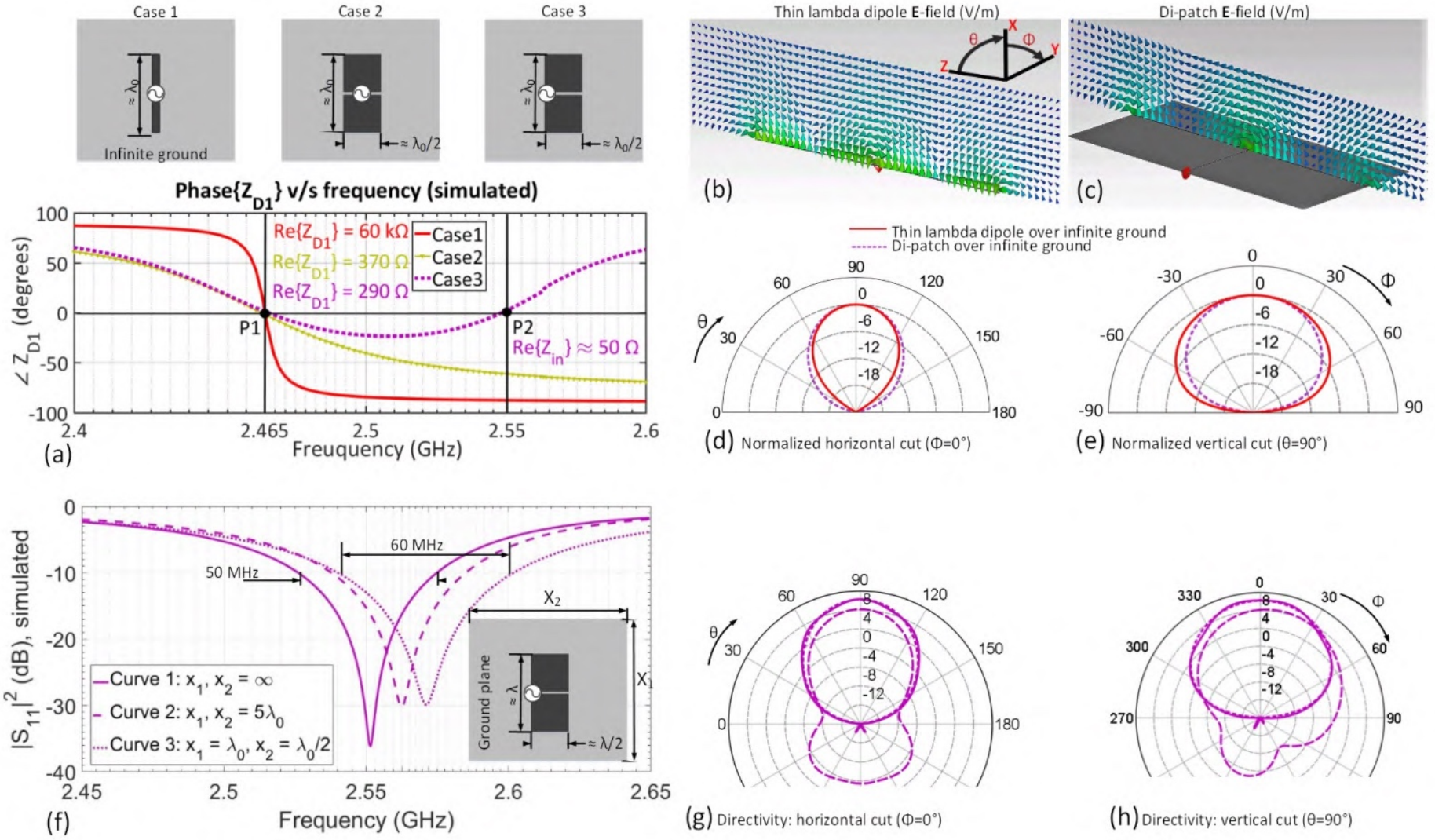

FIGURE 3.11: (a) Different antenna configurations 1.6 mm above an infinite ground, and their phase-frequency curves. (b), (c) Comparison of the E-field distributions of a thin one-wavelength dipole and the di-patch antenna. (d), (e) Comparison of the corresponding normalized directivity patterns. (f) Simulated reflection coefficients for a di-patch with different ground plane sizes. (g), (h) Unnormalized directivity patterns for the various ground plane sizes.[54] ©2019 IEEE

same surface area as the two overlying patches, in comparison to reflection coefficient with the infinite ground plane in curve 1. It may be seen from curve 1 to curve 3, there was only a minor 20 MHz shift of the resonance frequency, and the impedance bandwidth remained essentially unchanged. As expected, due to diffraction at the edges of the smaller ground plane for curve 3, the directivity dropped from 10.5 dBi to 8.5 dBi, as seen in Fig. 3.11 (g) and (h). Overall, these considerations make the di-patch configuration for curve 3 the most interesting, due to the practical corner feeding, no loss in bandwidth, the smallest ground, thus the smallest footprint area, yet a relatively high directivity and front-to-back ratio (≈11 dB).

A centre-fed full-wavelength dipole antenna finds by-and-large no practical application, because of its high self impedance at resonance, as demonstrated in Table 3.3 for dipole 2. However, the presented analysis that closely above a ground plane, a full-wavelength dipole is perfectly usable, as long as it is designed as in case 3 in Fig. 3.11 (a). This is the primary significance of these results, in that a design configuration was found in which a previously unused antenna type becomes usable. In addition, the di-patch antenna has size and bandwidth advantages over typical patch antennas, as will be shown later.

3.3 Sensitivity analysis and bending tolerance

Several samples of a di-patch antenna that was resonant at 2.45 GHz in simulations were printed using an in-house PCB printer [78]. The simulated di-patch antenna model is presented along with its dimensions in Fig. 3.12 (a). The di-patch antenna was printed on a standard $\approx$ 1.5 mm thick FR-4 substrate with ϵ_r = 4.4 and $\tan\delta$ = 0.023 at 0.5 GHz. The top and bottom copper layers were 0.035 mm in thickness, bringing the total thickness of the antenna to $\approx$ 1.6 mm. A printed sample of the di-patch antenna is presented in Fig. 3.12 (b). A suitable balun [79] was soldered at the foot-point of the di-patch so as to be able to feed it a coaxial cable. On measuring the antenna reflection coefficient, it was seen that the resonance frequency was shifted to 2.55 GHz. This could be due to a disagreement between the simulated antenna dimensions and the dimensions of the milled version, or due to the substrate permittivity being different from the data sheet value.

To ascertain the reason for this frequency shift, the sensitivity of the reflection coefficient to small changes in the various di-patch antenna design parameters was analyzed in simulations. To determine the amount by which to vary the antenna dimensions in the simulation, the dimensions of the manufactured sample were measured under an optical profilometer with an accuracy $>$ 0.001 mm, and it was observed that the sample dimensions were off by $\approx$ 0.03 mm compared to the simulations. For example, fig. 3.12 (c) shows the slit in the middle of the di-patch under 10x magnification, and we can see that it measured 0.23 mm across, rather than 0.2 mm as in the simulation. Therefore, keeping other parameters constant, first the slit width was increased in the simulation, and then overall di-patch antenna size was increased by 0.03 mm. The effects of these two variations on the simulated reflection coefficient are presented in Fig. 3.12 (d) and 3.12 (e), and we can observe that there was hardly any impact on the reflection coefficient; these dimension variations are simply too small to be critical. This left the substrate permittivity as responsible for the discrepancy in between the simulation and the measurement.

Let f_{sim} = 2.45 GHz represent the simulated resonant frequency, and f_{meas} = 2.55 GHz represent the measured resonant frequency, then we may write

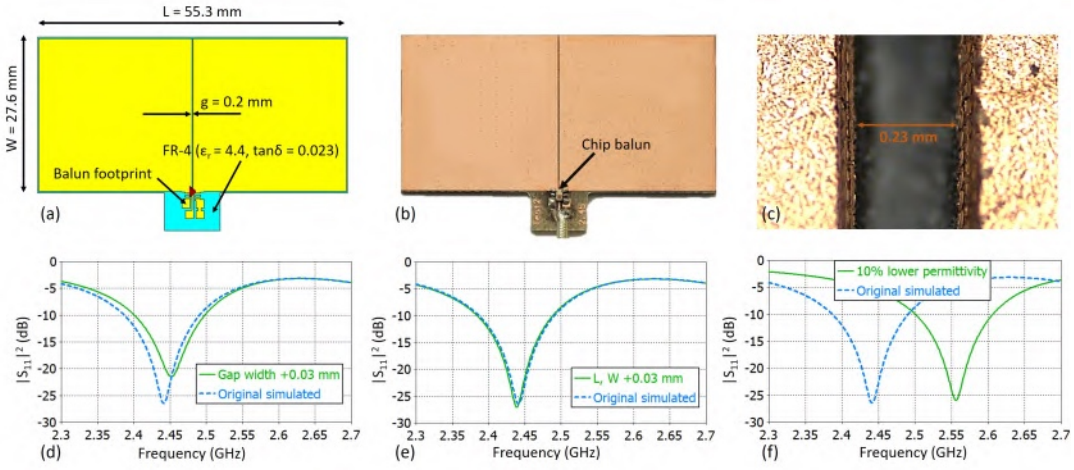

FIGURE 3.12: (a) Dimensions of the simulated di-patch antenna. (b) Manufactured di-patch antenna prototype with the soldered chip balun. (c) Slit width measured under 10X magnification using an optical profilometer. (d), (e), (f) Influence of gap width, (L, W), and substrate permittivity variation on the antenna reflection coefficient.

$$\frac{f_{sim}}{f_{meas}} = \frac{\sqrt{\epsilon_{meas}}}{\sqrt{\epsilon_{sim}}} \tag{3.22}$$

On solving this equation we find that $\epsilon_{meas} \approx 4$, and indeed on setting the relative permittivity to 4, the simulated resonance frequency shifted to 2.55 GHz, as represented in Fig. 3.12 (f). Given that the antenna is insensitive to small variations in its dimensions, and higher printing accuracies than ours are available in the market, it is most sensitive to substrate permittivity variations. This could also be potentially mitigated by using higher quality, and costlier substrate materials.

Next, the di-patch antenna was bent along its length and its width to demonstrate its suitability for conformal applications. The antenna was bent around an imaginary cylinder of radius r, as indicated in Fig. 3.13 (b) and (c). Consider first the bending along the length L. To completely wrap the di-patch antenna around the cylinder, the perimeter, $2\pi r$, of the cylinder should equal the length L of the di-patch. We denote the cylinder radius that achieves this as $r_{min,L}$, and it equals $L/2\pi$, which is 8.8 mm, given that L = 55.3 mm. Fig. 3.13 (d)...(f) show the electric field distribution across the length of the unbent di-patch antenna, and the same antenna bent in accordance with cylinder radii of $3.4 \cdot r_{min,L}$ and $1.7 \cdot r_{min,L}$. We can see from Fig. 3.13 (g), that a decrease in the cylinder radius accompanies a leftward shift of the di-patch resonance frequency. The 10 dB impedance bandwidth at r = 30 mm was only 20 MHz narrower than the unbent di-patch impedance bandwidth of 104 MHz. Only for an extreme bend as in Fig. 3.13 (f) was a -10 dB reflection coefficient not achievable. Next to the the reflection coefficients are the corresponding normalized patterns of directivity. Each pattern was normalized to its own maximum directivity, so as to easily compare the relative differences in the shapes of the patterns. Unless otherwise stated, this is how the radiation patterns will be compared in the remainder of this work; the peak values of the directivities and gains for the individual patterns will be specified in a separate, accompanying table. What is particularly noticeable in Fig. 3.13 (h) and (i) is that the front-to-back ratio is better for r = 30 mm, compared to the original.

For bending the di-patch along its width, $r_{min,W}$ was determined to be 4.5 mm, given that W = 27.6 mm. Fig. 3.13 (j)...(l) show the electric field distribution across the

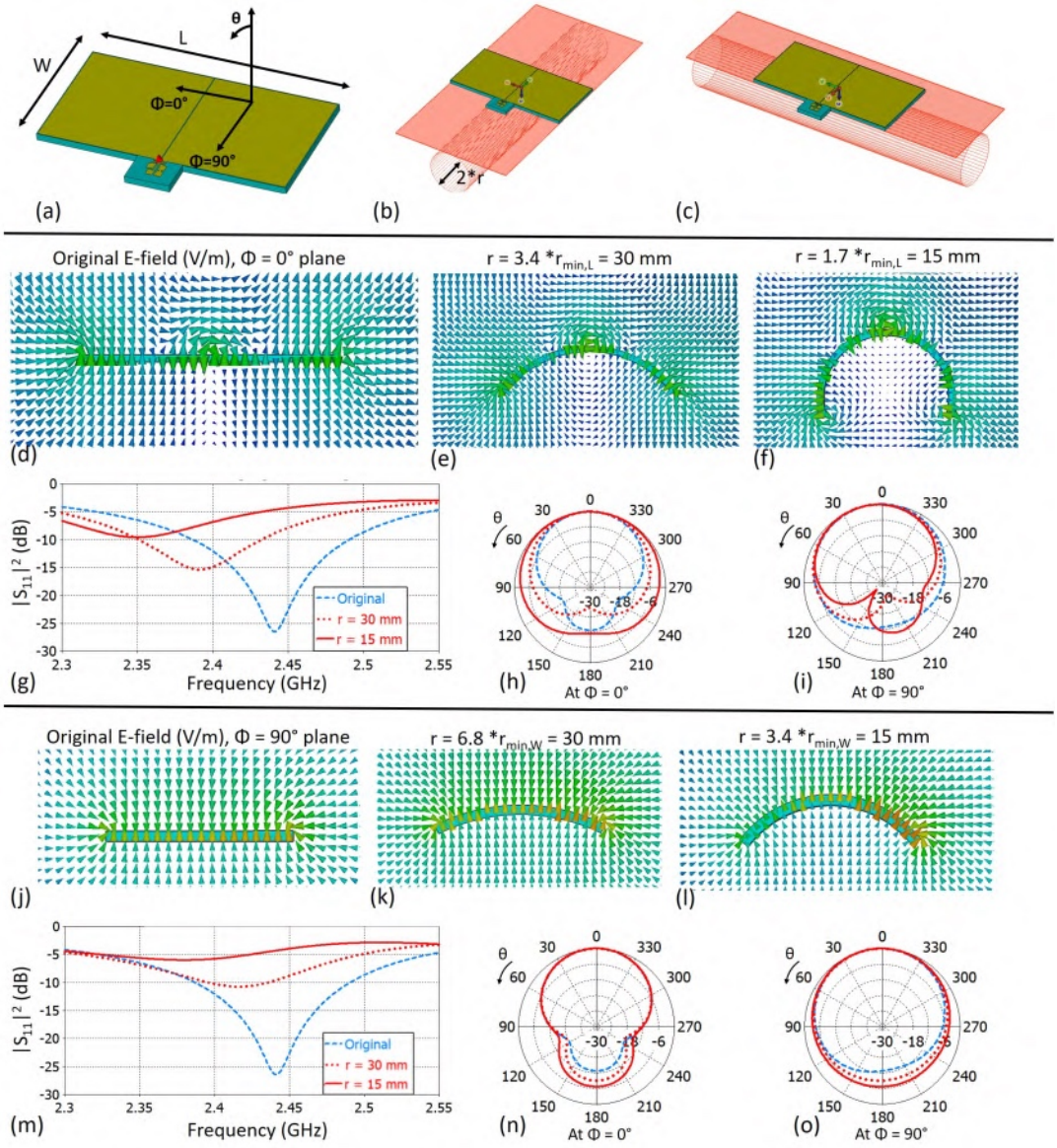

FIGURE 3.13: (a) Di-patch antenna with the reference coordinate system. (b), (c) Virtual cylinder of radius r for bending the di-patch along its length or width. (d) Reference E-field distribution along the length of the di-patch. (e), (f) E-field distribution for bending along the length. (g), (h), (i) The corresponding reflection coefficients and normalized directivity patterns. (j) Reference E-field along the di-patch width. (k)...(o) Results for bending along the width.

width of the unbent di-patch antenna, and the same antenna bent in accordance with cylinder radii of $6.8 \cdot r_{min,W}$ and $3.4 \cdot r_{min,W}$. The reflection coefficients corresponding to these antenna variants are plotted in Fig. 3.13 (m). One can notice that compared to bending along the length, the deterioration in the reflection coefficient is more rapid in this case; at a large r = 30 mm, a 10 dB impedance bandwidth of 41 MHz was obtained, and for lower radii a -10 dB reflection coefficient could not be attained. Unlike the last case, the normalized directivity patterns were closely comparable in shape in the upper hemisphere, but, there was a consistent deterioration in the front-to-back ratio on moving to lower radii.

The peak directivities, peak realized gains and total antenna efficiencies of the bent

TABLE 3.4: Simulated data for the bent di-patch antenna variants.

Bend type	Bending radius r (mm)	Directivity (dBi)	Realized gain (dBi)	Total efficiency (%)
No bend (reference)	—	5.8	3.7	61
Along length ($r_{min,L}$=8.8 mm)	$3.4 * r_{min,L}$	5.2	2.1	48
	$1.7 * r_{min,L}$	3.9	-1	32
Along width ($r_{min,W}$ = 4.5 mm)	$6.8 * r_{min,W}$	5.2	3.2	62
	$3.4 * r_{min,W}$	4.6	1.9	52

antenna variants are depicted in Table 3.4. For smaller cylinder radii, or equivalently, a larger amount of bending, the electric fields of the antenna become more spatially distributed. We see this in the form of a reduction in antenna directivity in Table 3.4. At the same time, the realized gain and total efficiency of the bent antenna was lower than the unbent/original antenna. Considering the simulated reflection coefficients in Fig. 3.13 and the data in Table 3.4 together, we may infer that the di-patch is more tolerant to bending along the length than along the width. It needed an exorbitant amount of bending along the length, as shown in Fig. 3.13 (f), for the di-patch antenna to lose -10 dB reflection coefficient, while for bending along the width, this occurred much quicker. Certainly, there are a myriad of ways in which we could bend the di-patch, but these two basic types of bends show that in general the di-patch antenna is quite resilient to such stresses, and therefore is a suitable candidate for conformal antenna applications.

3.4 Simulation and measurement comparisons

3.4.1 Bare di-patch antenna

Fig. 3.14 (a) presents a snapshot from the antenna measurement in a typical anechoic chamber, along with the reference coordinate system. The antenna was pasted on a light-weight, but sturdy cardboard screwed to a plastic slab. The plastic slab was bolted to the rotating metallic positioner, covered with pyramidal absorbers to avoid unwanted reflection artefacts in the measured radiation pattern. Consider first the simulated and measured reflection coefficient of the di-patch antenna in Fi g. 3.14 (b). There is an excellent agreement between the simulated and measured curves, and in each case nearly 100 MHz impedance bandwidth was obtained. Fig. 3.14 (c) and (d) compare the normalized simulated and measured radiation patterns in the horizontal and vertical cuts. There is a very good agreement between the simulated and measured patterns. The 3...6 dB reduction in the measured horizontal cut from $\theta = 120^\circ ... 210^\circ$ is due to the metallic positioner shadowing the measurement path between the di-patch antenna and the source antenna. The simulated and measured peak directivity, realized gain, front-to-back ratio, and total efficiency are summarized for the bare di-patch in Table 3.5.

Chip balun insertion loss compensation: An important point to be considered while looking at Table 3.5 is that the $\approx$ 0.5 dB (typical value, as mentioned in the data sheet) additional insertion loss from the chip balun [79] soldered at the di-patch feeding point was not calibrated out of the measurements. So, for a fair comparison with the simulations, which simply used a discrete port for exciting the di-patch antenna, the measured realized gain and efficiency should be increased by a factor of 0.5 dB, which

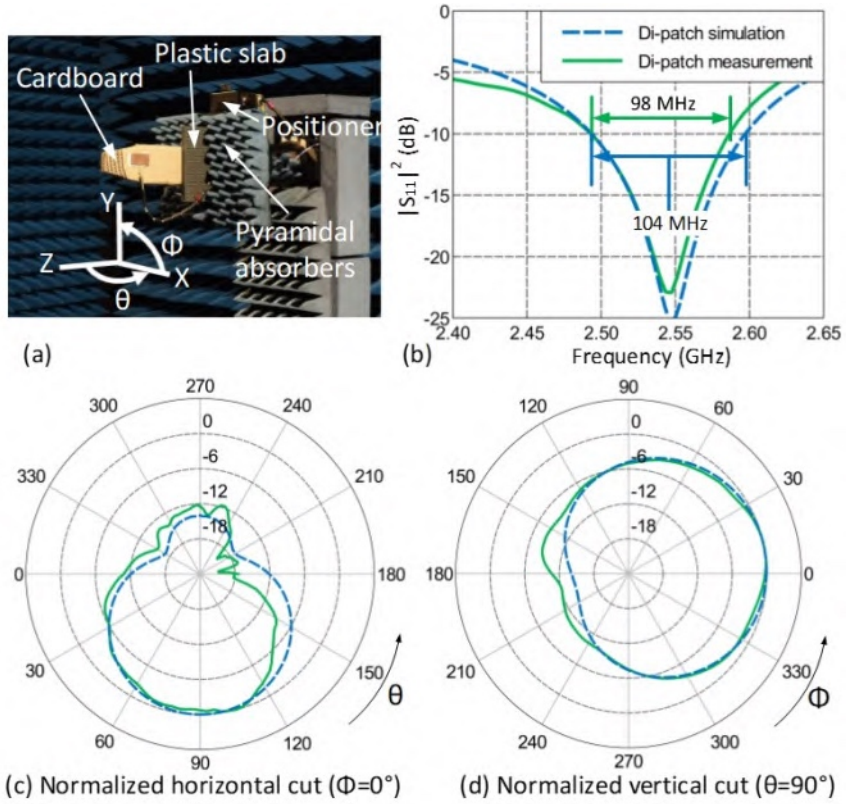

FIGURE 3.14: (a) Di-patch antenna measurement setup; the antenna lies in the Y-Z plane. (b) Simulated and measured reflection coefficients. (c), (d) Normalized horizontal and vertical cuts of the simulated and measured directivity patterns. [54] ©2019 IEEE

TABLE 3.5: Bare di-patch simulation vs. measurement [54] ©2019 IEEE. Values in bold compensate the 0.5 dB chip balun insertion loss.

	Simulation	Meaurement	Measurement uncertainty (dB)
Directivity (dBi)	5.8	6.3	±1
Realized gain (dBi)	3.7	2.8/**3.3**	
Front-to-back ratio (dB)	14	12	
Total efficiency (%)	61	44/**49.3**	

in turn leads to a measured realized gain of 3.3 dBi and efficiency of 49.3%, values that are now even closer to the simulations. This 0.5 dB compensation in realized gain and efficiency applies to all subsequent tables containing di-patch measured data.

3.4.2 Bare di-patch antenna compared to a bare patch antenna

The values presented in Table 3.5 for the bare di-patch antenna are what would be expected for a typical FR4 based patch antenna, with a larger ground plane, whereas the di-patch antenna achieves the same performance without a large ground plane, giving us an overall size advantage. This behaviour can be explained by observing the electric field distributions compared in Fig. 3.15 for a di-patch antenna and a patch antenna with a ground of the same size as the patch. Due to edge diffraction, the field strengths above and below the patch antenna are the same. On the other hand, the

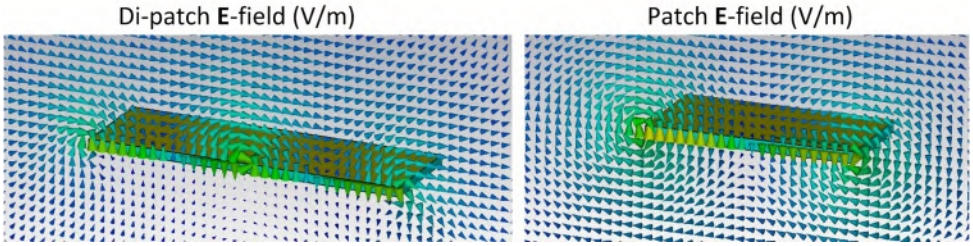

FIGURE 3.15: Comparison of the E-field distribution along the lengths of the di-patch antenna and a patch antenna with a ground plane same in size as the overlying patch. [54] ©2019 IEEE

TABLE 3.6: Di-patch vs. patch simulation results [54] ©2019 IEEE

Ground plane size	Substrate (1.6 mm thick)	Simulated directivity di-patch/patch (dBi)	Simulated FB ratio di-patch/patch (dB)
Infinite	Vacuum	10.5/9.9	infinite/infinite
As in Fig. 3.15	Vacuum	8.5/7	12/0
As in Fig. 3.15	FR4	5.8/3.5	14/0

field components at the centre of the di-patch are always above the ground, while those at the edges are also stronger in intensity above the di-patch antenna. Thus, the di-patch with a small ground is more directive than a patch antenna with a small ground, as also seen from the results in Table 3.6. This table also provides a general demonstration of how antenna directivity is influenced by the size of the ground plane and the choice of the substrate material. Smaller ground planes provide an opportunity for back-side radiation, and this reduces the directivity. Higher substrate permittivity implies a lower effective antenna aperture at the same frequency, which in turn also reduces the directivity.

The question now was how large a patch antenna ground plane needed to be, so as to obtain radiation characteristics comparable to the di-patch antenna, as this would help quantify the comparative size advantage offered by the di-patch antenna. Starting with a square patch, it was found through simulations that a ground plane at least 3 times larger in surface area compared to the square patch was necessary to achieve $\approx$ 6 dBi directivity and $\approx$ 12 dB FB ratio corresponding to the di-patch antenna. This made the di-patch antenna $\approx$ 40% smaller in surface area compared to the patch antenna, at the same frequency. Based upon these simulations, a patch antenna was manufactured, measured, and compared to the previously measured di-patch antenna. The permittivity and thickness of the substrate influence the antenna gain and bandwidth. To ensure a fair comparison, the same 1.5 mm thick FR-4 substrate from the same lot was used to make the patch antenna, as the di-patch antenna. The measurement results are presented in Fig. 3.16, and summarized in Table 3.7. The di-patch antenna offers twice the impedance bandwidth. The horizontal directivity cuts are comparable, while the differences in the vertical cuts are due to dipole like radiation from the di-patch. The differences in the measured directivity/gain are irrelevant. Furthermore, the differential feeding of the di-patch antenna offers the advantage of common mode noise rejection over the microstrip feed of a patch antenna.

TABLE 3.7: Bare di-patch vs. patch measurement results [54] ©2019 IEEE. Values in bold compensate the 0.5 dB chip balun insertion loss.

Antenna type	Substrate (1.6 mm)	Measured directivity (dBi)	Measured realized gain (dBi)	Measured FB ratio (dB)	Total efficieny (%)	Impedance bandwidth (MHz)
Di-patch	FR4	6.3	2.8/**3.3**	12	44/**49.3**	98
Patch		7.2	2.4	12	33	45

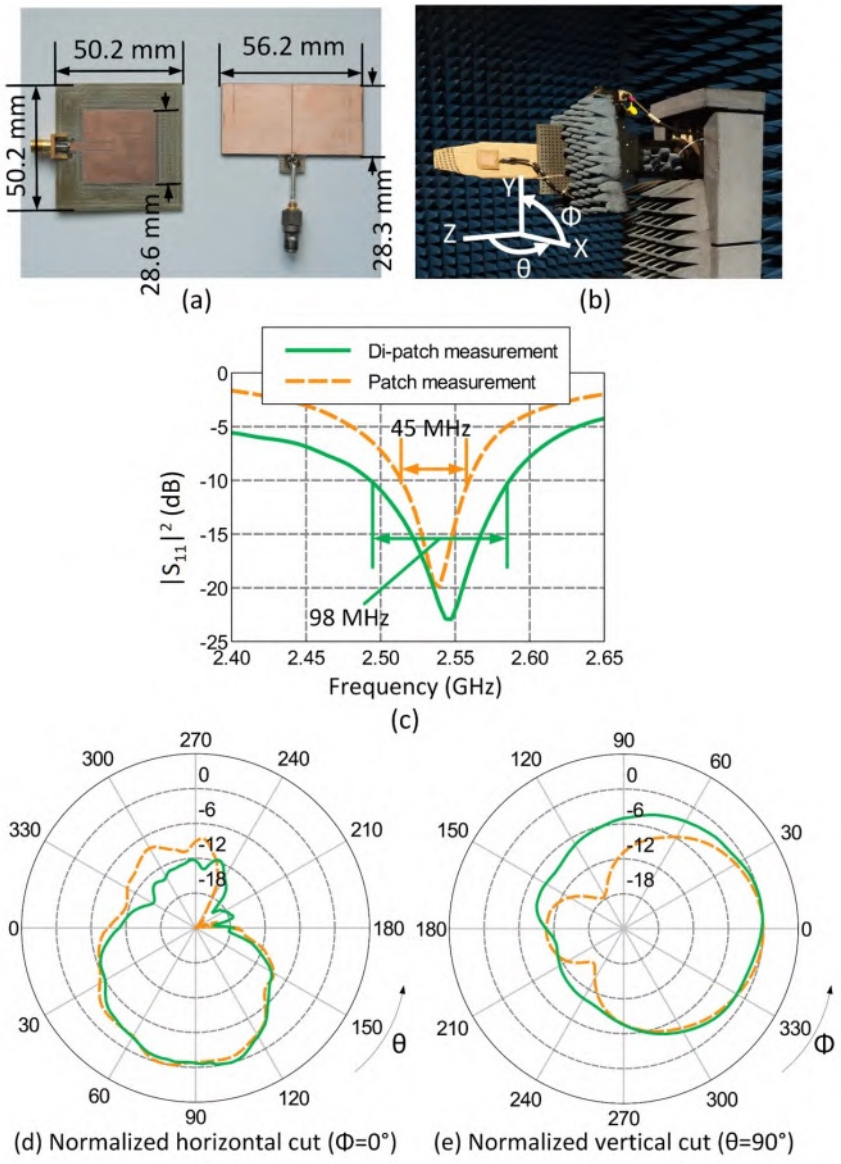

FIGURE 3.16: (a) Manufactured patch antenna/di-patch antenna dimensions. (b) Patch antenna measurement setup, and the reference coordinate system. (c) Measured reflection coefficients and impedance bandwidths. (d), (e) Normalized measured horizontal and vertical cuts of directivity of the patch and the di-patch antenna. [54] ©2019 IEEE

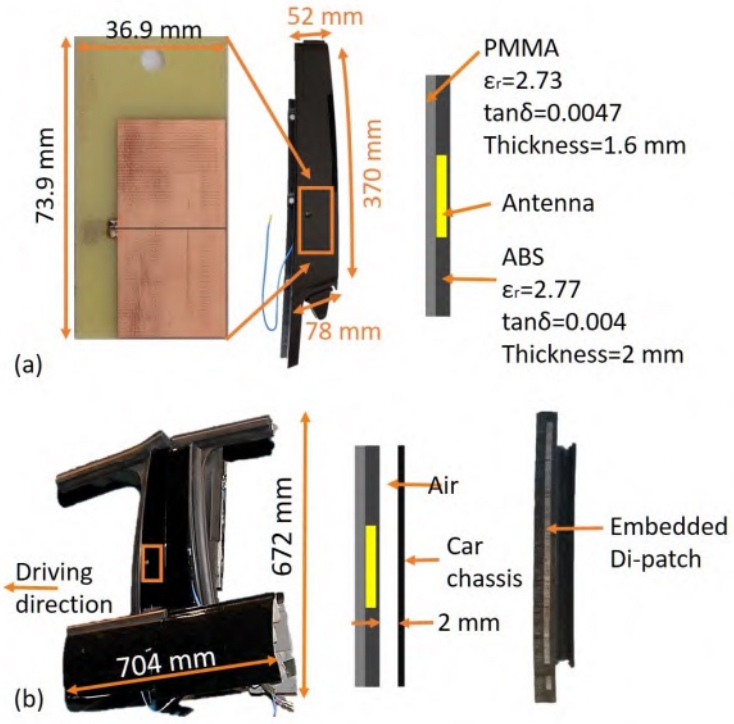

FIGURE 3.17: (a) Manufactured di-patch antenna prototype, approximate embedding location in the plastic cover, and the plastic cover material properties, (b) The door frame cut out, cross-section after mounting the plastic cover on the door frame, and a manufactured plastic cover cut along its length. [55] ©2019 IEEE

3.4.3 Simulations and measurements with partial door frame

This forms the second step in the simulation/measurement strategy outlined in the previous chapter. To perform measurements with the partial door frame, the antenna needed to be first embedded into the plastic cover. In order to embed the antenna in the front/driver side B-column plastic cover, an injection moulding process was followed at Wiegand [80]. In the first step, ABS (acrylonitrile butadiene styrene) at 230...240°C was injected within 3 seconds around the antenna held at a fixed location. This was followed by a cooling phase in which the temperature was brought down to 70° C within 40 seconds. In the second step, a glossy top layer of PMMA (Polymethylmethacrylat) was injected at 230...240°C within 3 seconds, followed by the same 40 seconds cooling phase to 70°C, with the temperature coming down to room temperature in another 5...10 minutes. Additionally, the antenna also experiences pressures of up to 140 MPa during the moulding process.

The approximate location of the embedded antenna in plastic cover is indicated by the orange box in Fig. 3.17 (a), along with the ABS and PMMA material properties that were also verified through split-ring resonator measurements. Following this, the plastic cover was mounted on to the door frame structure, as shown in Fig. 3.17 (b), along with a cross-section indicating the distance between the cover and the car metal chassis following the mounting. The impact on the antenna performance due to the thermal and pressure related stresses suffered by it during the embedding process will be addressed next, before moving on to the radiation pattern simulations and measurements.

As FR4 was used as the antenna substrate, with regard to the high temperature

during the moulding process, two temperature limits pertaining to the FR4 material need to be considered: T_g = 135°C, the glass transition temperature, and, T_d = 315°C, the thermal decomposition temperature [81]. If heated beyond T_d, FR4 begins to decompose and change chemically, but since the maximum temperature during the moulding is 240°C, the chemical properties of FR4 are not affected. However, the moulding process exceeds T_g for a short span of time. At a temperature higher than T_g but lower than T_d, the polymer chains of FR4 loosen up, imparting the substrate a rubber like consistency, and there is a 250 ppm/°C thermal expansion in the thickness of the substrate. But these physical changes in substrate reverse as the temperature falls below T_g. To make sure that the antenna is indeed not affected by the high moulding temperatures, a bare di-patch antenna was heated in an oven. The antenna experienced temperatures of 200°C for around 4 minutes, followed by 235°C for 1 minute, and was then allowed to cool down to the ambient temperature. In comparison, the antenna experiences temperatures above T_g for less than a minute during the actual moulding; longer and more stringent high-temperature conditions were deliberately chosen for this test.

On comparing the antenna dimensions and reflection coefficients before and after heating, no differences were found. Therefore, it is safe to say that the high moulding temperature has no impact on the electrical behaviour of the antenna. But what could not be simulated in our lab was the 140 MPa pressure experienced by the antenna alongside the high temperature during the moulding. To see if the high pressure had made a significant impact on the antenna geometry, a plastic cover sample containing the embedded antenna was cut along its length to expose the di-patch embedded in the ABS layer, as shown in the rightmost picture in Fig. 3.17 (b). No significant differences were found in the length or the thickness of the embedded antenna measured from the plastic cover cutout, showing that the antenna had survived the strenuous moulding process with the substrate suffering neither chemical nor physical changes.

The simulated model, the measurement setup, and the simulated and measured results are presented in Fig. 3.18. The measured resonance was not as sharp and deep as in the simulations. One major factor that could be responsible for it is the simplicity of the simulated door frame model in comparison with the actual door frame. But the simple model led us to the correct center-frequency in the measurements, as well as the simulated and measured normalized radiation patterns were in good agreement. While the horizontal cuts are smooth in the upper hemisphere, the vertical cuts present some ripples. This is due to the secondary radiation contributions from traveling waves that are excited especially strongly along the narrow slit between the front and the back door, i.e., in the plane of the vertical cut. This can be seen from the electric field distribution presented in F ig. 3.18 (e). The key simulated and measured values are summarized in Table 3.8. We see that the directivity measured for the door

TABLE 3.8: Partial door frame simulation and measurement results, bare di-patch measurement results [55] ©2019 IEEE. Values in bold compensate the 0.5 dB chip balun insertion loss.

	Directivity (dBi)	Realized gain (dBi)	Total efficiency (%)
Door frame simulation	7.6	5	55
Door frame measurement	8.2	3.5/**4**	34/**38**
Bare di-patch measurement	6.3	2.8/**3.3**	44/**49.3**

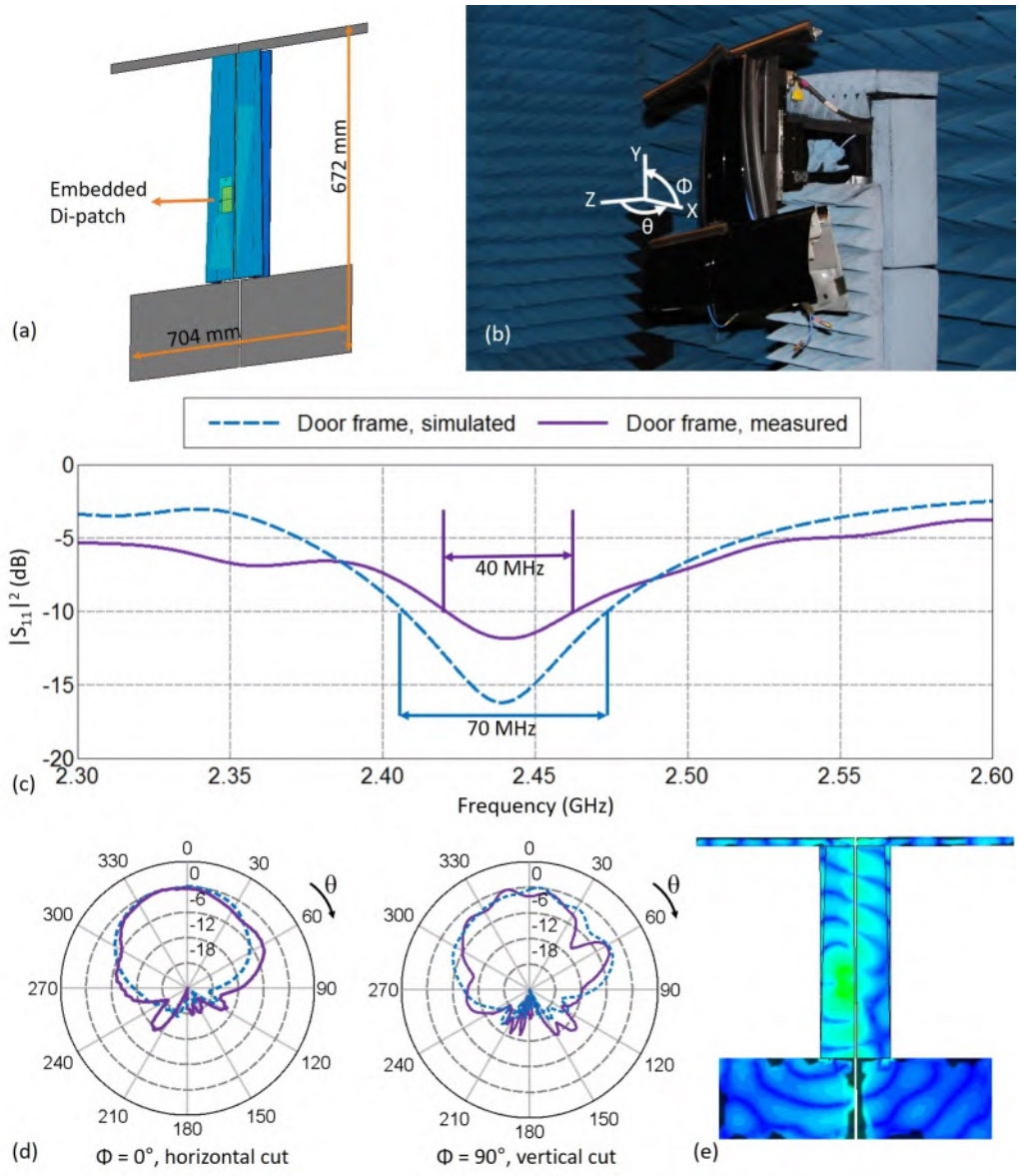

FIGURE 3.18: (a) Simulation model. (b) Measurement setup; door frame lies in the Y-X plane. (c) Simulated and measured reflection coefficients. (d) Normalized horizontal and vertical cuts of directivity. (e) Simulated electric field distribution on the door frame. [55] ©2019 IEEE

frame is approximately 2 dB higher than the bare di-patch directivity. While the bare di-patch in itself consists of a small ground, after plastic embedding and mounting on the door frame, the car metal chassis acts as an extended reflector behind the di-patch antenna, which directs more of the radiation to the upper hemisphere, leading to a larger directivity than for the bare di-patch.

Chip-balun insertion loss compensation: In Table 3.8, compensating for the 0.5 dB chip balun insertion loss, the di-patch door frame measured realized gain becomes 4 dBi, and the total efficiency increases to 38%. The corresponding values for the bare di-patch measurement, as pointed out earlier would be 3.3 dBi and 49.3%.

3.4.4 Simulations and measurements with car

As mentioned in the previous chapter, simulations with a complete car model would yield the most accurate results, but are not practically feasible due to limited computing resources and processing time, especially when the car is far electrically larger than the operational wavelength under consideration. Therefore, the simulation results presented in this section consider only a simplified model of the car chassis and are mainly intended to provide a qualitative idea of the installed antenna performance.

The car was first simulated with all its doors in the closed position, and thereafter with the driver-side front door opened to the maximum door opening angle of 65° as applicable to the considered car model, an Audi A1. As the front door contained the plastic cover with the embedded antenna, it was interesting to know the impact of opening that door on the installed antenna radiation pattern. These results are presented in Fig. 3.19, starting with the electric field amplitude distribution on the car body in both the cases. We see in Fig. 3.19 (a), that the fields are the strongest in intensity in the region in which the di-patch antenna was installed, and in general, stronger on the two doors that sandwich the antenna. As the car was electrically large, electric fields manifested on the chassis in the form of traveling waves, which radiate on encountering discontinuities like corners and edges in the model, and lead to the formation of ripples in the antenna radiation pattern. If we now consider the field distribution in Fig. 3.19 (b), it is noticeable that after opening the door, the field strength on the passenger side back door and on the rooftop decreased in intensity, but whether such changes in the field distribution were enough to considerably impact the antenna radiation pattern remained to be seen. We shift our attention to the normalized horizontal radiation patterns presented in Fig. 3.19 (b) and (c), wherein in we may observe that on rotating back the open door radiation pattern by 65° in (c), there was quite a good overlap to the closed door radiation pattern, except for some discrepancies in the ϕ= 180°...300° range. This is most likely due to the fact that opening the door allows the antenna to radiate a bit more freely on the open side; closing the door prevents this, as this radiation is reflected off of the passenger-side back door. The vertical cuts in Fig. 3.19 (d) had an almost perfect overlap, with some differences in their back lobes. With all this considered, it was not surprising to see that the measured cuts in Fig. 3.19 (g)...(i) presented a similar behavior. Therefore, we may conclude that opening the door containing the antenna has no significant impact on the shape of the radiation pattern; the radiation pattern simply rotates along with the door.

Radiation pattern shapes may be in agreement, but this does not necessarily imply that the directivity and gain values would also be the same. Let us take a look at Table 3.9, and in particular if we consider the row containing the measured values, we notice no significant differences between the closed door and open door values. We may conclude that opening the door neither significantly impacts the

TABLE 3.9: Simulated and measured values with the whole car. Values in bold compensate the 0.5 dB chip balun insertion loss.

	Closed door			Open door		
	Directivity (dBi)	Realized gain (dBi)	Total efficiency (%)	Directivity (dBi)	Realized gain (dBi)	Total efficiency (%)
Simulated	8.2	1.2	20	6.7	-0.5	20
Measured	9.4	1.3/**1.8**	15/**17.4**	9.5	0.8/**1.3**	14/**15**

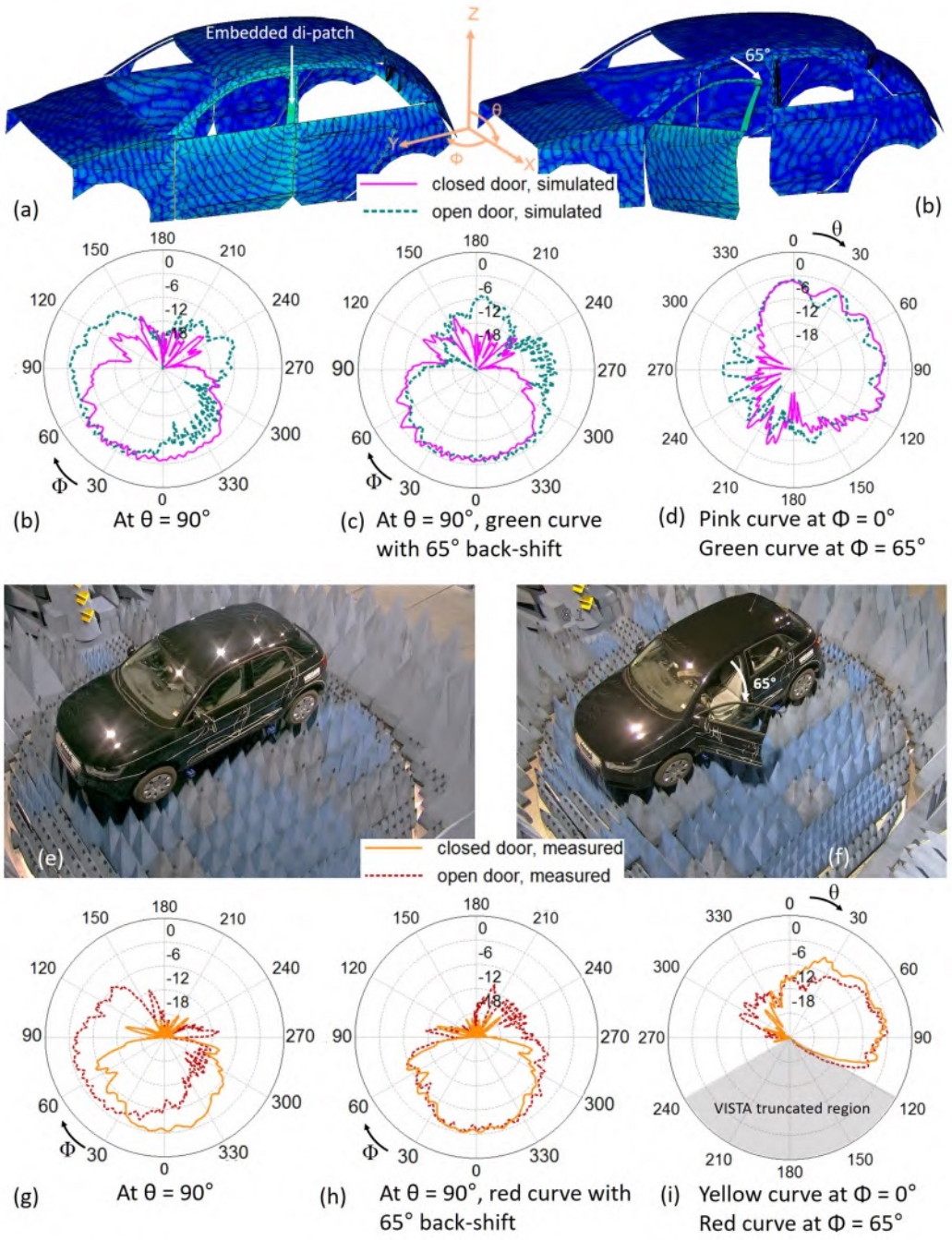

FIGURE 3.19: (a), (b) E-field amplitude distribution (V/m) with doors closed, and with the front door opened. (b), (c) Comparison of simulated normalized horizontal cuts of directivity. (d) Comparison of simulated normalized vertical cuts of directivity. (e), (f) Snapshots from anechoic chamber measurements. (g), (h) Comparison of measured normalized horizontal cuts of directivity. (i) Comparison of measured normalized vertical cuts of directivity.

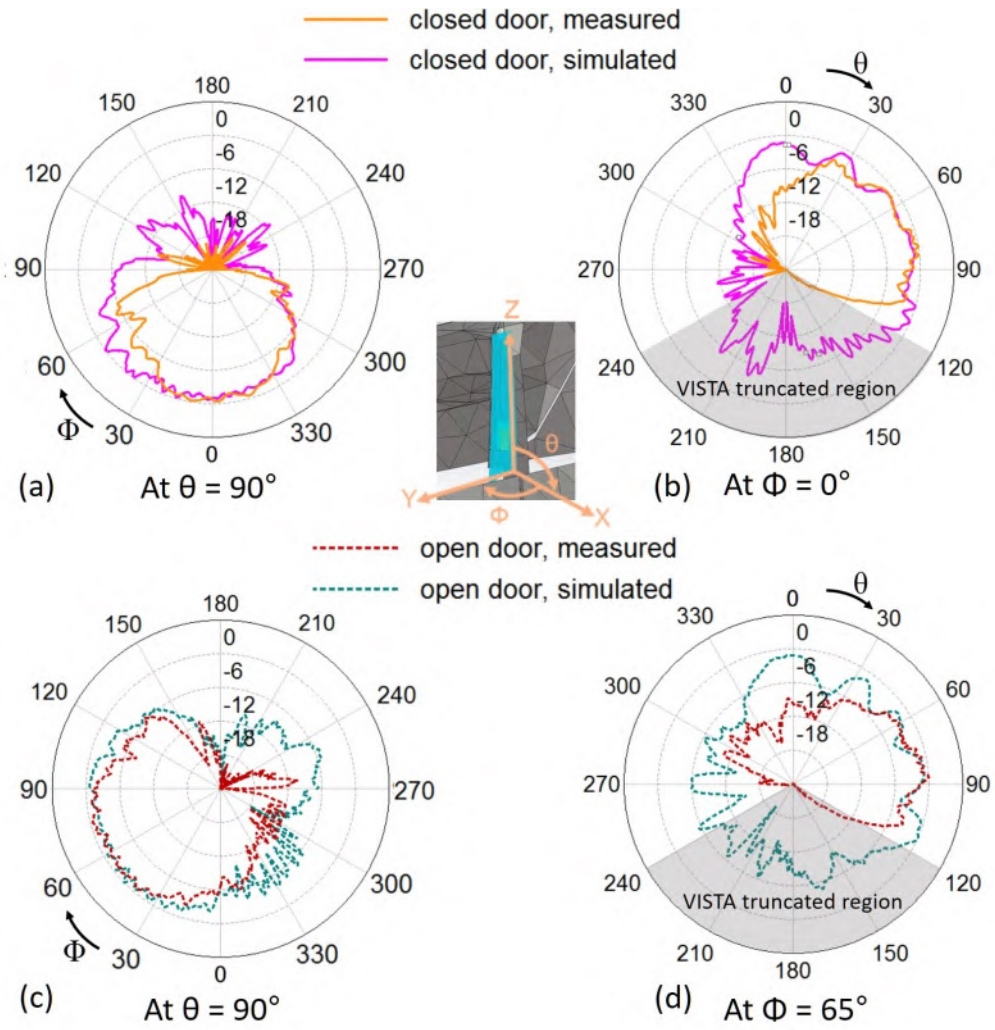

FIGURE 3.20: (a), (b) Comparison of measured and simulated normalized patterns of directivity with the front door closed. (c), (d) Comparison of measured and simulated normalized patterns of directivity with the front door opened.

shape, nor the peak values pertaining to the radiation patterns. The simulated values are also presented in the upper row of Table 3.9, and there we see larger discrepancies. As pointed out earlier, the various simulation model simplifications imply that the simulations provide qualitative, and not quantitative, ideas about the antenna performance, and therein the simulation was an accurate predictor of that the shape of the radiation pattern would not be influenced by opening the front door. For the sake of completeness, a comparison between the normalized simulated and measured radiation patterns is also presented in Fig. 3.20.

Chip-balun insertion loss compensation: In Table 3.9, compensating for the 0.5 dB chip balun insertion loss, the closed door measured realized gain becomes 1.8 dBi, and the total efficiency increases to 17.4%. The corresponding values for the open door measurement would be 1.3 dBi and 15%.

VISTA truncation compensation: This is relevant only for the radiation patterns measured in VISTA, as in this section. Due to the truncated measurement, a portion of the radiation in the lower hemisphere is not accounted for, as a result it is reasonable to expect that the antenna efficiency and the realized gain would further increase in

value if the truncated region were to be taken into account. An idea about how much of the pattern is truncated can be had by looking at the simulated and measured curves in Fig. 3.20. It is not straightforward to predict the increase in gain and antenna efficiency one may achieve by incorporating the truncated region, due to the simplified nature of the simulations, the inherent $\pm$ 1.4 dB measurement uncertainty of VISTA among other things. An elaborate discussion to this end is presented in [47], as also pointed out in the introductory chapter. This consideration naturally also applies to the VISTA radiation pattern measurements in the subsequent chapters.

3.5 Series-fed di-patch array

Microstrip patch antennas are ideally suited for conformal arrays due to their low-profile design, and such arrays find applications in satellite communication and navigation, WLAN, telemetry, mmWave radar sensors and so forth. The interesting question at this point was if a series-fed di-patch array could be realized, and whether it would offer any advantages over the series-fed patch array. In this regard, taking the bare patch antenna design of sub-section 3.4.2 (Fig. 3.16 (a)) as a starting point, a 1$\times$2 series-fed patch array was constructed as shown in Fig. 3.21 (a), to act as a reference for performance comparison. On the other hand was a 1$\times$2 series-fed di-patch array as shown in Fig. 3.21 (b). The substrate permittivity was, as before, 4, at which $\lambda_g = \lambda_0/2$. The inter-element distance between the array elements was of course $\approx \lambda_0/2$, but the length of the interconnecting microstrip line depends on the type of array desired. In this case, for a broad-fire array, the first and the second element need to be excited in phase. Going back to Fig. 3.21 (a), we know that the opposite ends P1 and P2 of any patch are in 180° phase opposition, therefore for an in-phase excitation, the line connecting the first patch to the second patch at P1 two needs to be $\lambda_g/2$ in length. On the other hand, if we consider Fig. 3.21 (b), at the opposite points P1' and P2' of a di-patch the phase is the same, therefore to ensure an in-phase excitation, the line connecting the first di-patch to the second di-patch at point P2' needs to be λ_g in length, and this is the reason that the line needed to be meandered in order to fit it in a space that was only $\lambda_g/2$ in length.

In terms of the total surface area, the di-patch array is $\approx$ 20% smaller than the patch array, and the normalized radiation patterns in Fig. 3.21 (c) and (d) are comparable in the upper hemisphere, with some differences towards the lower hemisphere. Although the patterns appear to have similar shapes at the same value of ϕ, it must be kept in mind that the patterns are orthogonal to each other; $\phi = 0$ corresponds to the E-plane for the patch array, and H-plane for the di-patch array. The key simulated values are collected in Table 3.10. The directivity of the patch array and the di-patch array is the same, but the di-patch array realized gain was 1.3 dB higher, as it radiates more efficiently. In terms of the impedance bandwidth, the di-patch array once again offers nearly twice the bandwidth over the patch array. Considering all this, the di-patch antenna appears to a suitable and promising candidate for array applications, and should be further investigated.

TABLE 3.10: Key simulated values for the patch and the di-patch array.

Array type	Directivity (dBi)	Realized gain (dBi)	Total efficiency (%)	Impedance bandwidth (MHz)
Patch array	8	2.6	29	61
Di-patch array	8.3	3.9	37	113

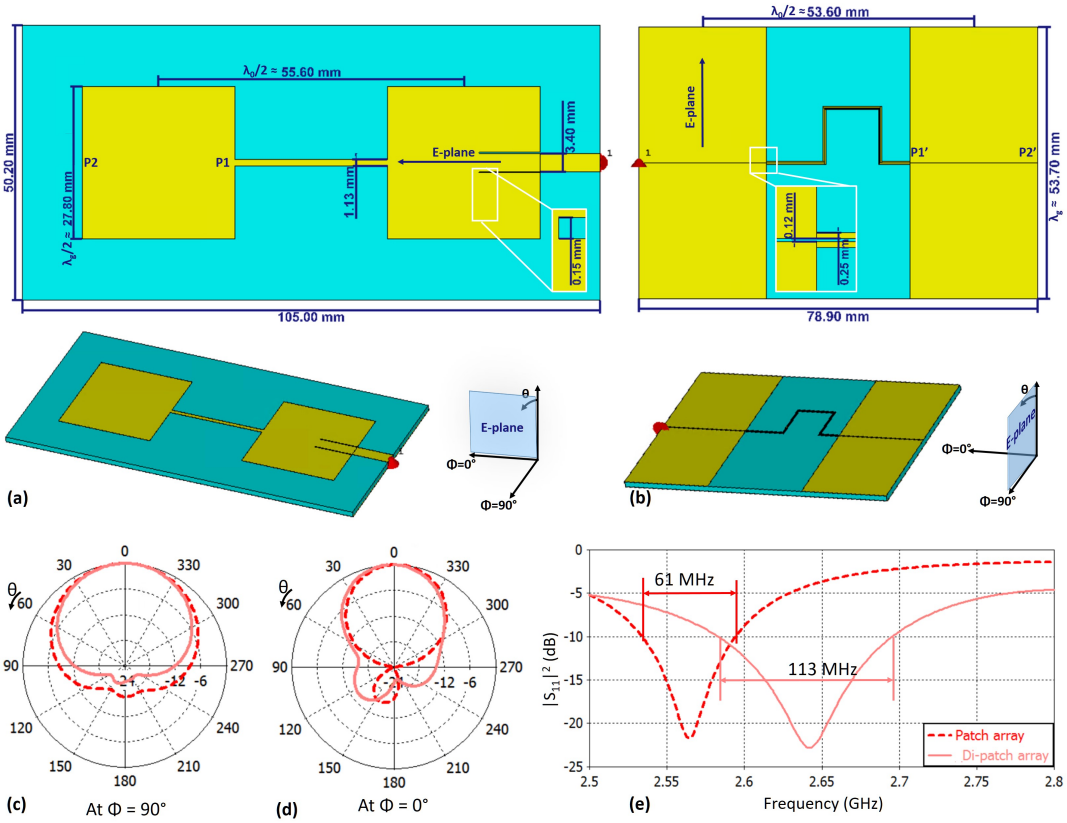

FIGURE 3.21: (a)Patch array. (b) Di-patch array. (c), (d) Normalized cuts of the radiation patterns in two different planes. (e) Comparison of the patch array and di-patch array impedance bandwidths.

Chapter 4

Co-planar stacked microstrip line coupled multi-band patch antenna

4.1 General design principles and novel aspects

In the last chapter we saw that a full-wavelength dipole above a metallic ground offered twice the impedance bandwidth over a typical patch antenna, thus improving upon the main limitation associated with a patch antenna, with no compromise of the achievable realized gain, and with the advantage of a significantly smaller size. However, if we want to achieve an even larger bandwidth with a single antenna, then we need to look into other possible ideas and antenna design configurations. This is relevant because vehicles use a multitude of wireless communication services operating in different frequency bands.

In this regard, if we take a closer look into the multi-band patch antenna design approaches followed in the literature up till now, two of the simplest techniques are: (a) co-planar or vertical stacking of patches [82] - [88], or (b) off-center fed rectangular patches [89, 90]. There is a subtle difference between the approaches (a) and (b). While (a) leads to a widening of the bandwidth around the centre frequency, (b) leads to the formation of two distinct resonance frequencies corresponding to the orthogonal TM_{10} and TM_{01} dominant modes. The first resonance lies along the patch length, and the second along its width, wherein the patch aspect ratio may be adjusted to move the two bands closer or further apart.

For a quantitative description of what these approaches offer against a typical patch antenna, consider Fig. 4.1. The reflection coefficient of single centre-fed patch antenna is plotted in green, and acts as the reference curve. If we look at case (a), the black curve, we see that it offers ≈ 2 times the bandwidth compared to the green reference curve, but the bandwidth enhancement is limited to the vicinity of 1.8 GHz. Parasitic patches may be stacked horizontally along the length, as done in this example, or along the width of the primary patch, or along its length and width simultaneously - but fundamentally only the bandwidth around the centre frequency is improved. On the other hand, for case (b) represented by the green curve, the first resonance overlaps with the reference resonance, and there is a second resonance close to 2.6 GHz, but the bandwidth remains limited in each offered band.

An extensive research of the current literature showed that the combination of these two approaches was not considered before. A successful combination would naturally combine the benefits of the two approaches, i.e., a larger bandwidth due to co-planar stacking as well as the freedom to move the frequency bands by varying the aspect ratio of the off-centre fed patch. In this chapter, instead of using an off-centre probe feed, the patch was excited at its corner with a microstrip feed. It was observed that by horizontally stacking a parasitic patch adjacent to this corner-fed rectangular patch, not only did we obtain the dual-band behaviour expected for a

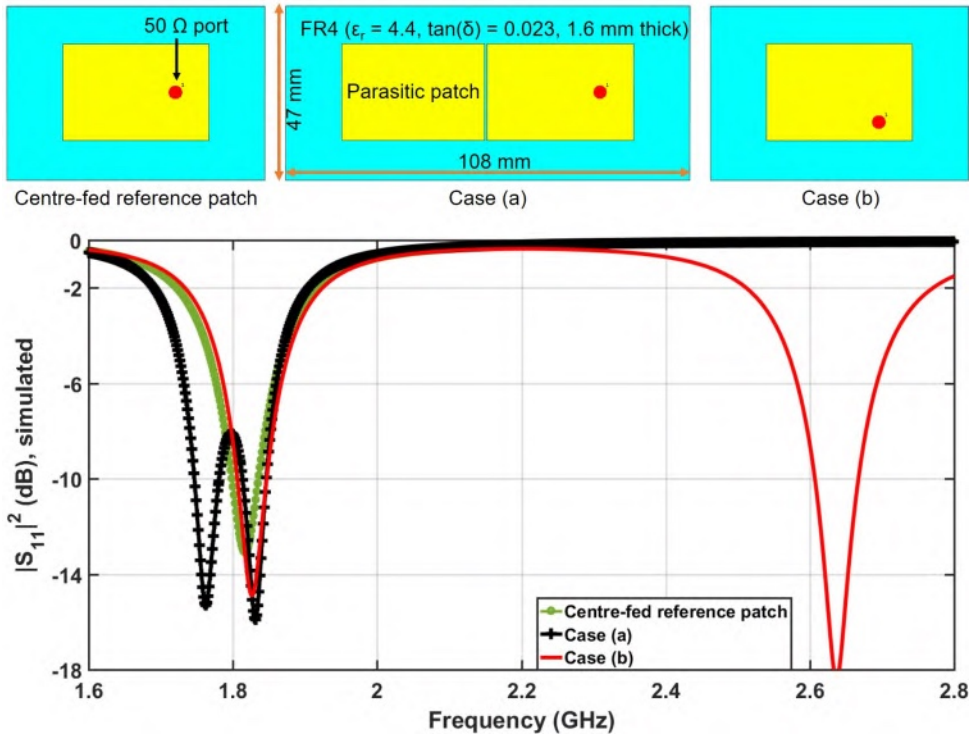

FIGURE 4.1: Reflection coefficient of a centre-fed reference patch in comparison with the reflection coefficient with a co-planar parasitic patch in case (a), and off-centre feeding in case (b). [94] ©2019 IEEE

corner-fed patch, but also an increased bandwidth in each of the two bands due to the parasitically coupled patch. Furthermore, this approach could be extended to cover additional frequency bands to obtain a penta-band antenna design, wherein, as expected, one was free to scale the length-to-width ratios of the patches to tune/shift the multi-band response to cover virtually any desired set of frequencies.

These findings enabled the design of a multi-band antenna that covered the LTE-1800 uplink (UL) (1.71...1.78 GHz), LTE-1800 downlink (DL) (1.805...1.875 GHz), UMTS UL (1.92...1.998 GHz), UMTS DL (2.11...2.17 GHz), and LTE-2600 (2.5...2.69 GHz) bands, as first reported in the author's publication [94]. The structure of the antenna followed a dual-layer design - a top layer containing the patches, and a bottom ground layer, with the substrate in between. Typical 1.6 mm thick FR-4 (ϵ_r = 4.4, $tan\delta$ = 0.023) was used as the antenna substrate. The overall thickness of the antenna, including the thickness of the copper layers, was $\approx$ 1.7 mm. The simplicity of the antenna design makes it easy to manufacture, and its low-profile lends well to mounting in many locations such as car rooftop antenna cavities [91, 92], or external plastic panelling.

4.2 Penta-band patch antenna design

4.2.1 Design overview and sensitivity analysis

The multi-band principle may be understood by considering the four antenna configurations and their corresponding simulated reflection coefficients sketched in Fig. 4.2 (a). The corner-fed rectangular patch of case 1 exhibits dual-band behaviour corresponding to the chosen dimensions L1 and W1; L1 corresponded to a resonance

in the LTE-1800 DL band, while W1 to a resonance in the LTE-2600 band. But the impedance bandwidth obtained was neither enough to cover the entire LTE-1800 bandwidth, nor the LTE-2600 bandwidth, the bandwidths being indicated by corresponding grey shaded areas in the power-related $|S_{11}|^2$ diagram. It was observed that by horizontally stacking a parasitic patch of slightly smaller dimensions next to patch 1 as in case 2, the bandwidth increased not only for the LTE-1800 DL resonance along L1, but also for the LTE-2600 resonance along W1, enabling the complete coverage of the LTE-1800 and LTE-2600 bands with $|S_{11}|^2 < -6$ dB. If we contrast case 2 in Fig. 4.2 to case (a) in Fig. 4.1, we see that for the same overall physical size we obtain two additional resonances centred around 2.6 GHz just by shifting the feed to a corner of patch 1. With centre feeding as in case (a), another antenna with two patches would be needed to obtain these resonances. This gives a clear idea of the size advantage gained by combining the principles of horizontal stacking and corner feeding of patch antennas.

Furthermore, extending the length of the microstrip feed and adding a third rectangular patch as in case 3, with accordingly chosen L2 and W2, covered the UMTS UL and DL bands with $|S_{11}|^2 < -6$ dB as well. With yet another parasitic patch as in case 4, the reflection coefficient for the WLAN, LTE-2300 etc. bands lying in between the other frequency bands could additionally be matched at a level below -10 dB. The result was an antenna wherein multiple closely located frequency bands bunched together to provide a wideband response that allowed us to cover the 1.7...2.69 GHz frequency range with $|S_{11}|^2 \leq -6$ dB. However, in addition to sufficient impedance bandwidth, efficient radiation is also needed for an antenna to be usable. As presented in the upcoming sections, the antenna design offered sufficient radiation efficiency.

At this point, we may ask the question that if vertical stacking of parasitic patches is also possible, why choose co-planar stacking. For example, if the two parasitic patches were to be vertically stacked under the corresponding primary patches in case 4, the overall antenna size would be smaller. While that may be true, we would at the same time increase the manufacturing complexity and cost, as the antenna would become multi-layered. There was enough space available in the plastic cover for a larger antenna, and as the main goal was to demonstrate the feasibility of the plastic cover as an antenna mounting location, the cheaper, and less complex co-planar stacking approach was the more sensible option. Especially, samples of co-planar stacked patch antennas could be quickly produced with the in-house PCB printer, as opposed to the inherent multi-day delay associated with having complex antennas manufactured elsewhere.

While the four-patch variant in case 4 covers the widest bandwidth, the triple-patch variant in case 3 was analysed in greater detail, as it already covered the frequency bands of interest. The simulated electric field distributions for case 3 are presented in Fig. 4.2 (b) for five different frequencies. Although all three patches contribute to the radiation at each of the depicted frequencies, their contributions are not equal. Considered first are the frequencies resonant in the TM_{10} mode along the lengths L1, L1-ΔL1, L2 of the three patches, i.e., 1.75 GHz, 1.85 GHz, and 1.95 GHz. At 1.75 GHz, patch 1 and 2 are the primary contributors, with almost no contribution from patch 3 as it corresponds to the relatively further apart UMTS-UL/DL frequencies. The situation is a bit different at the 1.85 GHz and 1.95 GHz frequencies corresponding to the LTE-1800 DL and UMTS UL band centres. While patch 1 and patch 2 are the main contributors at 1.85 GHz, there is a non-negligible contribution from patch 3 due to the proximity between the LTE-1800 DL and UMTS UL bands. Likewise, patch 3 is the main contributor at 1.95 GHz, but there are significant contributions from patch 1 and 2 as well for the same reason. Next

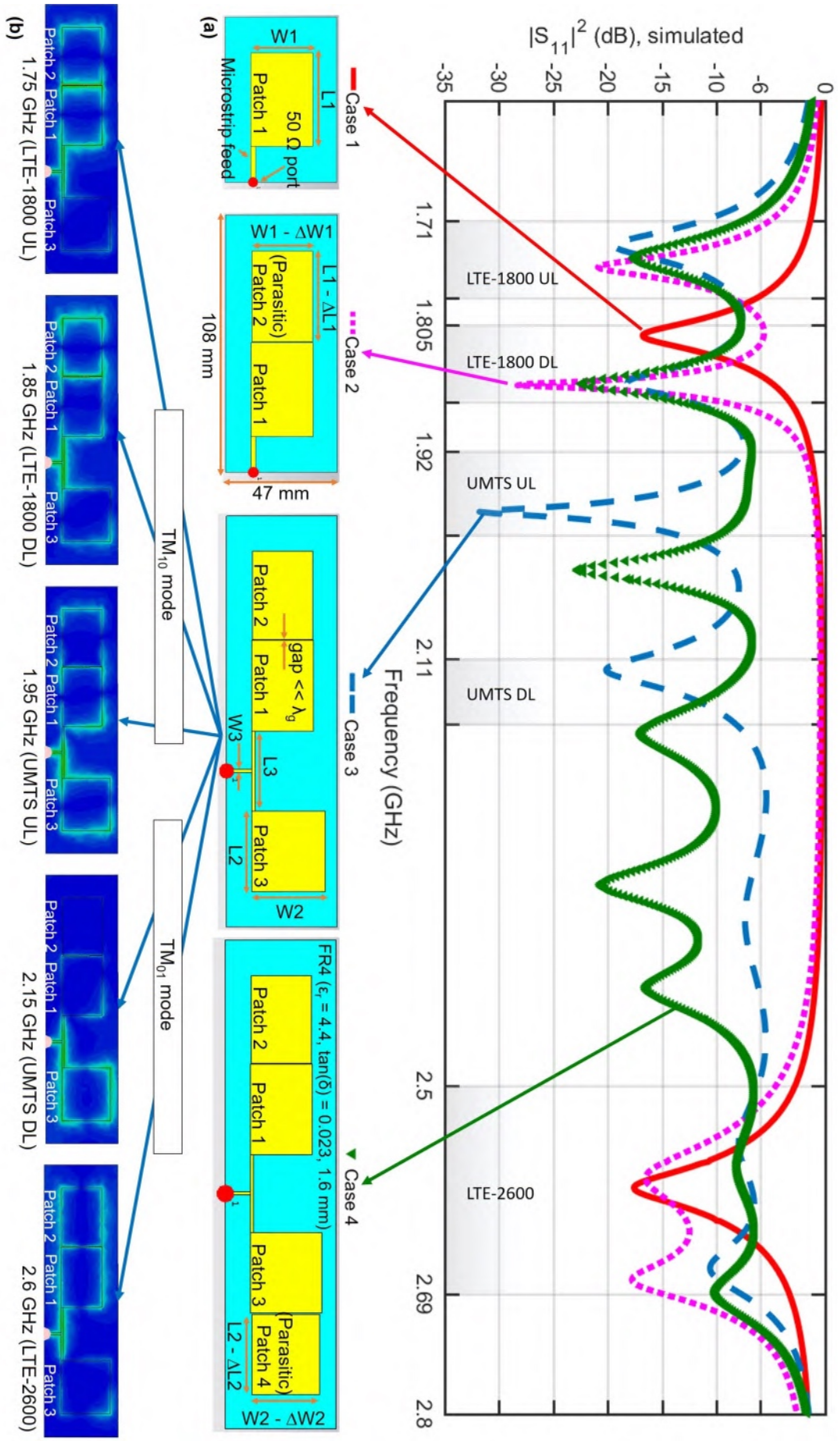

FIGURE 4.2: (a) Simulated reflection coefficients for the antenna evolution from case 1 to case 4. The grey shaded regions indicate the frequency bands of interest. (b) Electric field (V/m) amplitude distributions for case 3 near the centre frequencies of the frequency bands of interest. [94] ©2019 IEEE

considered are the frequencies resonant in the TM_{01} mode along the widths W1, W1-ΔW1, W2 of the three patches, i.e., 2.15 GHz and 2.6 GHz. Patch 3 is the primary resonator at 2.15 GHz, while patch 1 and 2 are the primary resonators at 2.6 GHz. In addition to this, and in general, there are radiation contributions from the microstrip line connecting patch 1 and patch 3 at all considered frequencies.

The dimensions of the simulated triple-patch antenna are provided in Fig. 4.3 (a). Considering that λ_g = 83 mm at 1.71 GHz, the lowest frequency of operation, and λ_g = 53 mm at 2.69 GHz, the highest frequency of operation, the overall physical size of the antenna 175 mm x 47 mm corresponds to an electrical size of 2.1 x 0.6 at 1.71 GHz, and 3.3 x 0.9 at 2.69 GHz. Let us now consider the influence of increasing the values of a few of the indicated parameters by 5%, on the $|S_{11}|^2$ of the triple-patch antenna. Of course, in each case only the considered parameter was varied, all others were held constant. We know that the dimensions L1 and W1 of patch 1 correspond to the LTE-1800 and LTE-2600 bands, respectively. If we look at Fig. 4.3 (b) and (c), we can see that a 5% increase in L1 and W1 correspondingly causes a left shift of the LTE-1800 and LTE-2600 bands, with no significant impact on the UMTS bands. On the other hand, the dimensions L2 and W2 of patch 3 control the UMTS UL and DL bands, and from Fig. 4.3 (d) and (e), it is clear that a 5% variation in L2 and W2 only impacts the UMTS bands, while the LTE bands are relatively unaffected.

To obtain the desired multi-band response from the antenna, a careful choice of the length L3 of the microstrip line was necessary, so that patch 1 and 3 may resonate independently without strongly interfering with each other. For obtaining the optimal length L3, λ_g = 83 mm corresponding to 1.71 GHz, the lowest frequency of operation in the multi-band response, was used as the reference. With L3 $<<$ λ_g, the multi-band behaviour was extremely deteriorated due to the intense interference between the patches, as shown in Fig. 4.3 (f). On increasing L3 gradually, L3 = 34 mm ($\approx \lambda_g/2.4$) was found to be a suitable value for obtaining the desired multi-band response. To provide an idea about the sensitivity of the multi-band response to variations in L3, the case for a 5% increase in L3 is also presented in Fig. 4.3 (f), wherein a slight deterioration in the LTE-2600 band reflection coefficient is visible. But this was tolerable, as the reflection coefficient remained below -6 dB. As opposed to this, varying the width, W3, of the microstrip line had almost no impact on the reflection coefficient, as shown in Fig. 4.3 (g). So, for the same amount of variation, the frequency response of the antenna was more sensitive to the microstrip line length than its width.

The next parameter analysed was the ϵ_r of the substrate, and Fig. 4.3 (h) shows that a 5% increase in the relative permittivity shifted the entire $|S_{11}|^2$ curve leftwards by 30...50 MHz. Lastly, the impact of the gap width on the frequency response was considered. As the gap width was the smallest dimension in the entire antenna design, the impact of printing uncertainties on it would be the largest. Therefore, in addition to the 5% increase, as done with the other parameters, a 23% increase in the gap width was also simulated. It is interesting to note from Fig. 4.3 (i), that even such a large increase in the gap width did not significantly impact the frequency response of the antenna.

The motivation to consider this large variation in the gap width was the same as in the last chapter. It was known from previous experience that the printed antenna sample would have a $\pm$0.07 mm uncertainty in its dimensions, so it was sensible to see if a 0.07 mm change in the gap width had a substantial impact on the antenna reflection coefficient. On the other hand, as all other dimensions of the antenna were much larger than the gap width, performing sensitivity analysis with a 5% variation in these dimensions was more than adequate. With this information at

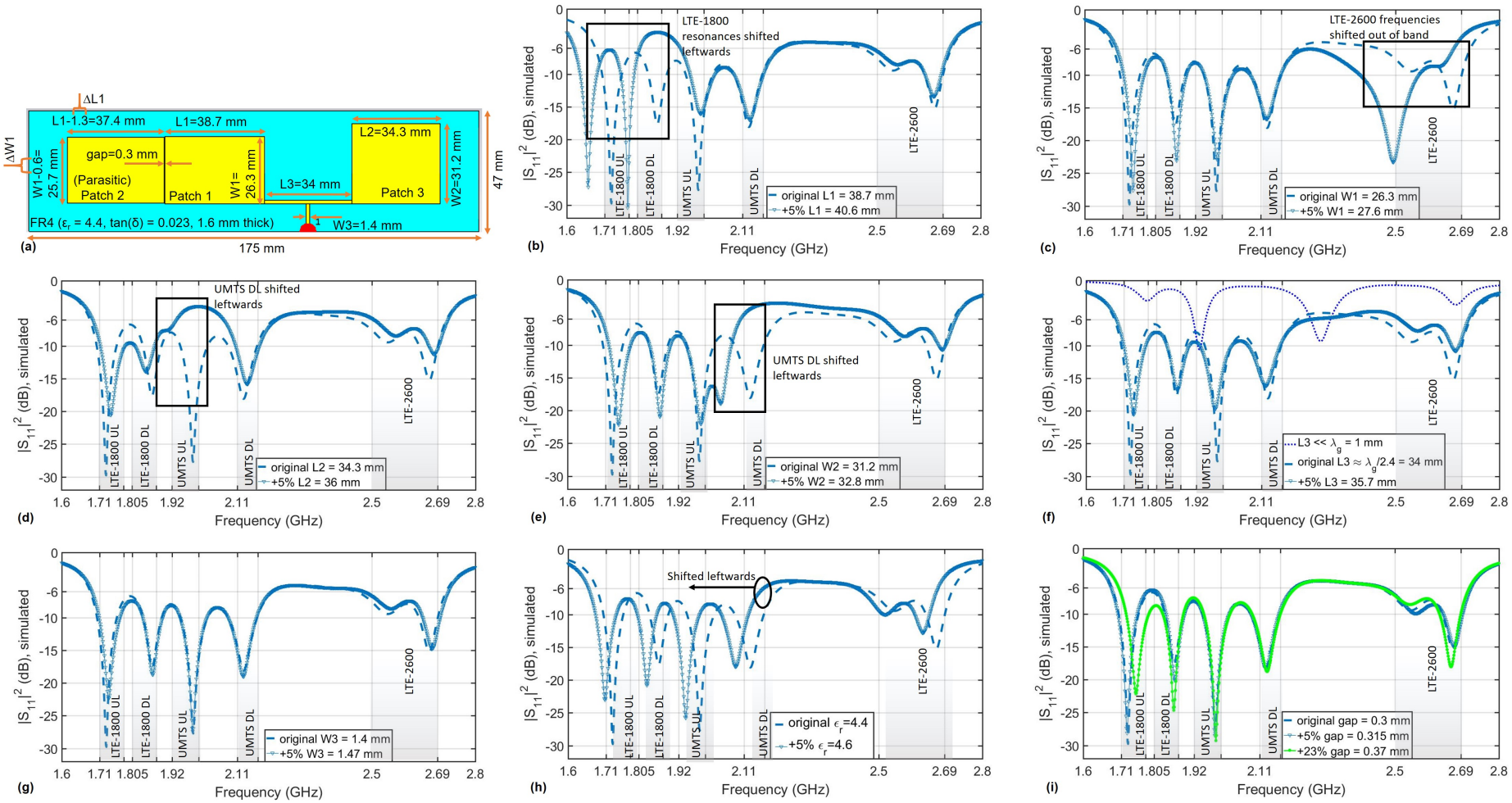

FIGURE 4.3: (a) Triple-patch antenna dimensions. (b), (c) Reflection coefficients for 5% increase in L1 and W1. (d), (e) Reflection coefficients for 5% increase in L2 and W2. (f), (g) Reflection coefficients for 5% increase in L3 and W3. (h) Reflection coefficient for 5% increase in ϵ_r. (i) Reflection coefficient for 5% and 23% increase in the gap width.

hand, it was almost certain that if the measured reflection coefficient of the printed antenna prototype were to differ from the simulated reflection coefficient, the most likely reason for this would be a deviation in the actual relative permittivity of the substrate from the value specified in the datasheet.

4.2.2 Impedance transformations in the design

Case 1 and case 3 of Fig. 4.2 (a) will be used to explain the various impedance transformations considered for the antenna design, and are presented again in Fig. 4.4 for the sake of convenience. Two general points need to be taken in consideration. First, since this is a multi-band antenna design, exact quarter-wavelength transformations will not apply; a quarter-wavelength at 1.8 GHz is electrically longer than the corresponding value at 2.6 GHz. The usage of the term quarter-wavelength implies the guided quarter-wavelength in this case, as the substrate is FR-4. Although multi-section wideband quarter-wave transformers exist in literature, the amount of additional space needed on the PCB for their implementation would exceed the space available for our automotive application. Secondly, the antenna is fed at a corner along the patch edge. Along the edge of a patch, the input impedance is not 50 Ω, but typically lies between 100 Ω...200 Ω depending upon the aspect ratio (length-to-width ratio) of the patch [63, 93], a direct consequence of how the electric field distributes in the substrate between the patch and the ground.

With this in mind, consider the antenna in case 1 in Fig. 4.4. As shown earlier, case 1 was resonant at 1.8 GHz and 2.6 GHz. It was found through simulations that the appropriate input impedance at the indicated corner of patch 1 was approximately 120 Ω. In other words, a 120 Ω source would be needed to excite the resonances at 1.8 GHz and 2.6 GHz, if patch 1 were to be fed directly at the indicated corner. But as 50 Ω sources are used to feed antennas, a transformation from 50 Ω to 120 Ω was necessary. From the standard quarter-wave transformation formula it was ascertained that a 75 Ω characteristic impedance microstrip line would provide the desired transformation. For Z_o = 75 Ω, the microstrip line needed to be 1.4 mm in width, in accordance with the substrate parameters. A quarter-wavelength $\lambda_g/4$ measures at 1.8 GHz $\approx$ 19.8 mm, while at 2.6 GHz $\approx$ 13.7 mm, so a line length between 13.7 mm and 19.8 mm was needed; much lower than 13.7 mm would be especially worse for 1.8 GHz, while much larger than 19.8 mm would be critical for 2.6 GHz in the first degree. It was seen that a line length of 15 mm was already good enough to excite both resonances, as clear from the corresponding reflection coefficient in Fig. 4.2 (a).

Consider now case 3 in Fig. 4.4. Patch 3 is responsible for the 1900 MHz UMTS UL band and the 2100 MHz UMTS DL band resonances. Following the same approach as with patch 1, on considering patch 3 alone, it was found that the input impedance at

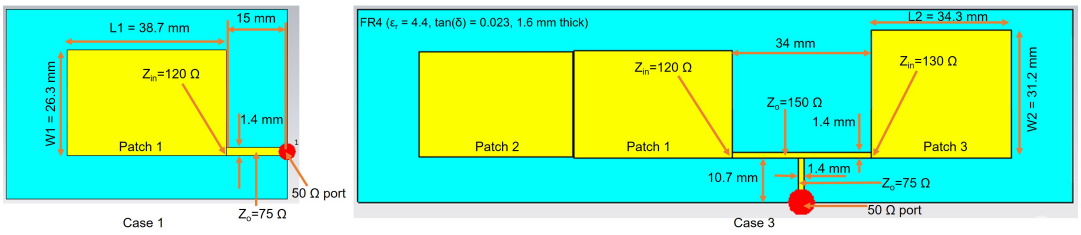

FIGURE 4.4: The different impedances and the corresponding transformations considered in the antenna design. [94] ©2019 IEEE

its indicated corner was approximately 130 Ω to excite the considered resonances. As shown in case 3, once again a 1.4 mm wide 75 Ω characteristic impedance microstrip line was constructed, and branched out towards patch 1 and patch 3 without changing its width. As a result, the microstrip line connecting the patches 1 and 3 acquired a characteristic impedance of 150 Ω. The reflection coefficient from 150 Ω to either 120 Ω or 130 Ω is already less than -19 dB (theoretical). So what was more important was to determine a suitable separation between patch 1 and patch 3 so as to provide sufficient decoupling between their corresponding resonances. As shown earlier, 34 mm was a good choice for this separation.

Finally, case 3 was with a 50 Ω source. The multi-band argument against a quarter-wave transformation from 50 Ω to the 75 Ω microstrip line applies once more, and it was also not absolutely necessary, given that the reflection from 50 Ω to 75 Ω is low enough at -14 dB (theoretical). However, although the best reflection coefficient at the port is theoretically -14 dB, the reflection coefficient curve for case 3 (and case 4) in Fig. 4.2 (a) shows values below -14 dB as well. The major reasons that lead to a better than expected reflection coefficient are the conductive losses associated with the copper patches, and the dielectric losses associated with the FR-4 substrate.

4.3 Simulation and measurement comparison

4.3.1 Bare triple-patch antenna measurements

In relation to the discussion in the last section, it was found that the entire reflection coefficient curve of the first manufactured antenna prototype, test sample 1, was shifted forwards by approx. 70...100 MHz, as shown in Fig. 4.5 (a). The situation was similar to Fig. 4.3 (h), except for the difference in the direction of the shift. This meant that our initial speculation was true, and the actual substrate permittivity was slightly lower than the value of 4.4 specified in the datasheet. So after re-designing the antenna considering a slightly smaller value of permittivity, results comparable to the simulations were obtained. The measured reflection coefficient of the optimized test sample 2 is shown in Fig. 4.5 (b).

For measuring the radiation patterns over the frequency range of interest, the approach followed was the same as in the case of the bare di-patch antenna measurement in the last chapter, so it is not repeated here. The measurement uncertainty was the usual $\pm$ 1 dB. Of the total 468 MHz bandwidth required by the various considered mobile communication bands, approx. 261 MHz could be covered with $|S_{11}|^2 <$ -10 dB, and the remaining with $|S_{11}|^2 \leq$ -6 dB in the measurement.

As in the last chapter, the antenna partial realized gains, G_v, in the vertical polarization, and, G_h, in the horizontal polarization were measured. Figures 4.6 (b)...(f) compare the normalized simulated and measured horizontal and vertical cuts of the combined realized gain, $G = G_v + G_h$, near the centre frequencies of each considered band. The qualitative agreement at 1.75 GHz, 2.15 GHz, and 2.6 GHz was quite good. The major differences between the simulations and measurements at these frequencies were in the horizontal cuts in the range $\theta = 120^\circ...220^\circ$ indicated by the grey shaded areas. The measured gain in this angular range was lower than the simulated gain at these frequencies due to the positioner shadowing the measurement path between the triple-patch antenna and the source antenna. The influence of the positioner was visible at 1.85 GHz and 1.95 GHz as well, however there were also other differences between the simulated and measured patterns at these frequencies. At 1.85 GHz, the back-side radiation of the measured vertical radiation pattern was stronger in intensity, for example by a factor of $\approx$ 12 dB at $\phi \approx 230^\circ$, as compared to

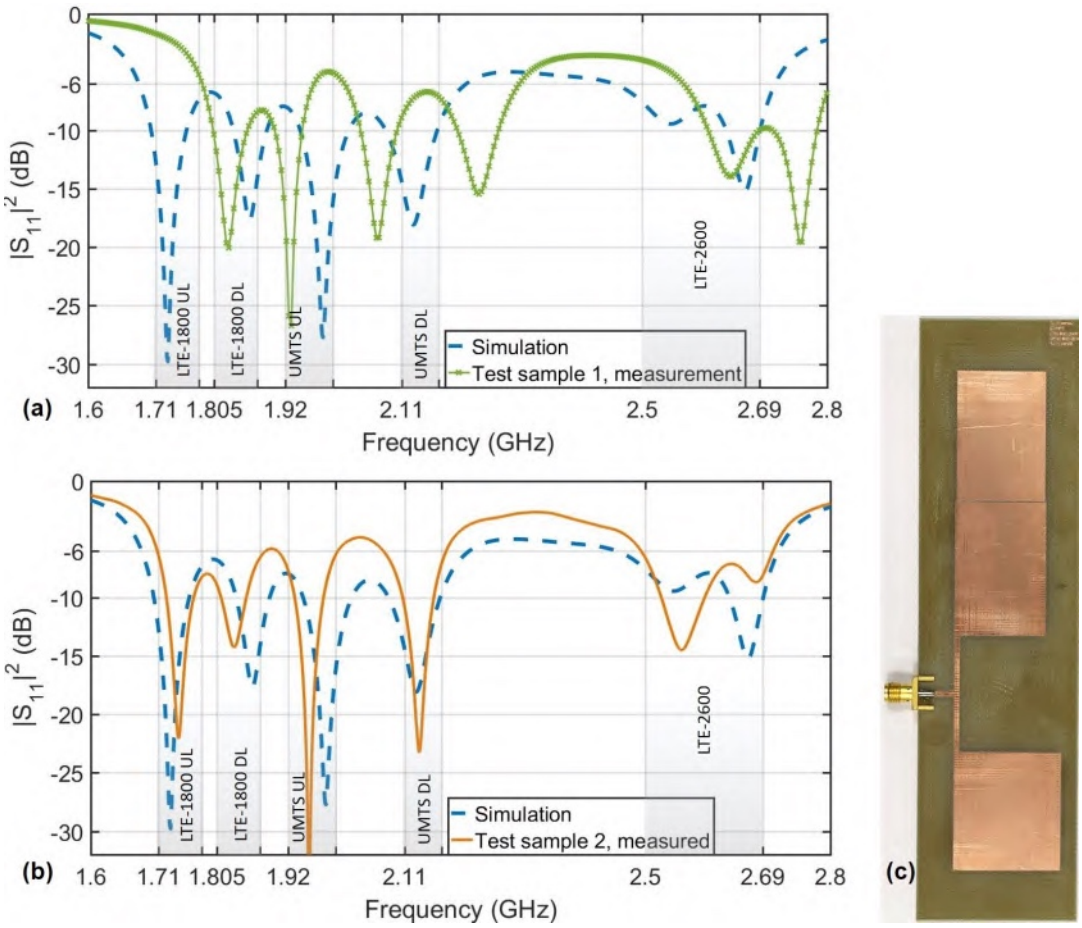

FIGURE 4.5: (a) Desired simulated reflection coefficient against the measured reflection coefficient of the first test sample. (b) Desired simulated reflection coefficient against the measured reflection coefficient of the optimized second test sample. (c) A snapshot of the second test sample.

the simulation. While at 1.95 GHz, the simulated and measured vertical radiation patterns were in good agreement, the measured horizontal pattern was stronger in intensity, for example by a factor of ≈ 6 dB at $\theta \approx 30^\circ$, in the range $\theta = 330^\circ...60^\circ$, moving anti-clockwise along the indicated arrow. As the measured antenna is not and cannot be an exact replica of the simulated antenna, along with the fact the simulation environment comprised only the antenna, a perfect correspondence between the simulated and measured results is not reasonable to expect over the entire frequency range. The peak values of simulated and measured directivity and realized gain, as well as the total efficiencies (including matching losses) are provided in Table 4.1. The maximum realized gain, 4.8 dBi, was measured at 2.6 GHz, while its minimum value, -1.7, dBi was obtained at 1.85 GHz. At the other frequencies, it was between 2...3 dBi.

Here, it was also interesting to take a look at the partial realized gains separately, as the combined realized gain loses information about the antenna polarization at the different frequencies of interest. Therefore, the measured peak partial realized gains, G_v in vertical polarization and G_h in horizontal polarization, are also presented in Table 4.1. We can see that at the TM_{10} mode resonance frequencies 1.75 GHz, 1.85 GHz, and 1.95 GHz, most of the radiated power is contained in the horizontal polarization, while at the TM_{01} mode 2.15 GHz and 2.6 GHz resonances, the power is concentrated in the vertical polarization, even though the realized gain patterns in

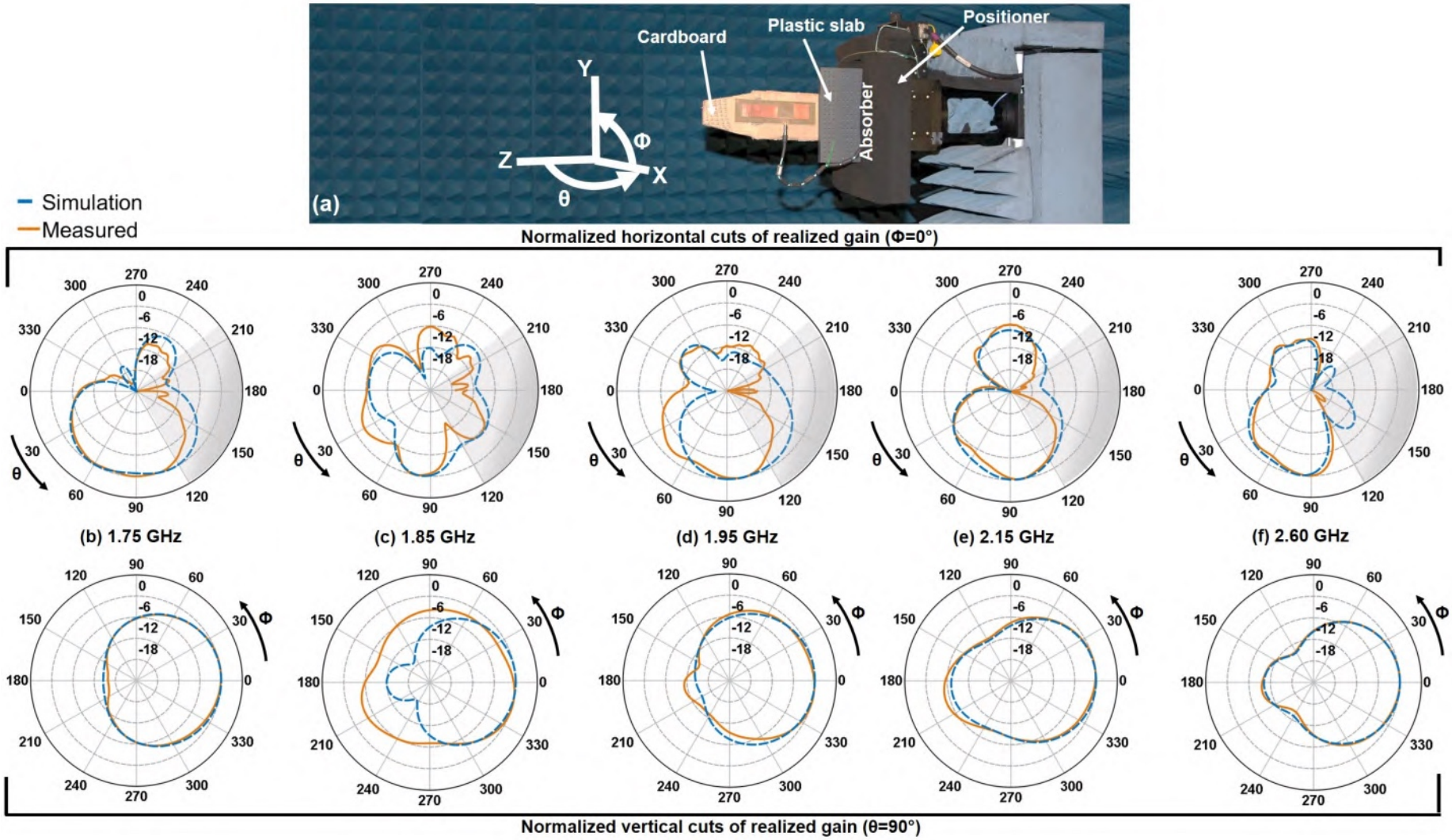

FIGURE 4.6: (a) Antenna measurement setup and coordinate system; x-axis is perpendicular to the antenna, with the antenna lying in the y-z plane. (b), (c), (d), (e), (f) Comparison of simulated and measured normalized horizontal and vertical cuts of the realized gain at the indicated frequencies. Grey area marks the approximate angular range where the positioner shadows the source antenna. [94] ©2019 IEEE

TABLE 4.1: Bare triple-patch antenna simulation and measurement comparison [94] ©2019 IEEE

Freq. (GHz)	Dir. (dBi)		Rlzd. gain (dBi)		Measured partial rlzd. gains (dBi)		Total efficiency (%)	
	Sim.	Meas.	Sim.	Meas.	G_h	G_v	Sim.	Meas.
1.75	4.7	5.8	0.4	2.1	2	-12.6	37	43
1.85	7.4	6.9	-0.7	-1.7	-2.2	-11.5	15	14
1.95	5.8	6.8	-0.9	1.9	1.4	-9.6	21	32
2.15	6.6	7.9	1.4	3.2	-8.6	2.8	30	34
2.6	7.8	8.3	2.5	4.8	-16.3	4.8	29	44

Fig. 4.6 follow a similar trend over the considered frequency range.

4.3.2 Measurements with partial door frame

As usual, embedding the antenna prototype without taking into account the influence of the relative permittivites of the ABS and PMMA layers of the plastic cover would mean that we would end up with an embedded antenna that would not resonate in the desired frequency range. But the previous experience with embedding the di-patch antenna in the plastic cover was helpful here, where the plastic cover shifted the frequency response of the antenna backwards by $\approx$ 100 MHz from the desired value. If we take another look at the bare triple-patch antenna reflection coefficients in Fig. 4.5 (a), we notice that the test sample 1 measured reflection coefficient was shifted forwards by $\approx$ 100 MHz. This meant that if a copy of test sample 1 were to be embedded in the plastic cover, the forward and backward shifts of 100 MHz would compensate each other, and the embedded antenna frequency response would cover the correct frequency range.

So, a copy of test sample 1 was embedded in the plastic cover. The simulated reflection coefficient (with a suitably adjusted permittivity value of the FR-4 substrate) and the measured reflection coefficient are presented in Fig. 4.7 (a). While there is not an exact overlap between the two curves, the embedded antenna sample was not optimized any further, as the $|S_{11}|^2 \leq$-6 dB criterion was met throughout the desired frequency range. Fig. 4.7 (b) shows the the electric field distribution at 1.75 GHz and 2.6 GHz on the door frame. As expected, the number of crests and troughs is larger at the higher frequency than at the lower frequency. Fig. 4.7 (c) presents the door frame measurement setup in AML, while the normalized simulated and measured radiation patterns are compared in Fig. 4.7 (d)...(h). A good degree of similarity can be observed between the radiation patterns. The typical simulated and measured values are enlisted in Table 4.2.

4.3.3 Measurements with the car

Considering that it would take several days to simulate such a multi-frequency antenna along with the car chassis, and occupy the entirety of the available departmental computational resources, such simulations were not performed. On the other hand, for an interesting measurement comparison, identical triple-patch antennas were embedded in the adjacent B-column plastic covers on the left side of the car, as indicated in the schematic in Fig. 4.8 (a). The VISTA measurement setup is presented in Fig. 4.8 (b), with the corresponding normalized measured radiation

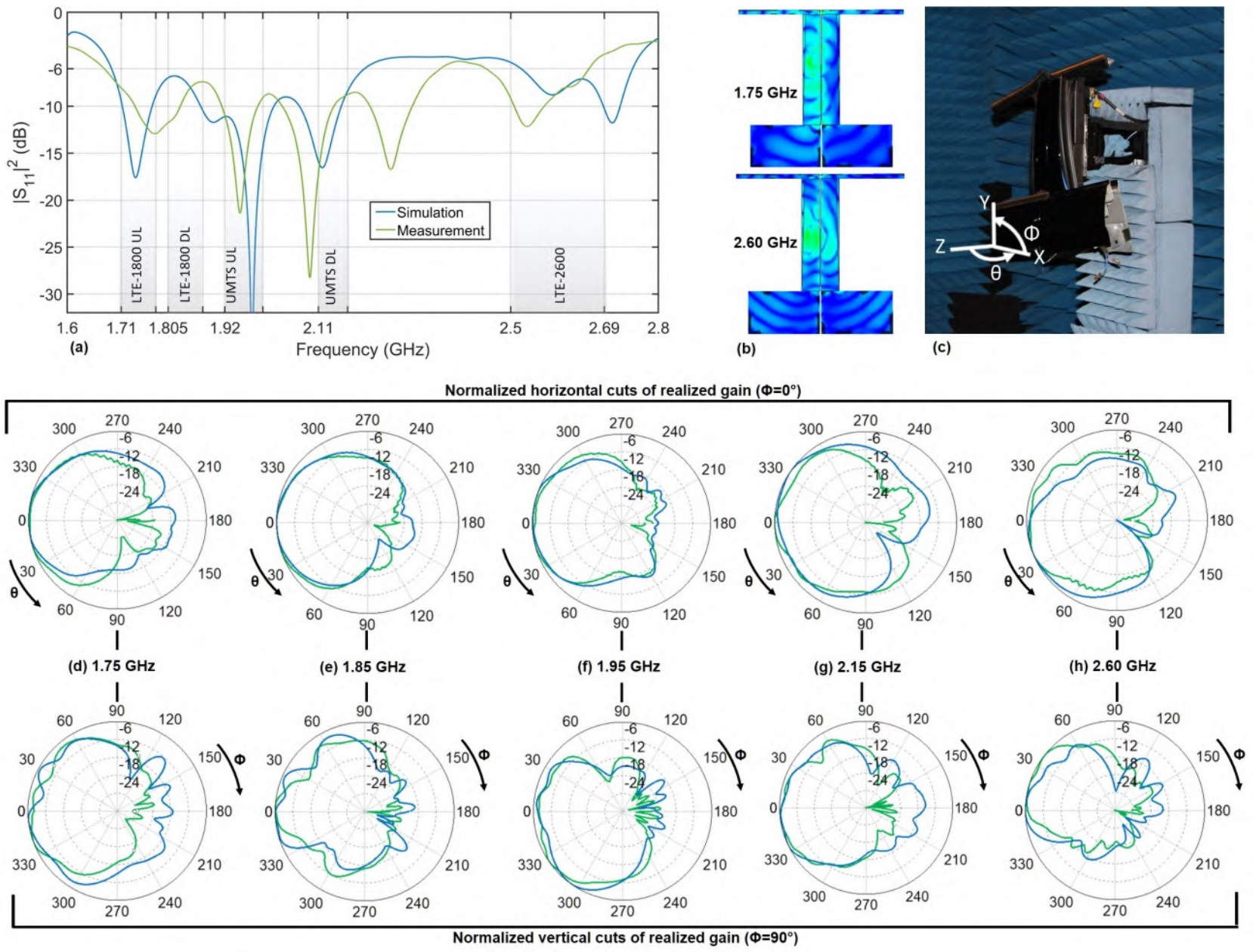

FIGURE 4.7: (a) Simulated and measured reflection coefficients for the door frame. (b) E-field distribution at the two extreme resonant frequencies. (c) Antenna measurement setup and coordinate system; z-axis is perpendicular to the door frame. (d)...(h) Comparison of simulated and measured normalized horizontal and vertical cuts of the realized gain at the indicated frequencies.

TABLE 4.2: Door frame triple-patch antenna simulation and measurement comparison.

Frequency (GHz)	Directivity (dBi)		Realized gain (dBi)		Efficiency (%)	
	Simulated	Measured	Simulated	Measured	Simulated	Measured
1.75	6.62	7.70	2.35	1.90	37.5	26.3
1.85	7.95	9.00	0.13	-0.50	17.0	11.0
1.95	7.10	7.40	-0.30	0.33	18.2	19.7
2.15	6.90	8.10	1.28	2.6	27.6	28.2
2.60	8.80	8.70	4.53	3.1	37.4	27.1

patterns in Fig. 4.8 (c)...(g). The excellent overlap between the front-left 1 and front-left 2 patterns, as well as the nearly identical measured values as listed in Table 4.3, indicate that the antenna performance remains practically the same between the adjacent covers. Quantitatively, following the embedding, the two antennas were around 20 cm apart from each other, which was a large enough separation to make this antenna combination suitable for LTE MIMO data rate measurements as considered in detail in chapter 6.

TABLE 4.3: Comparison of measured values for two triple patch antennas embedded in the adjacent plastic covers on the left side of the car.

Frequency (GHz)	Directivity (dBi)		Realized gain (dBi)		Efficiency (%)	
	Front-left 1	Front-left 2	Front-left 1	Front-left 2	Front-left 1	Front-left 2
1.75	10.3	10.7	3.8	3.9	22.5	20.7
1.85	9.9	9.8	0.14	0.5	10.5	12
1.95	10.6	10	1.72	1.5	13	14
2.15	9.6	9.7	1	1.1	14	14
2.60	9.4	9.1	3.3	3	25	23.7

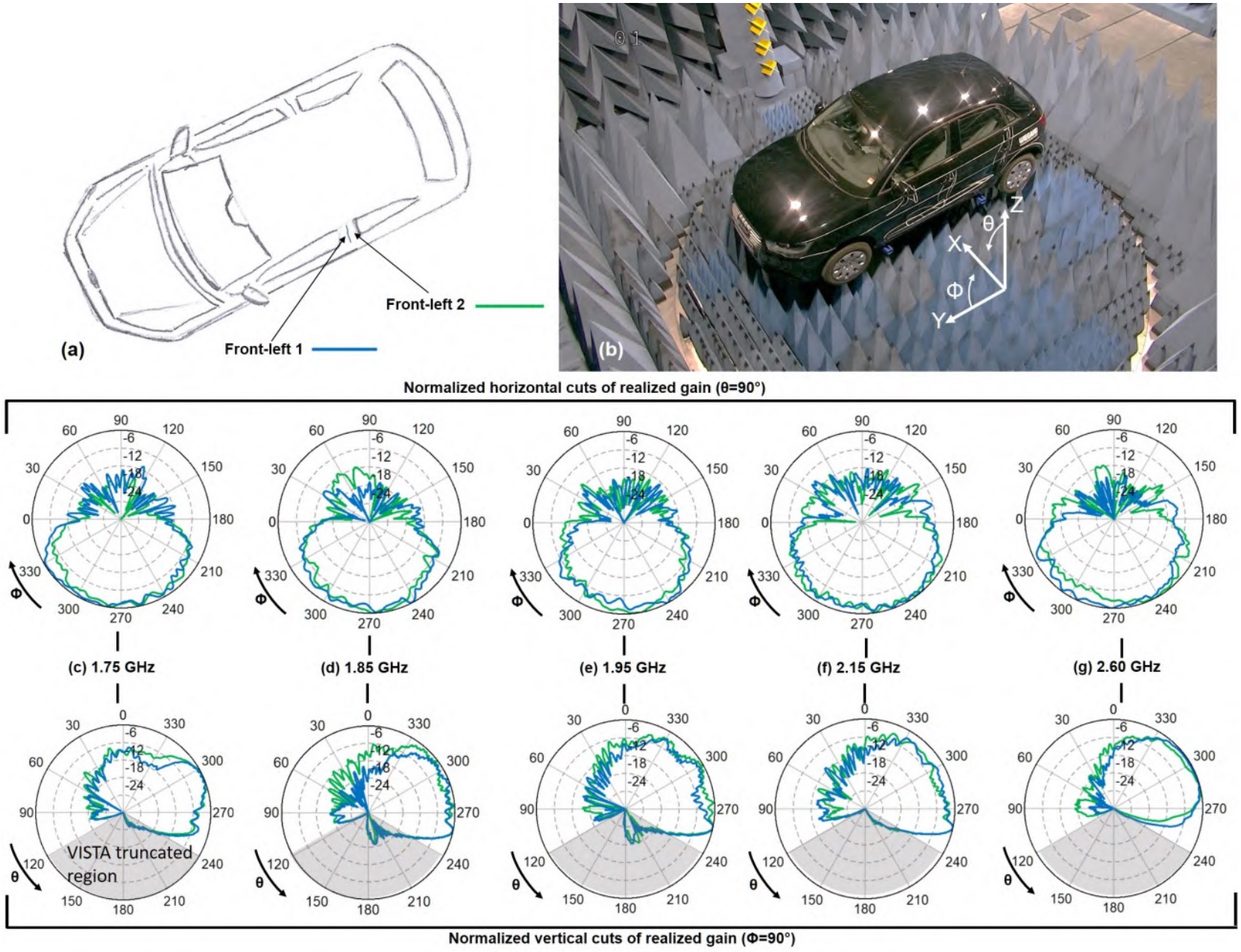

FIGURE 4.8: (a) Schematic indicating the location of the embedded antennas. (b) Measurement setup in VISTA. (c)...(g) Comparison of simulated and measured normalized horizontal and vertical cuts of the realized gain at the indicated frequencies.

Chapter 5

High impedance surface based dipole antenna

5.1 High impedance surface fundamentals

5.1.1 Achieving a high surface impedance

In chapter 3 on the di-patch antenna, the well-known limitation of a half-wavelength dipole antenna was presented, that it suffers from a debilitating impedance mismatch and therefore does not radiate efficiently when arranged closely above a metallic ground. The closer a half-wavelength dipole antenna lies to a metallic surface, the stronger is the destructive influence of the image current on the driving-point impedance of the antenna. But if we were to replace the electric-metallic ground with a magnetic ground, then the image current on the magnetic ground would instead add constructively with the current on the half-wavelength dipole antenna, enabling it to radiate efficiently. However, there exist no magnetic conductors in nature. But in the recent years, metamaterial surfaces that act as perfect magnetic conductors over a specific and adjustable frequency bandwidth have been developed. These metamaterials are known as high impedance surfaces (HIS), and a detailed discussion on these materials can be found in the work of Sievenpiper [97].

A simplified overview of the HIS principle is provided in this section. Consider the corrugated surface in Fig. 5.1 (a), also known as 'Fakir's bed of nails' [98]. The spacing between the corrugations is a small fraction of the operational wavelength, and as they are a quarter-wavelength in length, they transform the low surface impedance at the surface of the ground to an open-circuit condition at the top. For a half-wavelength dipole antenna laid horizontally closely above the corrugations, the image current will be in-phase owing to the open-circuit condition, and as a result the dipole antenna would resonate efficiently. However, there are two problems with this approach: (i) Quarter-wavelength long corrugations are simply too long at the

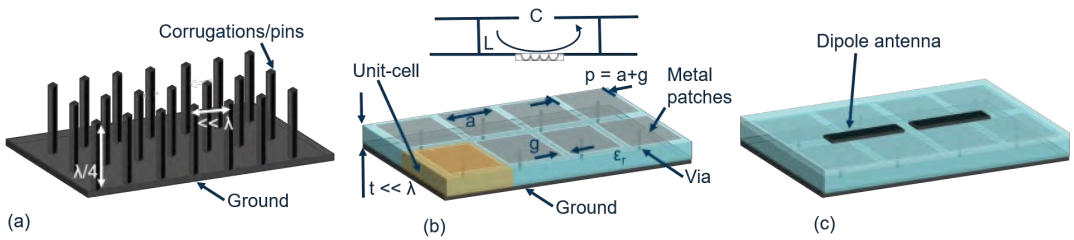

FIGURE 5.1: (a) A corrugated surface. (b) HIS as an array of unit cells, and the equivalent L-C model [96] ©2018 IEEE. (b) HIS with a dipole antenna printed atop an extra substrate layer [96] ©2018 IEEE.

typical mobile communication frequencies. For example, at 2.6 GHz, the corrugations would be ≈ 30 mm in length, which is not low-profile any more. (ii) If we place the half-wavelength dipole antenna quarter-wavelength above the metallic ground, there is no need for the corrugations in the first place, as at that distance from the ground, the dipole antenna and ground interfere constructively in any case. It is only if we are able to reduce the length of the corrugations, while maintaining the desirable high surface impedance condition at their top, that such metamaterials would be suited for a low-profile antenna design.

If the corrugations are embedded in a dielectric medium ϵ_r, the length of the corrugations/vias is shortened in accordance with the velocity factor of the dielectric medium. Additionally, the vias could be loaded with an array of patches which further bolster the dielectric constant through their effective capacitance, enabling the vias to be even smaller in length at the same resonance frequency. On doing this, we end up with the high impedance surface in Fig. 5.1 (b). In other words, a HIS can be imagined as a Fakir's bed of nails loaded with a dielectric substrate and an array of patches atop the vias [98]. Each metal patch-via combination with the underlying portion of the dielectric slab constitutes a unit cell, as highlighted in orange color. The period of repetition $p = a + g$ of the unit cells is small compared to λ (typically, $\lambda/10$). Such a material can be represented by an equivalent capacitance-inductance model; the array of patches contribute an effective capacitance C, and the grounded dielectric slab along with the vias contribute an effective inductance L. C and L in parallel lead to the surface impedance in eq. 5.1 [97]. It is clear from this equation that at resonance and a certain frequency bandwidth around it, the surface impedance offered by a HIS will be large compared to the free space impedance, η, and a dipole antenna printed atop such a surface, as in Fig. 5.1 (c), would couple efficiently to free-space, instead of being short-circuited.

$$Z_s = \frac{j\omega L}{\sqrt{1 - \omega^2 LC}} \tag{5.1}$$

5.1.2 Creation of an electromagnetic bandgap

The above discussion limited itself to how at resonance, a HIS provides an in-phase reflection of the incident wave, but this is not the sole advantage/application of such surfaces.

Depending upon its construction, a HIS can offer in addition an electromagnetic bandgap located around its resonance frequency, wherein the TM and TE surface waves are forbidden to propagate. Whereas TM waves occur on inductive surfaces and have neither a lower cut-off frequency nor an upper cut-off frequency, TE surface waves manifest on capacitive surfaces, but have a lower cut-off frequency. As ordinary metals have an inductive surface impedance, they support TM waves at all frequencies. Grounded dielectric slabs, on the other hand, support TE surface waves above a cut-off frequency at which the effective dielectric thickness is slightly over one quarter-wavelength and the surface impedance is capacitive. As a consequence, such slabs support both the surface wave modes; the TM waves propagate closer to the underlying metal surface, where the impedance is effectively inductive, and the TE waves propagate closer to the top surface of the substrate where the impedance is effectively capacitive. [97]

A lot of the times, one would like to prevent the propagation of these surface waves, as they contribute to undesirable effects on the antenna performance. In case of printed antenna arrays, they enhance the mutual coupling between the array elements,

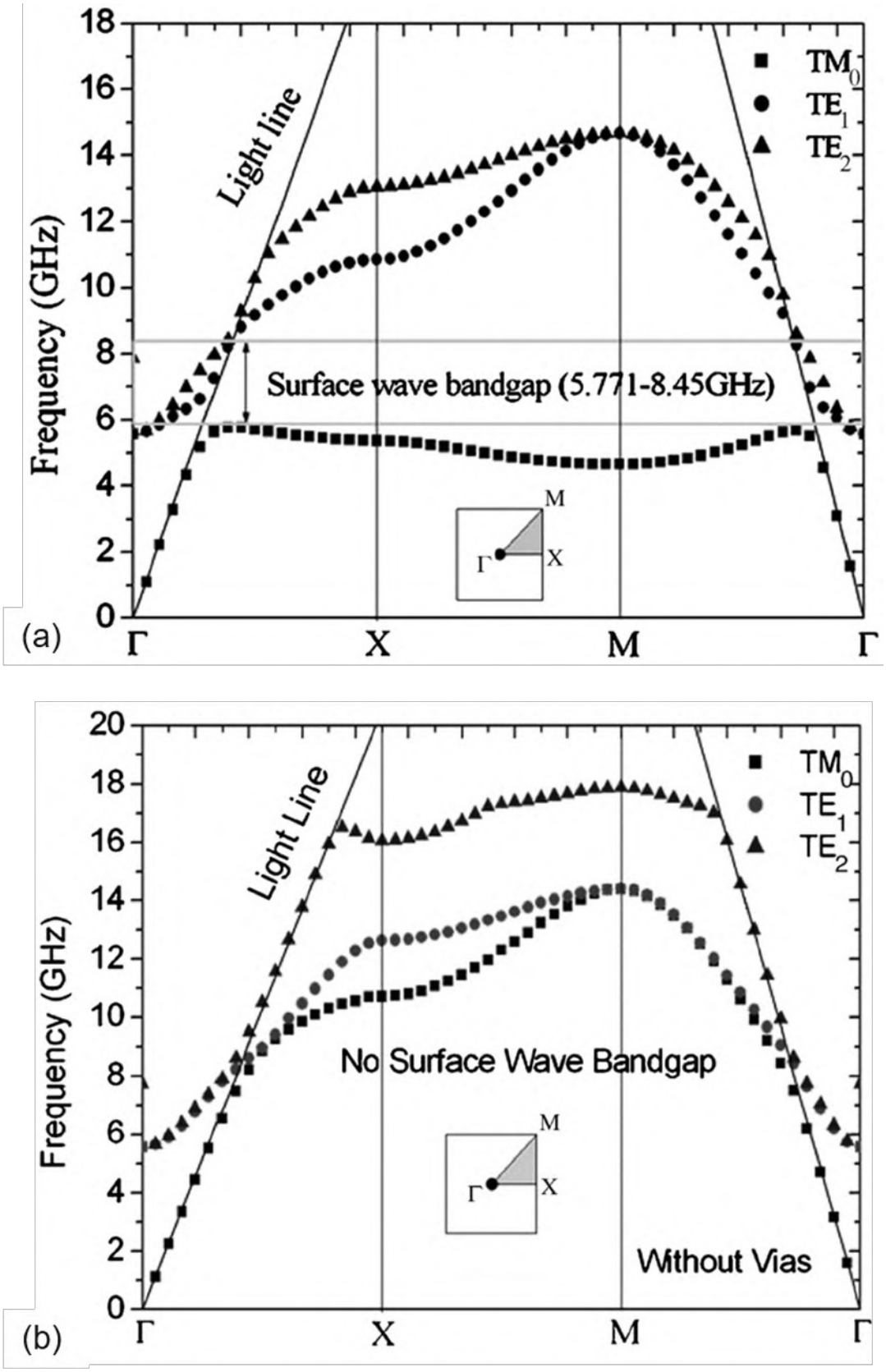

FIGURE 5.2: Dispersion diagrams for: (a) A patch-loaded grounded dielectric slab including vias, and (b) a patch-loaded grounded dielectric slab without vias. (Reprinted from [100], with the permission of AIP Publishing)

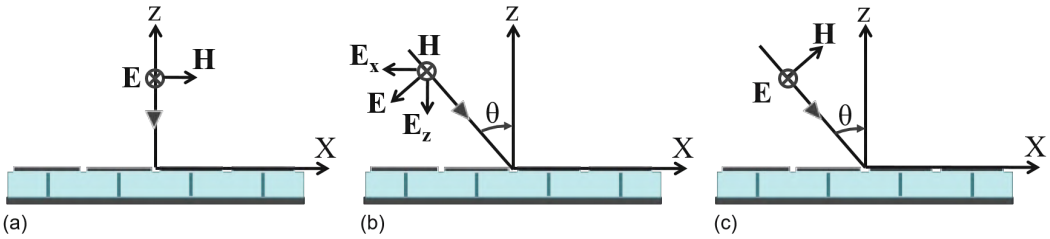

FIGURE 5.3: (a) Normally incident plane wave. (b), (c) Obliquely incident TM polarized plane wave/TE polarized plane wave.

and in general can lead to the formation of ripples or nulls in the radiation patterns of printed antennas. If the TM surface waves could be cut-off at an upper frequency that lies below the lower cut-off frequency of the TE waves, an electromagnetic bandgap would be created wherein no surface waves would be supported. If the aforementioned grounded dielectric slab is converted into a HIS, in that the slab is loaded with an array of patches and vias as in Fig. 5.1 (b), such an electromagnetic bandgap can be created. Consider the dispersion diagrams taken from [100] in Fig. 5.2. Both are for same-in-design high impedance surfaces resonant at $\approx$ 6 GHz, except that the HIS in Fig. 5.2 (a) has vias, while the vias are absent in Fig. 5.2 (b). We can see that in the first case, the TM surface wave mode is suppressed from propagating at frequencies higher than 5.8 GHz, leading to the creation of an electromagnetic band gap between 5.8...8.45 GHz. Whereas if the vias are absent, then the TM surface waves propagate at all frequencies, and there is no band gap as evident from Fig. 5.2 (b). The presence of vias in a HIS is therefore of prime importance if an electromagnetic band gap is desired. As the frequency increases, the TM surface waves attempt to propagate closer to the underlying inductive metal surface. In such a case, the presence of vias on the metal surface slows down the TM surface waves, and eventually they stop propagating [97].

As important as the vias are for the creation of a bandgap, their presence or absence does not influence the reflection phase behavior of a HIS for a plane wave incident normally to the surface [97, 99]. Referring to Fig. 5.3 (a), in case of a normal incidence of a plane wave, the electric field would be perpendicular to the vias, because of which no current would be induced on the vias. In such a case, even if the vias were absent, the reflection phase behavior of the HIS would remain the same (see Fig. 3 in [99]). Vias play a role in the determination of reflection phase in cases where a plane wave strikes a HIS at an angle. Here also, the influence of vias is more significant if the obliquely incident plane wave is TM polarized as in Fig. 5.3 (b), as only then would there be a component of the electric field, E_z, directed parallel to the vias, which would induce a current flow in them. In such a case, the HIS starts exhibiting a dual resonance due to the coupling effect of the current induced on the patches and the current induced on the vias [100, 128]. For a TE polarized obliquely incident plane wave as in Fig. 5.3 (c), the electric field would once again be perpendicular to the vias, rendering them inactive, as no current is induced on them, so the resonance is determined by the current induced on the patches. An elaborate discussion along with results pertaining to this topic is presented in [100, 128] for the interested reader.

For the antenna design under consideration, the creation/existence of a band gap was not of prime importance. The primary interest was in a low-profile dipole antenna that could efficiently radiate after embedding in the plastic cover of the

car, considering the extremely small distance between the back side of the plastic cover and the car metal chassis following the mounting of the plastic cover onto the car. As discussed already, a typical dipole antenna would not radiate under such circumstances. A suitably designed HIS-dipole antenna combination would not only be low-profile, but also radiate efficiently after embedding in the plastic cover, as well as not be affected by the car metal chassis located closely behind the embedded HIS. As a HIS with or without vias could fulfill this requirement, it was chosen not to include vias in the HIS design; the reduced design complexity would also imply reduced manufacturing costs, and faster simulation times.

The remainder of the chapter is organized as follows. Section 5.2 considers the design of the HIS-dipole antenna for operation in the LTE-2600 frequency band from 2.5...2.69 GHz. We begin by discussing the unit-cell design, and how to determine the phase-frequency behavior of such a unit-cell through simulations. Thereafter, we present a HIS made up of a 3×8 array of unit-cells with a dipole antenna on its top that functions in the desired frequency range, and analyze the influence of selected parameter variations on the reflection coefficient of the HIS-dipole combination. In section 5.3, we consider the bare HIS-dipole, partial door frame, and car measurement results and compare these to their corresponding simulation results.

5.2 HIS-dipole antenna design for LTE-2600

5.2.1 Unit-cell/HIS design, reflection phase and bandwidth

The concept of the unit-cell design used for the presented HIS was taken from [101, 102]. Suitable adjustments were made to the substrate permittivity and the size of the unit-cell, so as to obtain a desirable phase-frequency response. The side-view of the constructed unit-cell is presented in Fig. 5.4 (a). The unit-cell consists of the usual ground layer at the bottom, a square patch layer at the top, and an additional intermediate layer of 45° rotated patches, as shown separately in Fig. 5.4 (b). The substrate materials between the metallizations, and above the top patch had slightly different relative permittivities. Initially, the unit-cell was designed with a uniform permittivity value in simulations, but such a multi-layer design involving substrate layers of non-standard thicknesses could only be realized with substrate materials of slightly differing permittivity values in the prototyping phase. Therefore, the permittivity values were adjusted accordingly in the simulations. The additional patch layer raises the capacitance of the unit cell, allowing the unit cell to satisfy the condition $p \leq \lambda/10$ at 2.6 GHz, where $\lambda/10 \approx 10$ mm, for the considered ≈ 1.7 mm unit-cell thickness. To compute the reflection phase that would be offered by a HIS composed of such unit-cells, we applied a periodic boundary condition around the four sides of a single unit-cell as visible in Fig. 5.3 (c). The bottom face of the unit-cell was assigned a perfect electric boundary as well. The unit-cell was excited with a normally incident plane wave from the top, and the reflection phase was recorded at an interface close to the top surface of the unit-cell.

The computed reflection phase is presented in Fig. 5.3 (d). Following [103], we know that the usable reflection phase bandwidth, wherein a printed dipole will exhibit a good reflection coefficient lies in the $90° \pm 45°$ range, and is not centred around 0° reflection phase. The same authors also intuitively explain in [104] the reasoning behind this range. A 0° reflection phase leads to a strong constructive interference between the HIS and the dipole, while a 180° reflection phase corresponds to a strong destructive interference between the HIS and the dipole. In both these cases, the dipole antenna would not be well-matched to 50 Ω. This implies that a

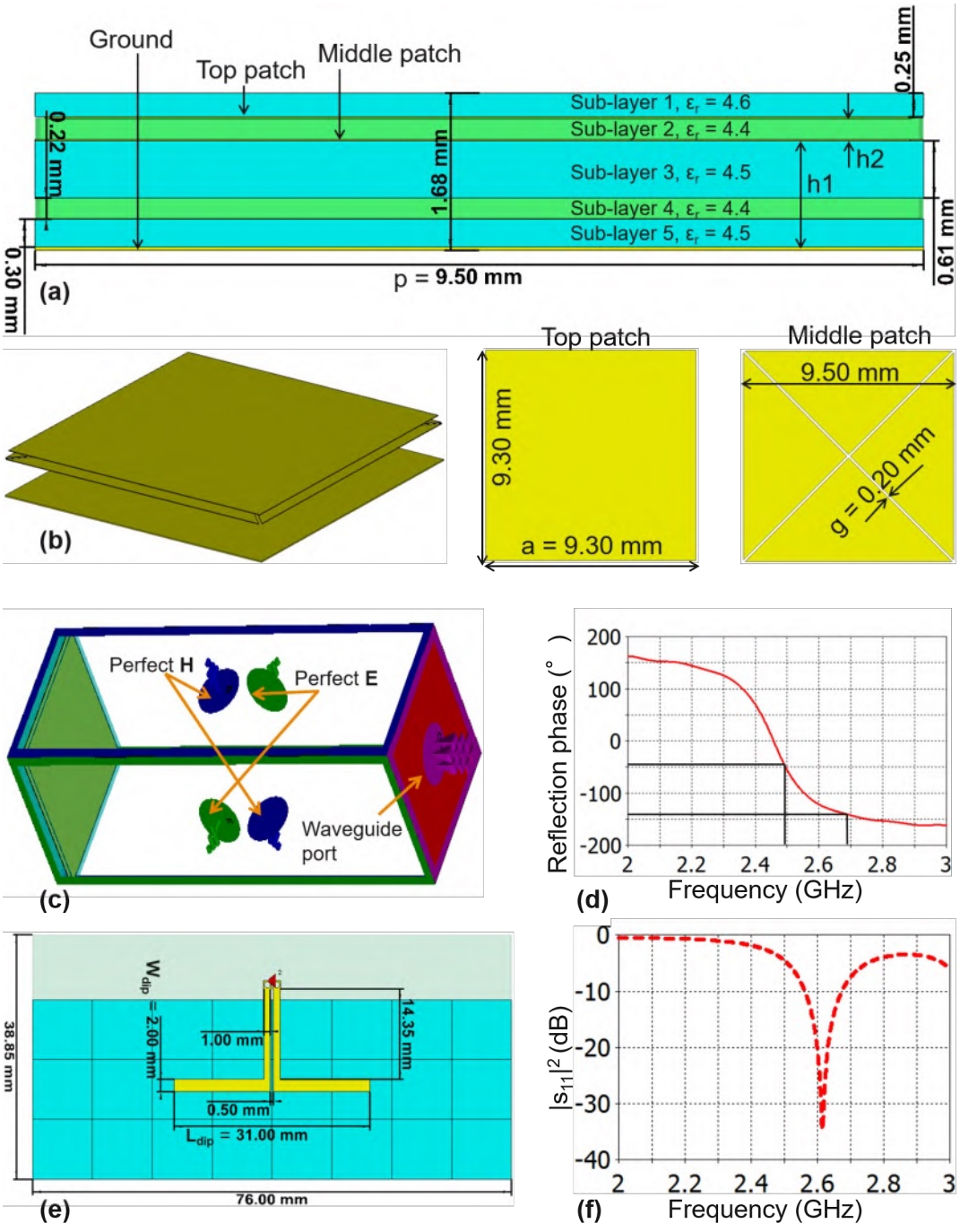

FIGURE 5.4: (a) Side-view of the unit-cell indicating the various dimensions and material properties. (b) 3-D view of the three metal layers in the unit-cell along with their dimensions. (c) Boundary conditions for unit-cell simulations. (d) Phase response of the simulates unit-cell. The region indicated with the black lines would be where an overlying dipole antenna would resonate. (e) 3×8 array of unit cells with a half-wavelength electrical dipole antenna printed on top. (f) Reflection coefficient of the HIS-dipole antenna combination.

dipole antenna would achieve a good impedance matching at a HIS reflection phase that lies in the middle of 0° and 180°. Unsurprisingly, as shown in [105], a dipole antenna can also be resonant in the $-90^\circ \pm 45^\circ$ reflection phase of a HIS. In general, these usable reflection phase ranges are variable to an extent, depending upon the height of the dipole above the HIS and the design of the HIS, but are usable design guidelines in any case.

As the arrays of patches in the unit-cell boost the effective capacitance of the unit-cell, thus keeping the cell small in size, it is a valid question to ask if the same reflection phase could be obtained by simply using a high dielectric permittivity substrate material and leaving out the patch arrays altogether. After all, a high substrate permittivity also implies a higher effective capacitance, and in that it is equivalent to an array of patches embedded in a low permittivity substrate. The authors in [103] considered this question. They had a unit-cell with an overlying array of patches and substrate $\epsilon_r = 2.2$. Keeping the cell thickness constant, they needed to raise the substrate permittivity almost 10-folds in order to obtain a similar reflection phase behaviour without the patch array as with the patch array. So, even though the array of patches in a unit-cell is exchangeable with an appropriately increased substrate permittivity, the permittivity required would be extremely high, and such substrate materials are expensive, and high permittivity also implies a narrower impedance bandwidth. At the same time, it is clear from the previous discussion that if an electromagnetic bandgap is required, that would not be achievable with a grounded dielectric slab.

5.2.2 Unit-cell/HIS-dipole parametric study

Various unit-cell design parameters, namely the unit-cell size p, the thicknesses $h1$ and $h2$, and the permittivities of the substrate layers were varied by +5% and the effect on the cell reflection phase behaviour for a normally incident plane wave excitation was observed. These parameters are indicated in Fig. 5.4 (a) and (b). In addition, the corresponding impact on the reflection coefficient of the HIS-dipole antenna was also studied. It is natural to expect that a shift in the reflection phase of a single unit-cell due to parametric variations should produce a corresponding shift in the reflection coefficient of the HIS-dipole comprising these unit-cells, which is exactly what transpired, as may be noted from the curves presented in Fig. 5.5 (a)...(e). We can observe that the direction of the shift in the dipole reflection coefficient follows the shift in the reflection phase of a single unit-cell. Quantitatively, there are some differences in the amount of frequency shift in the unit-cell reflection phase and the HIS-dipole reflection coefficient. This may be attributed to the fact that while the reflection phase is computed for an infinite array of unit-cells through the periodic boundary conditions, the HIS-dipole is strongly truncated. Thereby, an exact quantitative match between the corresponding results cannot be expected. The parts (f) and (g) of Fig. 5.5 present the reflection coefficients for a variation in the dipole antenna length and width. From this study, one may come to the conclusion that for the same factor of variation relative to the original value of the parameters, the substrate permittivity, patch size p, and the dipole length have the most significant influence on the dipole antenna reflection coefficient.

5.2.3 HIS-dipole curvature tolerance

As HIS-dipole antennas are relatively new types of antennas, it was also sensible to test the curvature tolerance of the design. To do this, the same approach was

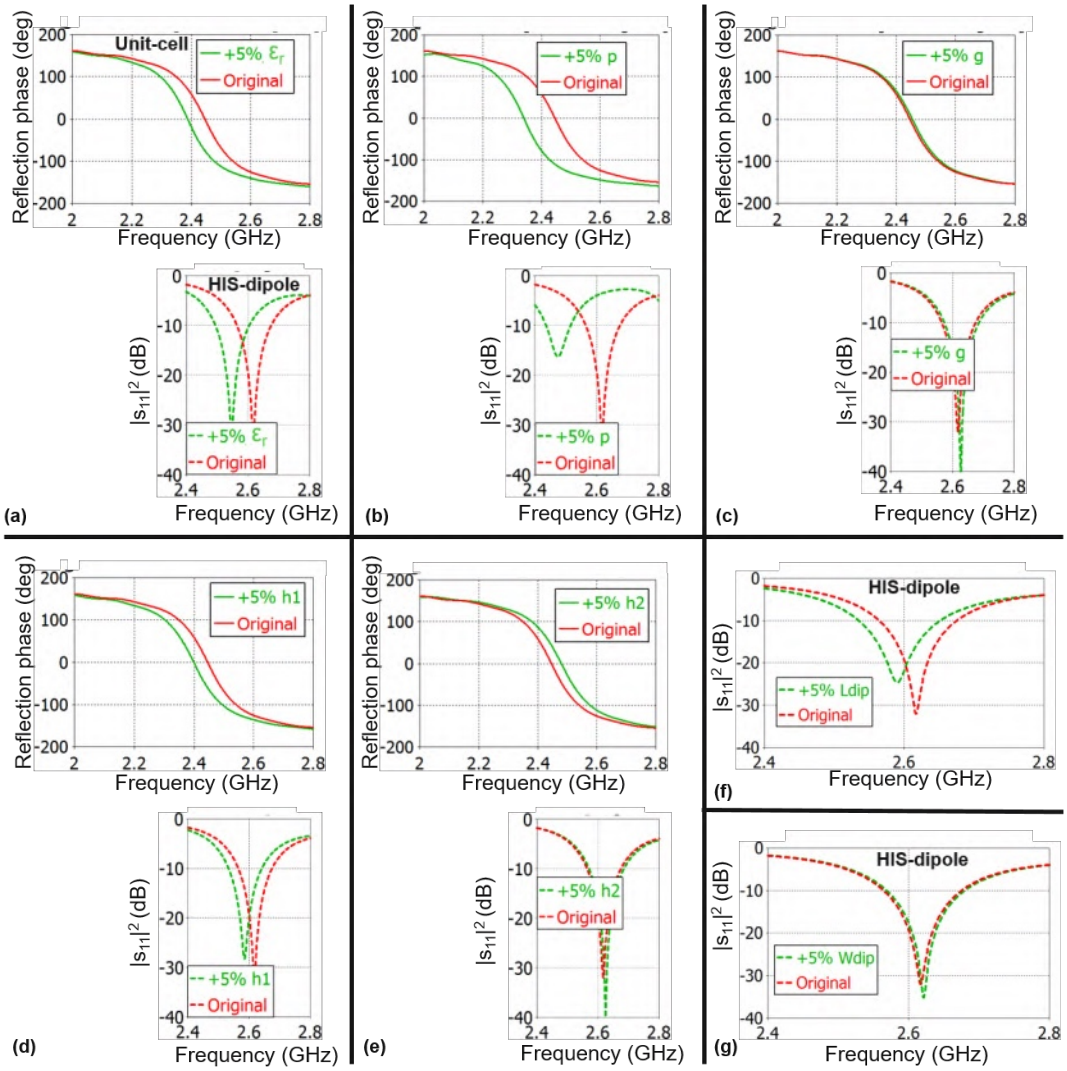

FIGURE 5.5: (a)...(e) Impact of a +5% increase in the various parameters of the unit-cell as indicated in Fig. 5.4 (a) on the reflection phase of the unit-cell as well as the reflection coefficient of the HIS-dipole combination resulting from these unit-cells. (f), (g) Impact of a +5% increase in the length L_{dip} and width W_{dip} of the printed dipole on the reflection coefficient.

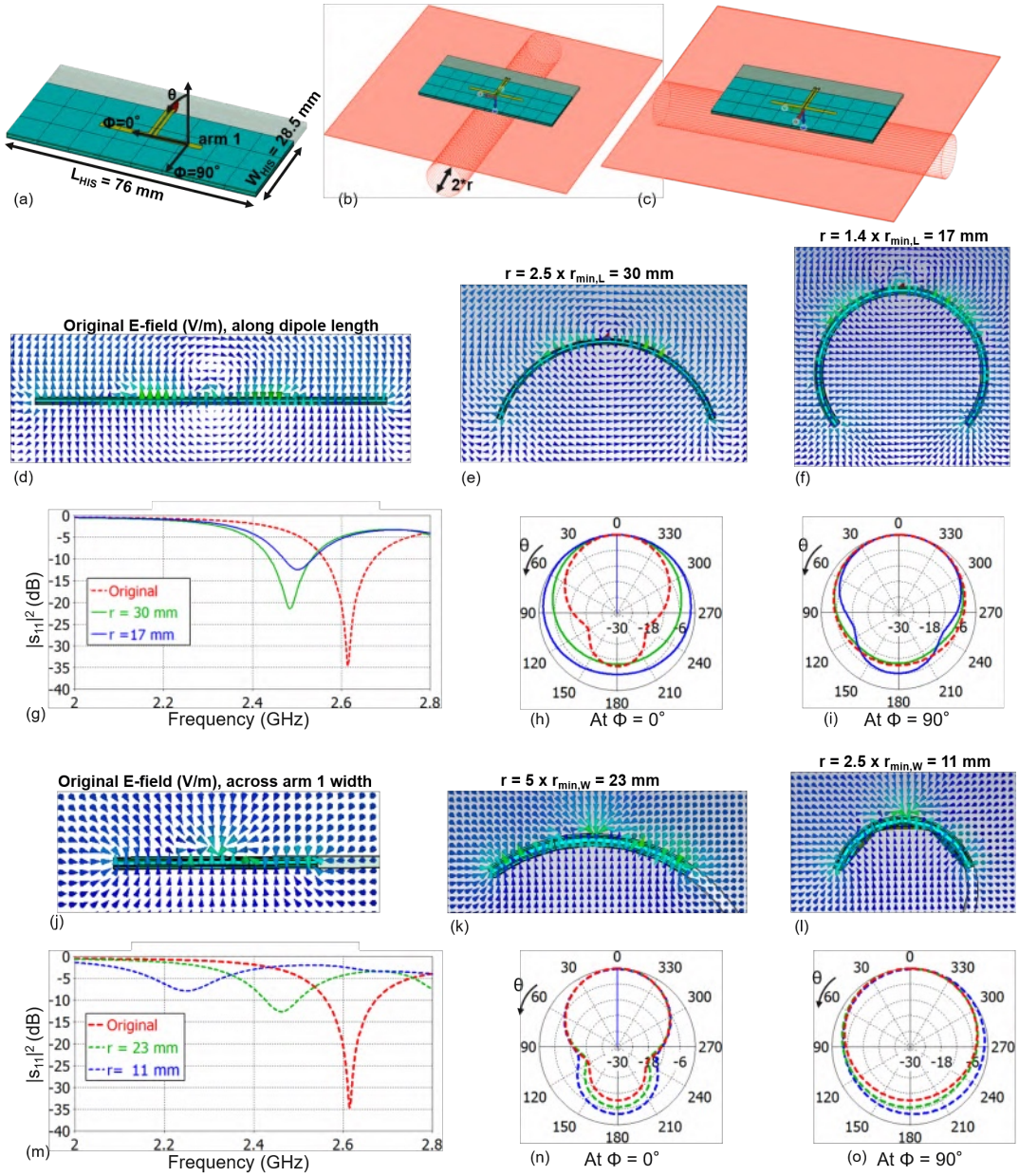

FIGURE 5.6: (a) HIS-dipole antenna with the reference coordinate system. (b), (c) Virtual cylinder of radius r for bending the HIS-dipole along its length or width. (d) Reference E-field distribution along the length of the HIS-dipole. (e), (f) E-field distribution with bending along the length. (g)...(i) The corresponding reflection coefficients and normalized directivity patterns. (j) Reference E-field distribution along the width of the HIS-dipole. (k)...(o) Results for bending along the width.

TABLE 5.1: Simulated values for bent HIS-dipole

Bend type	Bending radius (mm)	Directivity (dBi)	Realized gain (dBi)	Total efficiency (%)
No bend	—	5.7	3.9	67
Along length ($r_{min,L}$ = 12 mm)	r = 2.5×$r_{min,L}$	4.6	2.5	62
	r = 1.4×$r_{min,L}$	3.3	0.3	51
Along width ($r_{min,W}$ = 4.5 mm)	r = 5*×$r_{min,W}$	5.2	3.6	70
	r = 2.5*×$r_{min,W}$	4.2	2.4	52

followed as with the di-patch antenna in chapter 3, section 3.3. The length of the HIS was assumed to be the perimeter of a circle, and the radius $r_{min,L}$ corresponding to that perimeter was calculated. $r_{min,L}$ then represents the radius of bending for which the HIS would form a complete circle if bent along its length. Similarly, $r_{min,W}$ was calculated for bending along the width. The HIS-dipole was then bent cylindrically along its length and width for two different factors of $r_{min,L}$ and $r_{min,W}$, and the resulting influence on the reflection coefficient and the radiation patterns was noted. These results are presented in Fig. 5.6. Independent of whether the bend is along the length or the width, there is a downwards shift in the resonant frequency. However, for a comparable amount of bending along the width, there is a stronger impact on the depth of the reflection coefficient; we can see in Fig. 5.6 (m) that the blue curve no longer crosses the -10 dB level. As far as the radiation patterns are concerned, there is a decrease in the directivity as a portion of the power starts radiating in other directions in the lower hemisphere, as the field components bend along with the bending of the antenna. The simulated values are enlisted in Table 5.1. In general, this shows that HIS-dipole antennas are also well suited for conformal applications.

5.2.4 HIS truncation influence on the radiation pattern

If a HIS were infinite in its extent, then all the radiation from an overlying dipole antenna would lie in the upper half-sphere, but an infinite HIS is a theoretical construct; in reality a HIS is always truncated. The question arises how far can one proceed with the truncation of a HIS before the radiation performance of the overlying dipole antenna is considerably affected/degraded, if it is degraded at all. To ascertain this, the 8×3 HIS was taken as a reference and was truncated turn-wise along its length and width. The impact on the dipole antenna reflection coefficient and radiation pattern is presented in Fig. 5.7. First and foremost, we may observe that be the truncation along the length or the width, there was an upwards shift in the resonance frequency, as well as a deterioration in the reflection coefficient. The extended frequency range in Fig. 5.7 (i) shows that the original as well as the truncated HIS has a second resonance at around 3.2 GHz. As opposed to the dipole resonance at 2.6 GHz, the primary contributor of this additional resonance are the differential feed lines. If the differential lines are removed and the dipole antenna is fed directly in the middle, the resonance at 3.2 GHz disappears. In the case of the 4×3 unit-cell, the primary resonance frequency shifts upwards so as to almost overlap with the secondary resonance contributed from the differential feed lines. This has an influence on the radiation pattern as well, as in the main beam in this case has a slight tilt compared to the other cases. In general, the directivity decreases with the truncation of the HIS. This is understandable, because a smaller ground plane beneath the antenna, allows a portion of the radiation to escape to the lower hemisphere. The key values from the simulation are provided in Table 5.2.

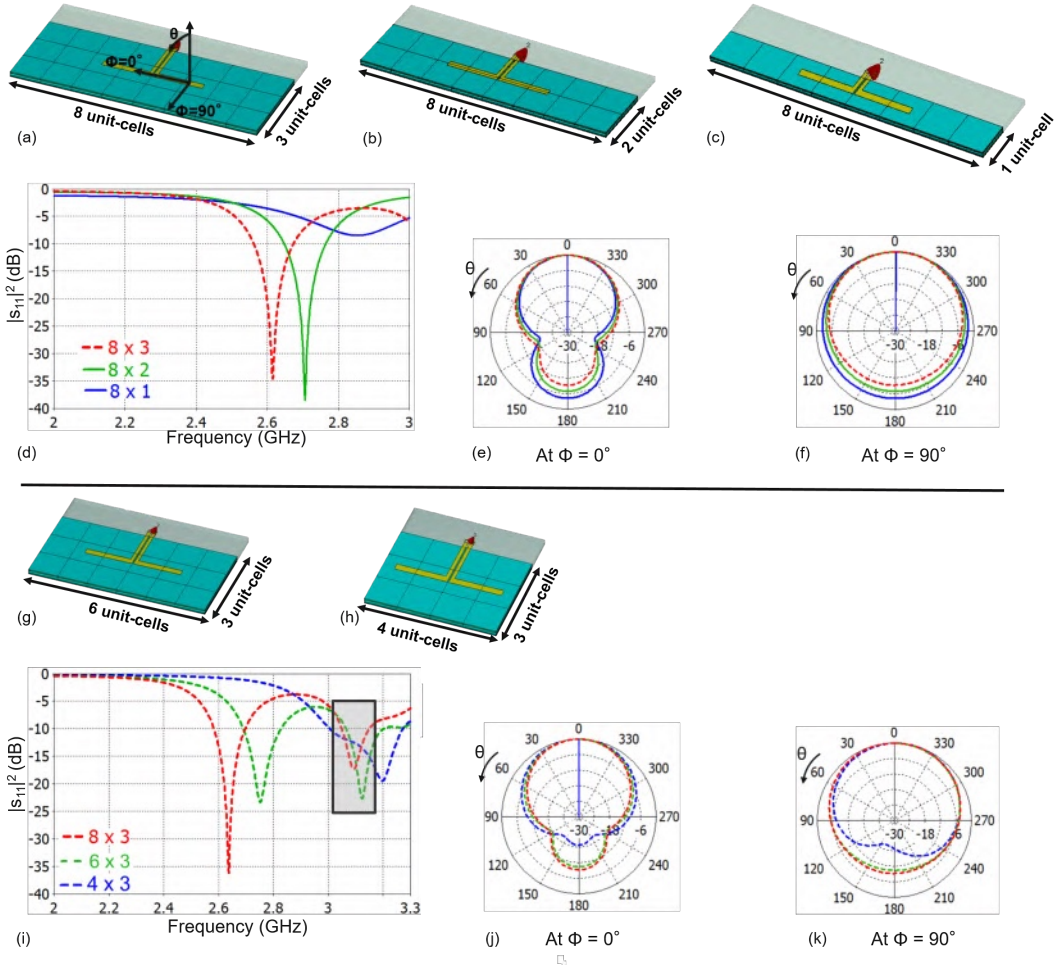

FIGURE 5.7: (a) HIS-dipole antenna with the reference coordinate system. (b), (c) HIS-dipole antenna with 1 and 2 rows of cells removed. (d)...(f) Corresponding reflection coefficients and normalized radiation patterns. (g), (h), HIS-dipole antenna with 2 and 4 columns of cells removed. (i)...(k) Corresponding reflection coefficients and normalized radiation patterns.

TABLE 5.2: Simulated values for truncated HIS-dipole configurations

Configuration	Directivity (dBi)	Realized gain (dBi)	Efficiency (%)
8 x 3	5.7	4	67.4
8 x 2	5.2	3.8	72
8 x 1	4.5	2.4	62.4
6 x 3	5.5	3.8	67
4 x 3	5.7	2.7	50

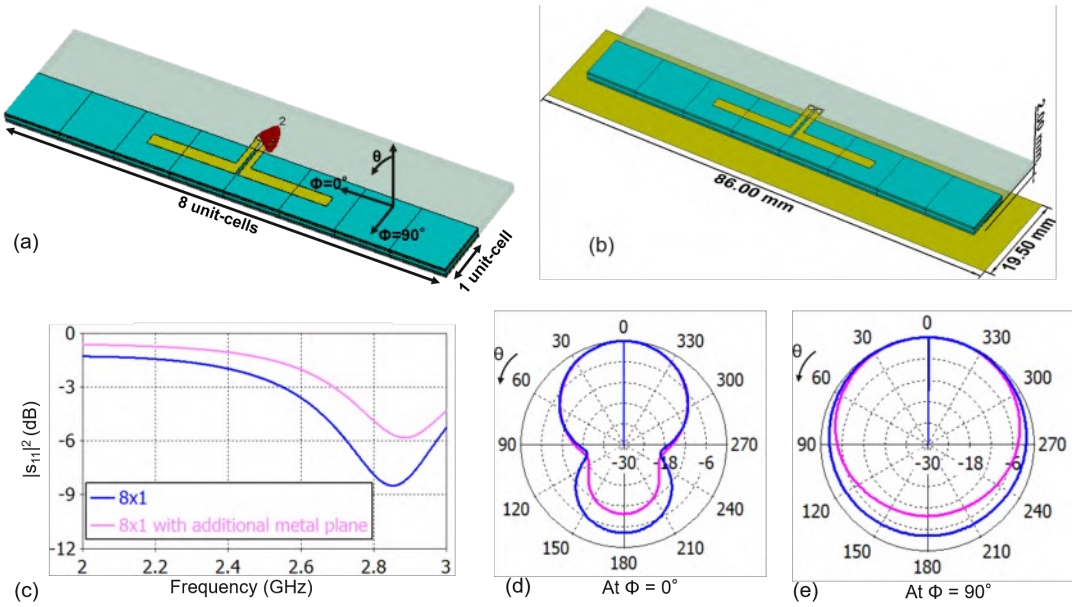

FIGURE 5.8: (a) 8x1 HIS-dipole in free space, along with the coordinate system. (b) The same HIS-dipole, but with an additional metal sheet at a distance of 2 mm underneath it. (c)...(e) Corresponding relfection coefficients and normalized radiation patterns.

TABLE 5.3: Simulated values for 8×1 HIS-dipole with and without additional metal sheet.

Configuration	Directivity (dBi)	Realized gain (dBi)	Efficiency (%)
8 x 1	4.5	2.4	62.4
8 x 1 (additional metal sheet)	6	2.44	44

Focusing on the 8×1 HIS case, and its corresponding reflection coefficient (blue curve) in Fig. 5.7 (d), it is interesting to note that even for such a starkly truncated HIS, a significant amount of -6 dB impedance bandwidth was available. But, as in our intended application, there would additionally be the car metal chassis underneath the HIS, it is important to ask if the matching level would further degrade for the 8×1 HIS as a consequence of this mounting situation. If not,then it would mean that large high impedance surfaces may not be necessary for applications like ours, unless a -10 dB impedance matching is absolutely desired. The 8×1 HIS was simulated with an additional rectangular metal sheet 2 mm underneath, to determine the impact on the reflection coefficient. These results are presented in Fig. 5.8 along with the corresponding values in Table 5.3, whereby it can be observed that the introduction of the additional metal sheet led to a further degradation of the reflection coefficient as well as the radiation efficiency. This shows that for low-profile applications closely above the car chassis, to preserve a reasonable level of matching, a HIS should not be truncated to the absolute smallest size permissible.

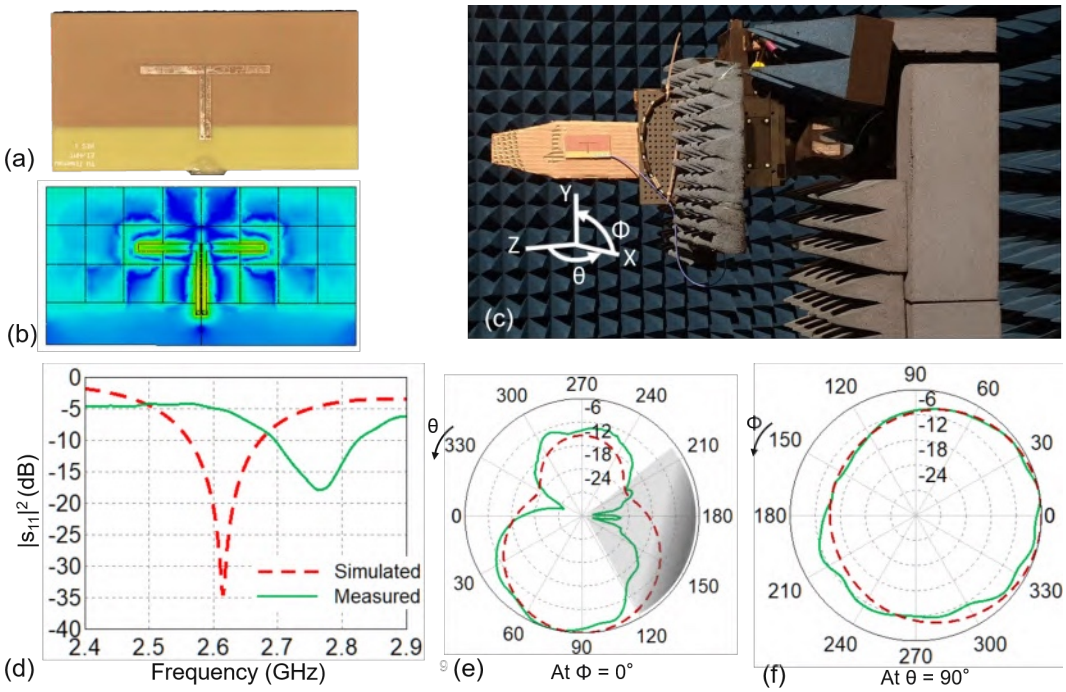

FIGURE 5.9: (a) HIS-dipole prototype. (b) Electric field distribution at 2.6 GHz. (c) Measurement setup; x-axis is perpendicular to the antenna. (d) Simulated and measured reflection coefficient. (d), (e) Normalized simulated and measured radiation patterns compared at 2.6 GHz and 2.75 GHz respectively. The greyed area indicated approximately the region in which the antenna is shadowed by the positioner.

TABLE 5.4: Bare HIS-dipole simulated and measured values (2.6 v/s 2.75 GHz). Bold compensate the 0.5 dB chip balun insertion loss.

	Simulation	Measurement
Directivity (dBi)	5.7	6.3
Realized gain (dBi)	4	2.2/**2.7**
Total efficiency (%)	67.4	39/**43.6**

5.3 Simulation and measurement comparison

5.3.1 Bare HIS-dipole antenna measurements

Fig. 5.9 (a) shows the HIS-dipole antenna prototype, the corresponding electric field distribution at 2.6 GHz is depicted in Fig. 5.9 (b), wherein the distribution typical of a half-wavelength dipole antenna can be observed. The remaining parts in the figure show the measurement setup and the simulated and measured results. The measured reflection coefficient had an approximately 150 MHz forwards shift, comparable to what has already been observed in the previous chapters. The simulated and the measured radiation patterns are comparable, except in the grey angular range where the positioner shadows the antenna. The key simulated and measured values are presented in Table 5.4.

As here also the same chip balun [79] was soldered at the HIS-dipole feed point, as in the case of the di-patch antenna, the 0.5 dB insertion loss due to the balun needs to be calibrated out of the measured realized gain and efficiency for a fair comparison with the simulation, where simply a discrete port was used to excite the HIS-dipole.

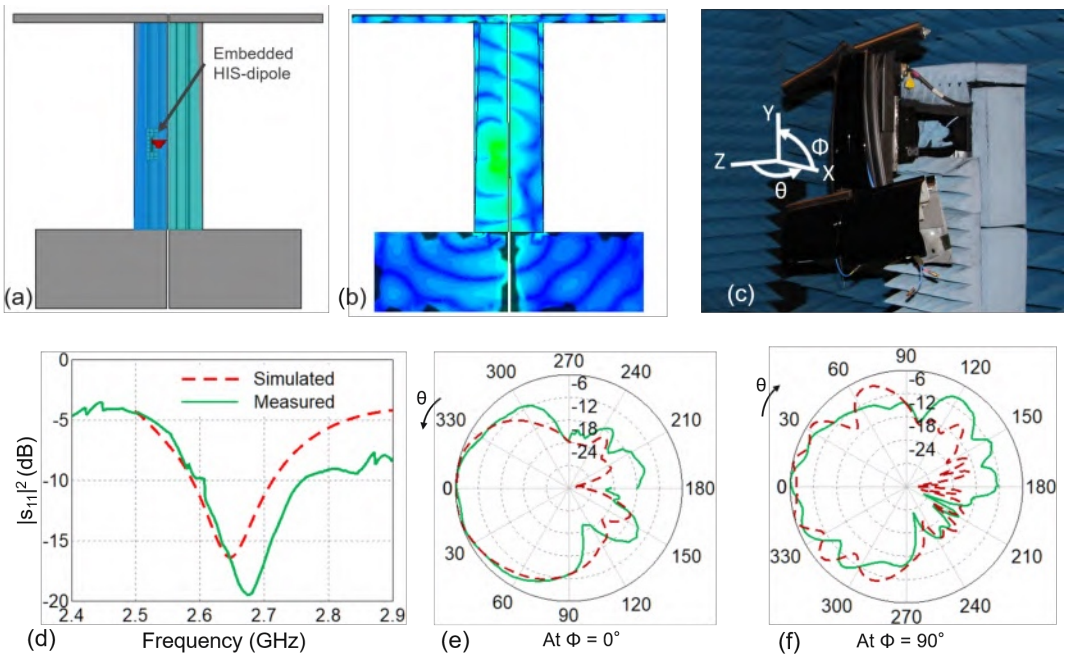

FIGURE 5.10: (a) Simulated model of the door frame, including the HIS-dipole antenna. (b) Electric field distribution at 2.6 GHz. (c) Measurement setup; z-axis is perpendicular to the door frame. (d) Simulated and measured reflection coefficients. (e), (f) Normalized simulated and measured radiation patterns.

TABLE 5.5: Door frame HIS-dipole simulated and measured values. Values in bold compensate the 0.5 dB chip balun insertion loss.

	Simulation	Measurement
Directivity (dBi)	7.8	7.3
Realized gain (dBi)	6.1	2.6/**3.1**
Total efficiency (%)	66.7	34/**38**

The adjusted measured values are written in bold in Table 5.4 and other subsequent tables containing measurement data.

5.3.2 Measurements with partial door frame

The simulation and measurement results with the door frame are presented in Fig. 5.10. Fig. 5.10 (a) and (b) show the simulated door frame model and the electric field distribution on it at 2.6 GHz respectively. We can notice that the surface wave propagation is dominant along the slit between the two doors, which gives rise to the ripples in the vertical cut of the radiation pattern in Fig. 5.10 (f), whereas the horizontal radiation patterns in Fig. 5.10 (e) are relatively smooth in the upper hemisphere. There was a good match between the simulated and the measured reflection coefficients. The key values from the simulation and measurement results are presented in Table 5.5.

5.3.3 Measurements with the car

The simulation of the car chassis including the HIS-dipole antenna followed the hybrid simulation procedure elucidated in chapter 2. It is worth reiterating such a

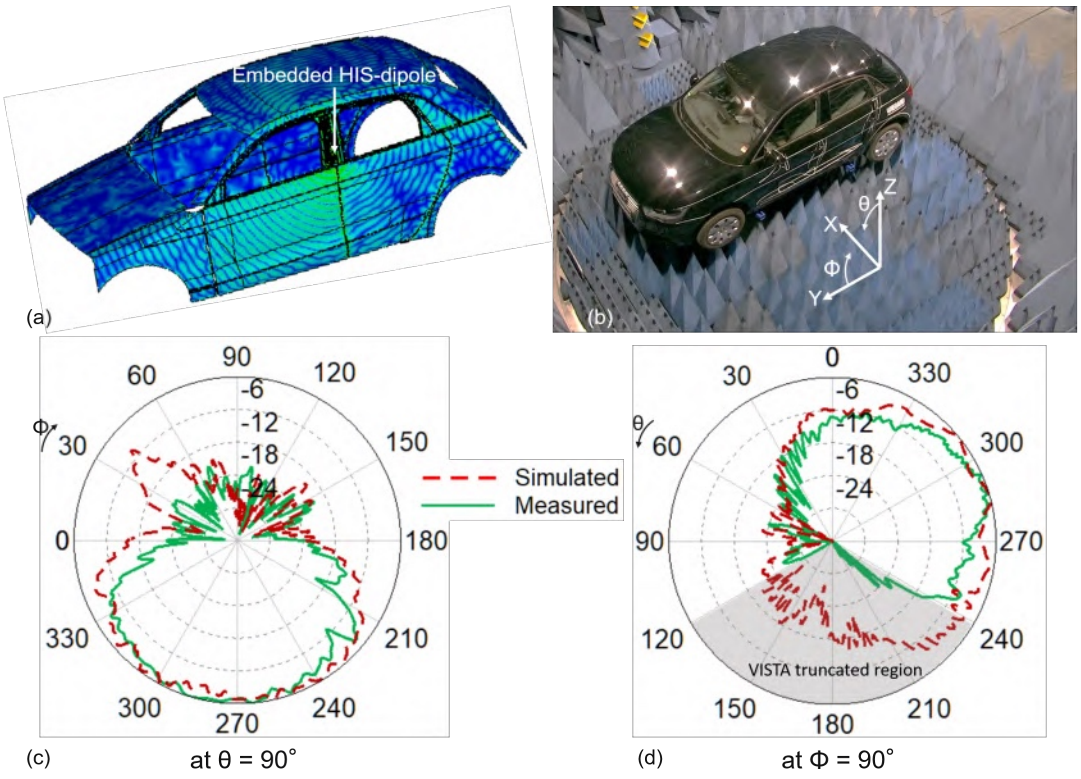

FIGURE 5.11: (a) Electric field distribution on the car at 2.6 GHz. (b) Measurement setup in VISTA. (c) Comparison of normalized simulated and measured radiation patterns.

TABLE 5.6: Car HIS-dipole simulated and measured values. Values in bold compensate the 0.5 dB chip balun insertion loss.

	Simulation	Measurement
Directivity (dBi)	6.9	10
Realized gain (dBi)	4.1	2.8/**3.3**
Total efficiency (%)	53	19.4/**21.4**

simulation is good enough to provide an intuitive qualitative insight into some of the measured observations, but due to the simplified chassis model and the hybrid simulation procedure it should not be relied upon too much quantitatively.

The electric field distribution on the car at 2.6 GHz is shown in Fig. 5.11 (a). Surface waves are pronounced not just along the slit between the doors, but also along the length of the car. As the car is longer in length than in height, the number of secondary radiation sources produced by surface waves is comparatively larger along the length. Accordingly, a larger number of ripples can be seen in the horizontal cut of the radiation pattern as opposed to the vertical cut in Fig. 5.11 (c) and (d) respectively. In general, the pattern shapes are comparable in both the planes. The key simulated and measured values are presented in Table 5.6

Chapter 6

System aspects, LTE MIMO measurements and V2V field tests

6.1 Towards a plastic embedded automotive antenna system

The previous chapters considered the simulations and measurements of primarily single antennas embedded in the front-left B-column plastic cover. The fact that there are two B-column plastic covers available on the left and right sides of an Audi A1, and most of the other passenger cars for that matter, was not utilized. For one, embedding the same types of antennas in multiple plastic covers would enable MIMO functionality to provide higher mobile communication data rates, and secondly, with antennas on the left and right sides of the car a close to omnidirectional coverage in the horizontal plane could be established.

This chapter aims at exploring the aforementioned aspects, and providing answers to many of the preliminary questions that arise at the onset of such system design considerations. The two most fundamental questions among them are: (i) The extent of omnidirectionality achievable with embedded antennas on the left and right sides of the car in comparison to a commercially available car rooftop monopole antenna, (ii) LTE MIMO data rate achievable with the embedded antennas as opposed to with the rooftop monopoles. The other questions are consequential to the two fundamental ones. One would be interested in understanding the the reasons for the differences, if any, in the MIMO data rates achieved by the plastic embedded antennas and the rooftop monopoles, as well as the reasons for the variability of the MIMO performance measured over a certain time duration in general.

For measuring the radiation patterns of the embedded antennas and the rooftop monopoles, VISTA was used in the fully anechoic configuration. The multiband patch antenna was chosen for embedding in the left and right side covers of the car. The reason for this choice was the multiband behaviour itself; one would be able to measure the radiation patterns over a 1.71...2.69 GHz frequency range, as opposed to at a single frequency as would be in the case of a di-patch antenna. This allowed for the comparison of the radiation patterns on the left and right sides of the car over a wider frequency range. These patterns are discussed in section 6.2. For the LTE MIMO data rate measurements, VISTA was used in the semi-anechoic configuration, with the pyramidal absorbers removed from the floor to facilitate multipath propagation. The Rohde & Schwarz CMW500 communications tester [107] was used for generating LTE signals for the transmit antennas, and the data rate achieved in the downlink with the plastic embedded antennas and the rooftop monopoles was measured with a network performance analysis tool known as 'iperf' [108]. The details pertaining to these measurements are presented in section 6.3.

It is also important to mention at the onset that this chapter does not provide a finished system design. Several other questions necessary to that end have not been

considered as a part of this thesis. For example, one among these questions is where the processing of the signals received/transmitted by these embedded antennas would take place. The RF front-end should be possibly as close to the antennas as possible, so as to avoid longer transmission lines between the antenna and the front-end, as these would lead to additional RF losses. From an economics point of view, a good solution would be the one that can be integrated into the car without the need for modifications to the car body. Or as a first proof-of-principle, a car model may be chosen which allows for a straightforward integration of the antenna-front end combination. The successful demonstration of the principle with such a car would act as a motivator for modifying other car geometries where such an integration would not be possible otherwise. At the time of writing this thesis, such questions are being considered in the follow-up project entitled 'smarte integrierte funksysteme für vernetzte mobilität und logistik (SISYVOS)' [109].

6.2 Radiation characteristics of multiband patch antennas embedded in the left and right covers

Towards the end of chapter 4, the radiation characteristics of multiband patch antennas embedded in the two adjacent B-column plastic covers on the left side of the car were considered. For this chapter, a third multiband antenna was embedded in the front-right plastic cover of the car, as shown in Fig. 6.1 (a). In principle, it was the same as the multiband antenna of chapter 4, with the difference that the feeding line was extended 7 cm vertically. Considering the intention of integrating a front-end along with the antenna in the future, such a vertical feed line extension was sensible for two reasons: (i) Given the limited width of the plastic cover, and practically no space between the cover and metal chassis along the cover length, front-end integration could only be envisioned at the bottom end of the plastic cover, where more space was available in width, as well as in the distance from the car chassis. (ii) The amount of additional loss contributed by such a line extension could be ascertained. As far as point (ii) is concerned, simulations showed that a 7 cm long microstrip line on a 1.6 mm thick FR-4 substrate ($tan\delta$ = 0.023) dampened an input signal by $\approx$ 0.7 dB at 2.6 GHz. Measurements in VISTA, whereby the radiation performance of a front-right B-column plastic cover integrated multiband antenna without microstrip line extension and with microstrip line extension was compared, corroborated the additional loss suggested by the simulations. Otherwise, the radiation patterns were identical between these two antenna variants. As a whole, the radiation patterns and peak directivities and gains for the right side embedded antenna were comparable to the antenna pair embedded on the left side of the car within the design frequency range 1.71...2.69 GHz. These values for the left side embedded antenna may be read from Table 4.3 in chapter 4; for the right side embedded antenna the difference to these values was negligible.

In Fig. 6.1 (a), the front-left 1, front-left 2, and front-right antennas have also been indicated as Rx1, Rx3, and Rx3 antennas respectively, as these acted as receive antennas for downlink data rate measurements at 1.85 GHz described in the next section. Downlink data rate was also measured for a pair of reference monopoles, ref1 and ref2, placed on the roof of the car. Fig. 6.1 (b) and (c) present the normalized horizontal and vertical gain patterns of the indicated antennas. Especially focusing on the horizontal pattern, one may notice that the monopole is omnidirectional, whereas in case of the embedded antennas, irrespective of whether the Rx1/Rx2 combination or the Rx1/Rx3 combination is chosen, there is always a null along the

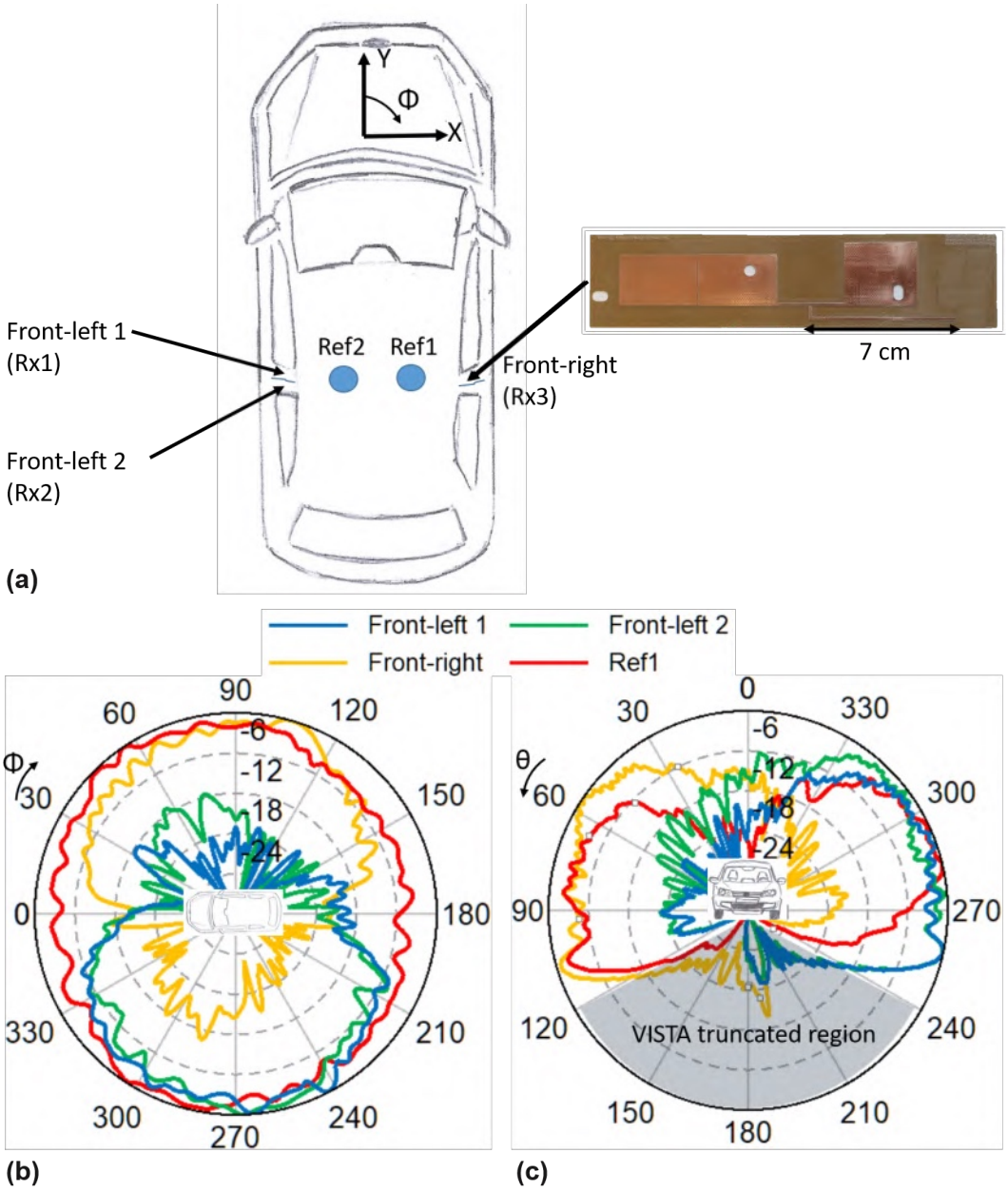

FIGURE 6.1: (a) A car schematic indicating the location of the various antennas, including a snapshot of the triple-patch antenna with the elongated feed line. (b), (c) Normalized measured horizontal and vertical cuts of directivity for the embedded antennas and the rooftop monopole, Ref1, at 1.85 GHz.

driving direction. This information would be helpful in interpreting some of the data rate measurement results presented ahead.

6.3 LTE MIMO data rate measurements

6.3.1 MIMO data rates achievable with LTE

In general, for an $N \times M$ MIMO system, with $N,\ M > 1$, a data rate $min(N,\ M)$ times than that for a SISO system is achievable under rich multipath conditions. Therefore, let us first consider the maximum data rate possible with a SISO wireless LTE link, which is dependent upon the chosen modulation scheme as well as the channel bandwidth.

LTE advanced releases 8...11 offer three types of modulation schemes, namely, QPSK, 16-QAM, and 64-QAM in the downlink [110, 115], and one of these is chosen depending upon the channel conditions. Naturally, higher order modulation schemes imply a higher data rate, but it is not a good strategy to always select the highest order scheme for this reason. Broadly, the selection strategy is as follows: (i) The eNodeB transmits a reference signal to the user equipment (UE). (ii) The UE computes the signal-to-interference-plus-noise ratio (SINR), and depending upon the SINR value, transmits back a corresponding channel quality indicator (CQI) value to the eNodeB. (iii) Based upon the received CQI value, the eNodeB selects the highest modulation scheme and code rate such that the packet error rate remains below 10% [111]. There are 15 CQI values available in LTE, lower values correspond to QPSK and higher to 64-QAM (see Table 1 in [111]). As far as the channel bandwidth is concerned, 4G LTE permits bandwidths of 1.4, 3, 5, 10, and 20 MHz [115]. Naturally, the higher the channel bandwidth, the higher would be the data rate.

In LTE, the smallest unit of resources that can be allocated to a user is known as a physical resource block (PRB). The resource element (RE) is the smallest physical channel unit, each uniquely identifiable by its subcarrier index k and symbol index l within the PRB. A PRB spans 12 subcarriers over 7 OFDM symbols and in total $12 \cdot 7 = 84$ REs. One PRB pair is the smallest schedulable unit in most downlink cases, and fits into two 0.5 ms consecutive slots as shown in Fig. 6.2. [112-114]

Based upon this information, the data rate offered by a SISO wireless LTE link may be computed as follows [115]:

1. Assume C MHz as the selected channel bandwidth. 10% of C represents the guard bandwidth, therefore the proportion of the channel bandwidth available for data is $B = 0.9 \cdot C$ MHz.

2. Since each PRB is 0.18 MHz in bandwidth, the number of PRBs in a slot required for B MHz channel bandwidth = $B/0.18 = P$.

3. Each PRB has 84 resource elements or OFDM symbols. Therefore, the number of OFDM symbols contained in P PRBs = $P \cdot 84 = R$

4. Let K be the number of bits/symbol corresponding to the selected modulation scheme. The total number of bits needed for representing R OFDM symbols in a 0.5 ms slot = $K \cdot R = K_{Tot}$.

5. 25% of the transmit data is control data, and the rest is user data. Considering this, the SISO data rate for the user may now be given as: $D_{SISO} = 0.75 \cdot K_{Tot}/(0.5 \cdot 10^{-3})$ bits/s. Then, as mentioned, $D_{MIMO} = min(N,\ M) \cdot D_{SISO}$ under ideal channel conditions.

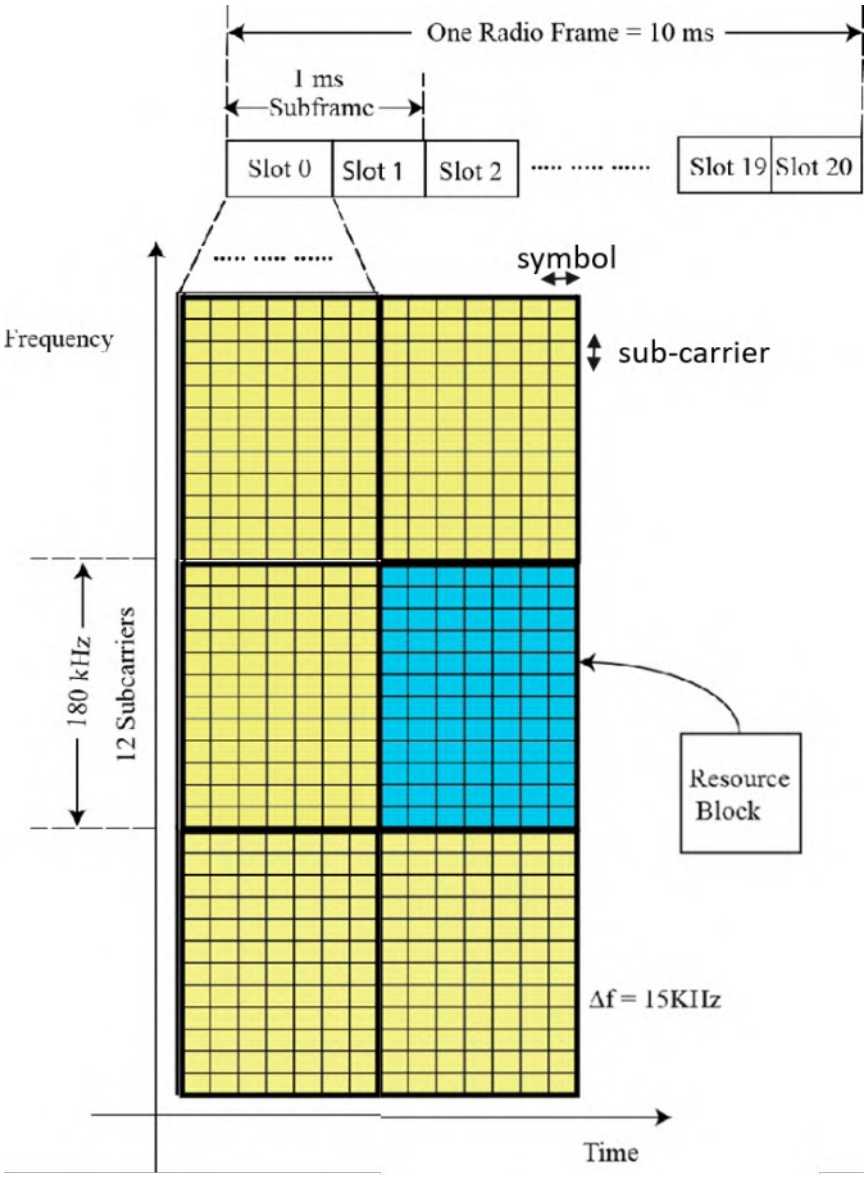

FIGURE 6.2: LTE frame structure (adapted from [112]).

6.3.2 Measurements in VISTA and comparison to field tests

The entire measurement set-up in VISTA is shown in Fig. 6.3 (a), along with an equivalent schematic in Fig. 6.3 (b). The Audi A1 with plastic embedded antennas (Rx1, Rx2, Rx3) and the rooftop monopoles (Ref1, Ref2; Fig. 6.3 (c)) was placed at the centre of the 6.5 m diameter turntable. We can see that inside the car was a Huawei E8372 USB-stick LTE modem [116] with inputs for two LTE antennas. The modem was connected to a laptop which was executing the network performance measurement program iperf for measuring the downlink data throughput. The Rx1 and Ref1 antennas were not only used for receiving LTE data during the measurement, but also for transmitting the channel quality information to the Rohde & Schwarz communications tester CMW500. This information was not transmitted directly from these antennas to CMW500, but was relayed over a horn antenna that had a wired connection to CMW500. This horn antenna was placed on the back seat of the car.

Coming to the rest of the measurement set-up outside the car, we can see two vertically polarized double-ridged horn antennas, Tx1 and Tx2, located at 45 degrees

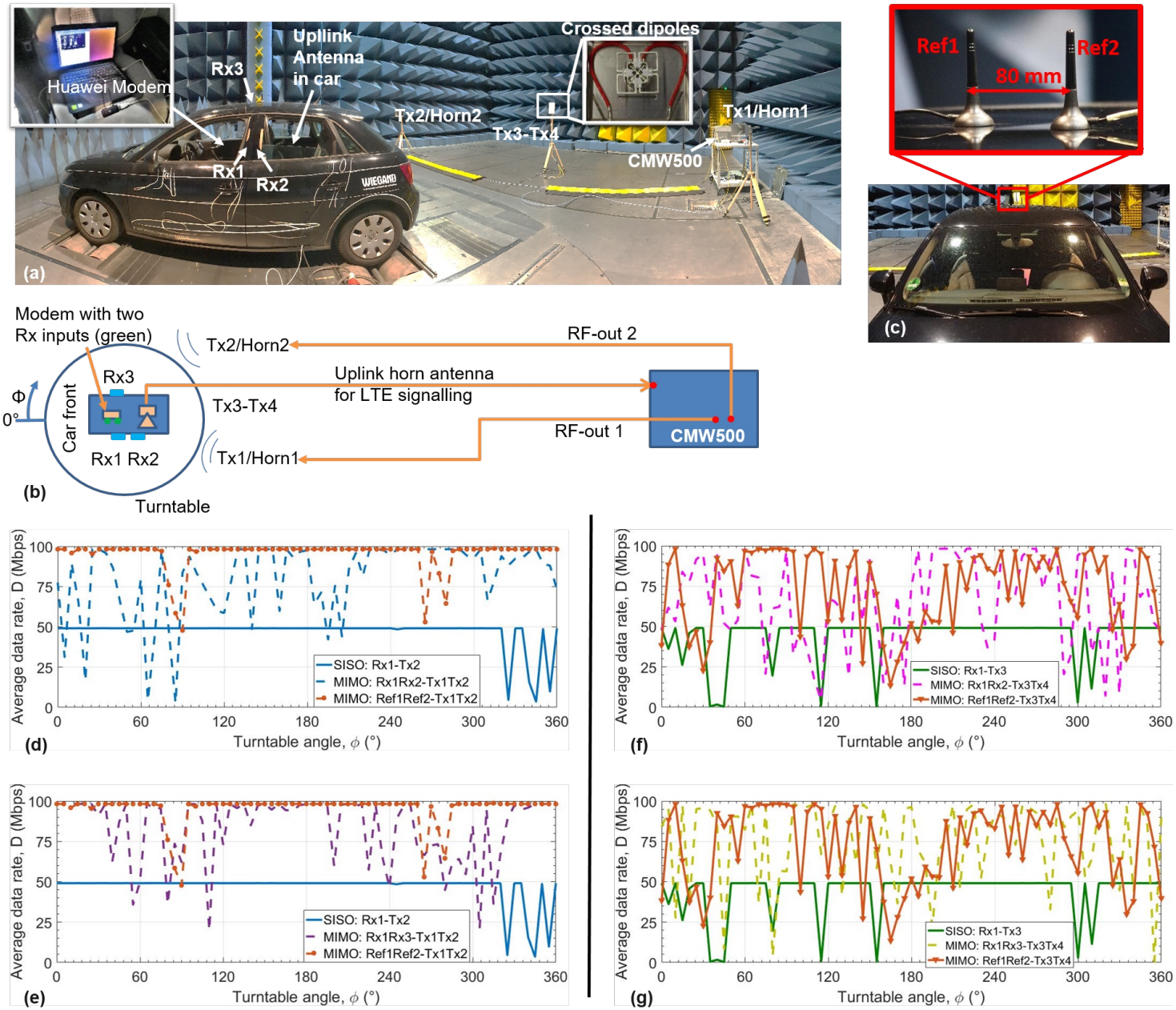

FIGURE 6.3: (a) Measurement setup indicationg the location of the embedded antennas, Rx1, Rx2, Rx3, the tranmitting antennas, Tx1...Tx4, and CMW500, (b) Schematic of the measurement setup indicating the various connections. (c) A pair of reference monopoles on the car rooftop. (d), (e) Downlink SISO and MIMO data rate comparison with Tx1/Tx2 horn antennas as transmitters. (f), (g) Downlink SISO and MIMO data rate comparison with Tx3/Tx4 crossed dipoles as transmitters.

to the centre of the turntable on either side of it. Furthermore, there was an LTE mobile base station crossed-dipole antenna pair, labelled Tx3 and Tx4, positioned at 0 degrees to the centre of the turntable. All of the Tx antennas were approximately at a 5 m distance from the turntable centre and at a height of roughly 1.6 m from the ground. At the back of the picture, on the right hand side, one can notice CMW500, to which the Tx antennas were connected in pairs at a time. CMW500 can generate LTE signals in various transmission modes, numbered through TM1...TM10 in release 12 (refer [117] for a description of each mode) . The modes that were used for the measurements considered here were the the TM1 mode and the TM4 mode. TM1 mode corresponds to the usage of a single transmit antenna, and using a single receive antenna on the car, this mode was able to deliver the SISO data rate. TM4 mode denotes closed loop spatial multiplexing on 2 transmit antennas, which made it suitable for measuring the downlink MIMO data rate with 2 receive antennas connected to the Huawei modem at the car. Furthermore, CMW500 allows for the selection of the modulation scheme, and it was set to 16-QAM. Therefore, it was known that the peak SISO data rate would be roughly 50 Mbps, for 20 MHz channel bandwidth, as per the calculation procedure in the previous section. Consequently, the peak 2x2 MIMO data rate would be around 100 Mbps.

Downlink data rate was measured with different combinations of Rx antennas on the car and Tx antennas outside the car in distinct measurements, without altering the measurement set-up in any way, except for changing the antenna connections to the Huawei modem and CMW500. Consider the measurement procedure for the Rx1/Rx2 antenna combination:

1. The Rx1 and Rx2 antennas were connected to the Huawei modem, whereas the Tx1 and Tx2 antennas were connected to CMW500.

2. The transmission mode of CMW500 was set to TM4 for closed loop MIMO operation.

3. The transmit power per LTE resource element was set to the maximum value of -32.8 dBm at CMW500.

4. The turntable was rotated 360 degrees in 73 steps of 5 degrees each. At each step, the downlink data rate was recorded for 10 seconds by iperf. The data rate was averaged over 10 seconds for each turntable step in post processing.

5. Tx1 and Tx2 antennas were disconnected from CMW500, and Tx3 and Tx4 antennas were connected instead. Step 4 was repeated.

The entire procedure above was repeated for the Rx1/Rx3 and Ref1/Ref2 antenna combinations. The downlink SISO data rate was also measured similarly with the Rx1 antenna, once with Tx1 as the transmit antenna, and then with Tx3 as the transmit antenna, after switching CMW500 to TM1 transmission mode. It is important to note that as the measured data rate is influenced by multipath propagation, changes in the measurement environment lead to changes in the multipath behaviour, and as a consequence in the measured data rate. Therefore, the VISTA measurement results apply to the set-up under consideration. It is also for the same reason that the data rate varies over time in the field tests discussed later. As the car moves on the road, the multipath behaviour changes in accordance with the surrounding environment.

The measurement results are presented in Fig. 6.3 (d)...(g). Consider first the parts (d) and (e). These represent the measurements with the horn antennas Tx1 and

Tx2 as the transmit antennas. The SISO data rate (blue curve) was 50 Mbps over nearly the entire 360° range, except at a few points towards the end. The orange dotted curve in both (d) and (e) indicates the downlink MIMO data rate achieved with the Ref1/Ref2 antenna combination at the car; we can see that leaving aside a few points in 60...120° and the 240...300° range, it was around 100 Mbps over the 360° turntable rotation. In comparison to the orange dotted curve, the blue dashed curve in part (d) shows the MIMO performance of the Rx1/Rx2 antenna combination at the car. Similarly, the violet dashed curve in part (e) presents the MIMO performance of the Rx1/Rx3 antenna combination at the car. It can be seen that in both the cases, the rooftop monopoles, i.e., the Ref1/Ref2 combination performs better. One of the reasons for this performance difference is contained in the radiation patterns of these antennas, as depicted earlier in Fig. 6.1. The Rx1/Rx2 combination radiates primarily towards the left side of the car, the Rx1/Rx3 combination radiates both on the left and right sides, which is better than the former situation. But in both the cases, a null exists along the driving direction. This is not true for the rooftop monopoles; these radiate omnidirectionally in the horizontal plane, therefore have a better coverage and achieve a better data rate. Another important fact is that depending upon the angle of rotation, either the antenna(s) in the left plastic cover(s) or the one in the right plastic cover is shadowed by the body of the car, whereas no such shadowing problem exists for the rooftop monopoles.

Let us now move onto the parts (f) and (g) in Fig. 6.3. The difference here is that the cross-polarized dipole antennas, Tx3 and Tx4, were used as the transmit antennas. The green curve in both the parts shows the downlink SISO data rate measured with Rx1 at the car and Tx3, the -45° oriented dipole of the crossed dipole pair, at CMW500. Once again, 49 Mbps was achieved at a majority of the points, although the performance was slightly worse compared to the SISO data rate measurement with the Tx2 antenna in the previous case. The orange curves in (f) and (g) represents the MIMO data rate achieved with the Ref1/Ref2 antenna combination on the roof of the car. In comparison, the pink dashed curve in (f) and light green dashed curve in (g) depict the MIMO data rate obtained with the Rx1/Rx2 and the Rx1/Rx3 antenna combination, respectively. The difference between the MIMO performance of the rooftop monopoles and the embedded antennas is not so evident, as it was in parts (d) and (e). As a whole, the MIMO data rate was also less consistently close to 100 Mbps as opposed to in parts (d) and (e). This could simply be due to the polarisation mismatch between the crossed dipole antennas and the vertically polarized rooftop monopoles and embedded antennas.

In all cases, Fig. 6.3 (d)...(g), the MIMO data rate fell below the SISO data rate at some of the measured points. Ideally, MIMO data rate should be > SISO data rate. In closed loop operation, the transmitter is capable of adjusting the transmit mode depending upon the channel condition information contained in the feedback loop from the receiver. So, for example, if the channel does not offer rich multipath conditions, the transmitter could switch to a transmit diversity mode or a SISO mode to ensure that data is transmitted reliably at a speed no less than what a SISO connection would offer under the same conditions. Although CMW500 was operated in closed loop configuration, it remained operational in the initially set TM4 MIMO mode irrespective of information provided to it by the feedback path. At some measurement points, operation in the MIMO mode may not have been suitable, and at these points the MIMO data rate fell below the SISO data rate.

For a deeper insight into the measurement data discussed above, consider the plots presented in Fig. 6.4 (a) and (b). As mentioned earlier, the turntable was rotated through 360° in 73 steps of 5° each. P represents the percentage of steps at which the

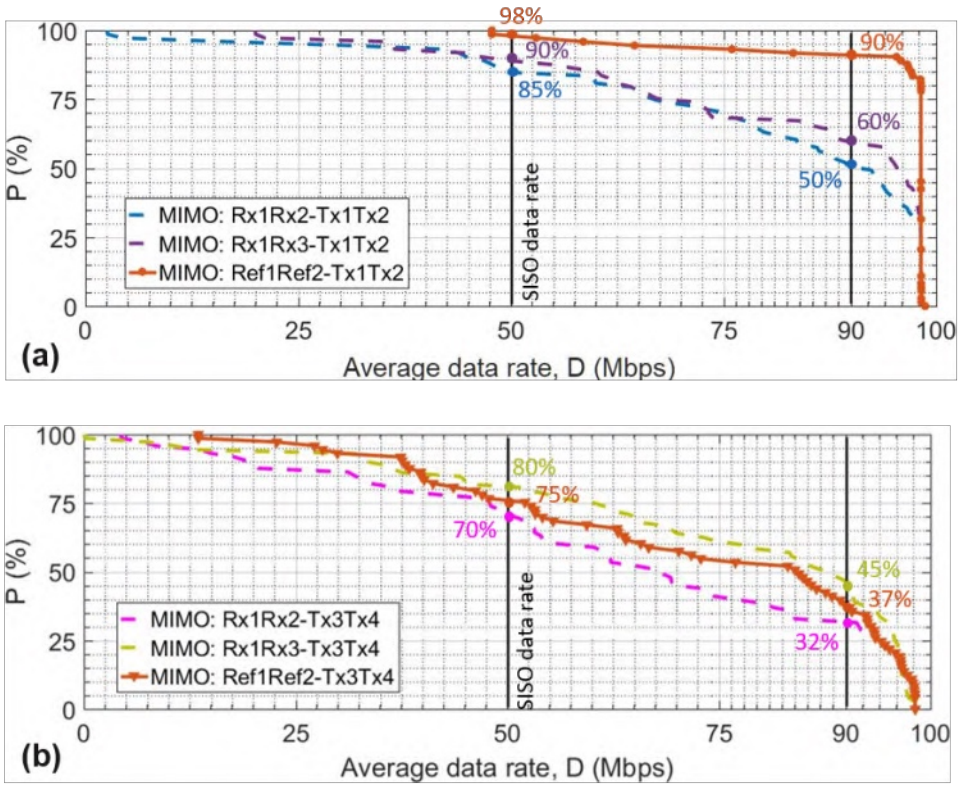

FIGURE 6.4: Curves indicating the percentage of measured data points with data rate $\geq$ to the values along the x-axis with: (a) Tx1/Tx2 horn antennas as transmitters, and (b) Tx3/Tx4 crossed dipoles as transmitters. More details in the text.

measure data rate D was $\geq$ the values contained in the X-axis of the graph. Part (a) compares P with Tx1 and Tx2 horn antennas as the transmit antennas. The percentage of points above the SISO data rate and above 90 Mbps has been indicated in each case. Ref1/Ref2 antenna combination performs the best, and between the Rx1/Rx2 and the Rx1/Rx3 combinations, the latter performs slightly better. The reason that the Rx1/Rx3 combination performed slightly better than the Rx1/Rx2 combination, but worse than the Ref1/Ref2 combination has been elucidated earlier based upon the radiation pattern differences of these combinations. As the 2 x 2 MIMO data rate cannot be more than twice the SISO data rate, the curves drop off sharply right before the 100 Mbps point on the x-axis. Part (b) illustrates P with Tx3 and Tx4 crossed dipole antennas as the transmit antennas. One can clearly see here that the performance difference between the Ref1/Ref2 combination and the embedded antenna combinations is not so distinct as in Fig. 6.4 (a). The Rx1/Rx3 in fact performs slightly better than the Ref1/Ref2 combination. In any case, this measurement with the crossed dipole antennas as transmitters is of more practical importance than the measurement with the horn antennas as transmitters, as mobile base stations typically comprise crossed dipole antennas (for keeping the array compact [117]). A lack of major performance difference between the Ref1/Ref2 and Rx1/Rx3 combinations in relation to the crossed dipole antennas as transmitters is certainly interesting to see here.

The company Antennentechnik Bad Blankenburg [118] conducted a field test with the Rx1/Rx3 antenna combination in place, and compared the MIMO data rate performance of this combination with the SISO data rate obtained with a rooftop

monopole antenna. They took a total of 30 SISO (with the rooftop monopole) and 30 MIMO (with the B-column antennas) data rate measurements in pairs on the same day in rural and urban environments in and around the city of Weimar. Each SISO and MIMO data rate measurement within a pair was conducted simultaneously so that both these measurements experienced the same channel conditions, but at the same time each pair of these measurements was taken at a different time within the time window of ap-proximately 08:30 am to 03:00 pm. This allowed to additionally take into account the different network load conditions at different times of the day. Snapshots from the field test are shown in Fig. 6.5 (a) and (b). Inside the car, the setup was similar to that in VISTA: There was an LTE modem to which the rooftop monopole and the Rx1/Rx3 antennas could be connected. The modem was connected to a laptop with an RJ-45 interface, and the laptop was running a suitable program to record the data rate. The measurement result is presented in Fig. 6.5 (c). On an average, the MIMO data rate with the Rx1/Rx3 combination was 1.6 times higher than the SISO data rate with the rooftop monopole. A subsequent field test on the same route was done by the same company, wherein the MIMO performance of a pair of rooftop monpoles was compared to the SISO performance of a rooftop monopole. Here also it was found that on an average the MIMO data rate with rooftop monopoles was 1.6 times higher than the SISO data rate with a single rooftop monopole. Granted that the channel conditions may have been different during these two sets of measurements, but considered as a whole with the VISTA measurements with the crossed dipole base station antennas as transmitters (Fig. 6.4 (b)), the argument is bolstered that there is no significant difference between the MIMO performance of the Rx1/Rx3 combination and the rooftop monopole antenna pair with the bas station antennas as transmitters.

A few more observations can be made looking at Fig. 6.5 (c):

1. The MIMO data rate remained comparable to the SISO data rate in the least multipath rich conditions that arose during the rural stretches of the field test. This means that the base station had actually switched from the MIMO mode to a transmit diversity or SISO mode at these points, unlike in the VISTA measurements where CMW500 never made any switch between the modes to account for the deteriorating multipath situations.

2. This observation is contained in the first one, that the MIMO performance degrades in the rural areas, the most likely reason for this being the decline in multipath richness in these areas. Although not directly comparable to the Bad Blankenburg field tests, [119] shows that the multipath richness indeed declines in rural areas as measured through a corresponding increase in the Rician factor. These authors conducted V2V field tests, and computed the probability density functions for the Rician factor in urban, suburban, and rural environments. They found out that for urban areas most of the Rician factor values lay between -7...+10 dB, with the average value being 1.8 dB, whereas in rural areas, most of the Rician factor values were concentrated between +2...+7 dB, with the average value being 3 dB. Therefore, on an average, Rician factor is higher in rural areas than urban areas, in other words, the direct signal path carries more power than the combination of scattered paths in rural environments. Thus it can be expected that MIMO performance degrades in rural areas.

3. The peak MIMO data rate in urban conditions was not always twice the corresponding SISO data rate. This is because the data rate for a given channel

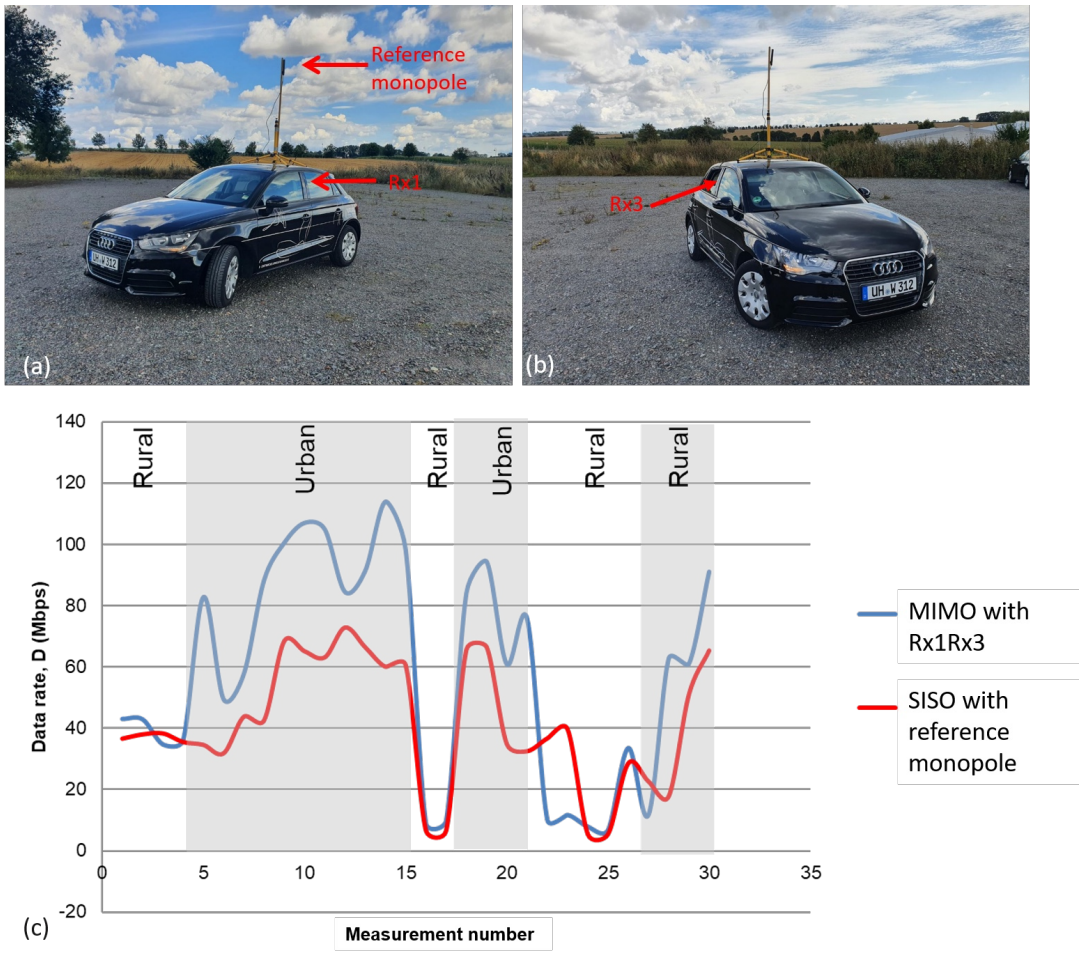

FIGURE 6.5: (a),(b) Snapshots from the field tests indicating the reference monopole antenna, and the embedded Rx1/Rx3 antennas. (c) Measured peak data rate against the measurement number.

bandwidth not only depends upon the selected modulation scheme, but also on the coding rate selected based upon the CQI value fed back by the receiver to the base station. A coding rate below 1 implies that the achieved data rate will be below the maximum possible data rate for a given modulation scheme and channel bandwidth combination.

6.4 V2V communications field tests

As mentioned earlier in chapter 2, V2V communication is quickly gaining traction due to the passenger safety and traffic optimization benefits it offers. We saw that for the purpose of LTE mobile communications, B-column mounted antennas performed similarly to the car rooftop monopole antennas, in terms of the measured data rates. Therefore, the question arose if the V2V communications performance of the plastic cover embedded antennas would compare to that offered by rooftop mounted monopole antennas. The performance metrics for V2V communication are packet delivery ratio (PDR), which is the ratio of packets received to the total number of packets transmitted within a set time interval which was 1 second in our case, and received power, P_{Rx}. High data rates like for LTE are not important as the packets in V2V communication are just a few bytes in size.

V2V communication field tests were conducted in the later half of 2020 to evaluate the performance of the B-column antennas and have been comprehensively reported in [120]. Concisely, the main findings of this pioneering work were: (i) For relative distances <300 m between the transmitter car and the receiver car, there was no remarkable performance difference between the rooftop monopoles and the front-left and front-right B-column antenna combination, (ii) For relative distances $\geq$ 300 m, the rooftop monopoles performed better, before these also reached the -95 dBm receiver sensitivity limit at distances upwards of 500 m. On an average, the PDR and P_{RX} of the rooftop monopoles were respectively 8.8% and 8 dBm higher than for the front-left/front-right B-column antenna combination. These differences can be understood in terms of the gain pattern differences between the rooftop monopoles and the B-column antennas. Once again, there was a significant difference between the gains of the rooftop monopoles and the B-column antennas along the driving direction, with the monopoles having a 20 dB gain advantage along this direction. In the field tests, the Tx-car was following the Rx-car, and these were, every once in a while, travelling in a straight line. In such instances, the gain deficit of the B-column antennas along the driving direction leads to their reduced performance. But this does not imply the unsuitability of B-column antennas for V2V communication.

The important conclusion here is that as significant performance differences appear only above relative distances of 300 m, these would be inconsequential in the fu-ture. For the field tests under discussion, only our two cars were equipped with V2V communication hardware, whereas in the future, all cars are likely to be equipped with V2V hardware. This implies that within the 300 m gap there would most likely be other V2V capable cars forming a part of the ad-hoc communications network. Therefore, the V2V communications distances would realistically lie below 300 m, in which case the B-column antennas are as good as the rooftop monopole antennas.

Chapter 7

Conclusion and outlook

The preceding pages presented several interesting mobile communication antenna designs, their theoretical backgrounds, simulations, and measurements including field tests. As outlined at the beginning of this work, the principal design challenge was the close proximity of the antennas to the metallic chassis, as well as the low integration space in the plastic cover. The di-patch, the multiband patch, and the HIS-dipole were able to surmount these challenges and deliver a better performance over typical patch antennas in terms of an improved impedance bandwidth in general, and additionally a lower total occupied surface area in the case of the di-patch antenna. Furthermore, in the last chapter concerning the LTE MIMO data rate performance tests, the performance of the plastic embedded antennas was found to be comparable to the rooftop monopole antennas. Although these antennas were designed targeting the goals of KUBINKA, there is nothing restricting their application only to the scope of this project. In a general sense, these antennas form worthy candidates for usage in other applications as well, where the proximity of the antenna to an underlying metal surface presents a design challenge.

Several things can be imagined in terms of the future work, as enlisted below in no specific order:

1. Till now HIS was combined with a typical half-wavelength dipole antenna. It would be interesting to thoroughly study the interaction of a di-patch antenna with a HIS, to ascertain if it offers any advantages over the aforementioned typical combination.

2. If it would be possible to obtain an even more wideband or multiband behaviour from the di-patch antenna through additional parasitic / directly connected patches, modifications to the shape of the di-patch, and/or cutting out slots at suitable locations on the patches.

3. The di-patch antenna arose from the observation that at the second harmonic resonance, the input impedance of a dipole antenna is very high closely above a ground plane. Suitable manipulations were made to the dimensions of the dipole antenna, the feeding point adjusted, and the input impedance could be brought down to 50 Ω. This was an exercise from an engineering point of view. It would be fascinating as well to explain the interaction of the second harmonic mode with the ground plane from a more theoretical or physics point of view.

4. Horizontal stacking was used for designing the multiband patch antenna in chapter 4, as sufficient vertical integration space was available in the plastic cover and also because the resulting two-layer antenna design would be simple enough to be milled in our own lab. However, ample vertical space may not always be available. In such a case, it should be possible to stack the

parasitic patches vertically. The would reduce the antenna size along the vertical dimension while, in principle, maintaining the same multiband behaviour.

5. Going from the bare antenna to the partial door frame and subsequently to the entire car, at each step there is a reduction in the antenna efficiency. Of course, as mentioned in the text, the losses increase due to the introduction of dielectrics, including the plastic covers, the surrounding rubber, the glass windows and the car paint, as well as the finite conductivity of the car metal. An even finer multi-step measurement procedure to isolate the losses contributed by each of these things would further help increase our understanding of the interaction of the antenna with the car. It could be like this: After the bare antenna measurement, measure the plastic cover alone, then together with the partial door frame. This would quantify the loss contributed by the plastic cover in the first step, and the total increase in losses with the introduction of the door frame. Then the door frame could be measured once with the rubber parts, once unpainted, and so on to decompose additional losses offered by the door frame into their constituent parts.

6. Even with the B-column antennas on the left and the right sides of the car, there would always be a null along the driving direction, in other words, the coverage would not be truly omnidirectional in the horizontal plane. To enhance the communication performance, suitable places should be found at the front and back of the car to embed antennas covering the same frequencies. This would especially be helpful for V2V communications, where a lot of information is exchanged between the cars along the driving direction.

7. Another approach pertaining to point 6 would be to just have the antennas inside the left and right side covers of the car, but to design these antennas such that the radiation pattern of the left cover antenna spills over a little bit to the front of the car, and the radiation pattern of the right cover antenna spills over a bit to the back of the car. Such a thing could probably be achieved by weighting the field distribution on these antennas appropriately and/or by cutting out portions of the PCB ground plane not directly below the antenna elements. If possible, such a procedure would achieve omnidirec-tionality without the need for additional antennas at the front and back of the car.

Appendix A

Mutual impedance between half-wave folded dipole antennas

The authors in [73] derive the mutual impedance between two folded dipole antennas, with $N = 2$, where N represents the number of arms in each folded dipole. The derivation would be concisely presented here, and subsequently it will be shown that the result can be easily generalized to determine the mutual impedance between two N-arm folded dipole antennas.

Consider Fig. A.1 (a), wherein a half-wavelength dipole (antenna 1) and a 2 arm folded dipole (antenna 2) are at a distance d from each other, and are oriented along the Z-axis. Radiation from antenna 1 induces a voltage V_{21F} at the terminals of antenna 2, which may be given as:

$$V_{21F} = -\frac{1}{I_2}\int_{-L_2/2}^{L_2/2} E_{z21}\,(z)\,I_2\,(z)\,dz \tag{A.1}$$

where I_2 is the current at the input terminals of antenna 2, E_{z21} is the electric field component in the Z-direction at antenna 2 due to antenna 1, and $I_2\,(z)$ is the current distribution along antenna 2.

The mutual impedance at the port of antenna 2 referred to the current I_1 at the input of antenna 1 is then defined as:

$$Z_{21F} = \frac{V_{21F}}{I_1} = -\frac{1}{I_1 I_2}\int_{-L_2/2}^{L_2/2} E_{z21}\,(z)\,I_2\,(z)\,dz \tag{A.2}$$

The current $I_2\,(z)$ along antenna 2 comprises a combination of two types of current flow: (i) The transmission line mode currents that flow in equal amplitude

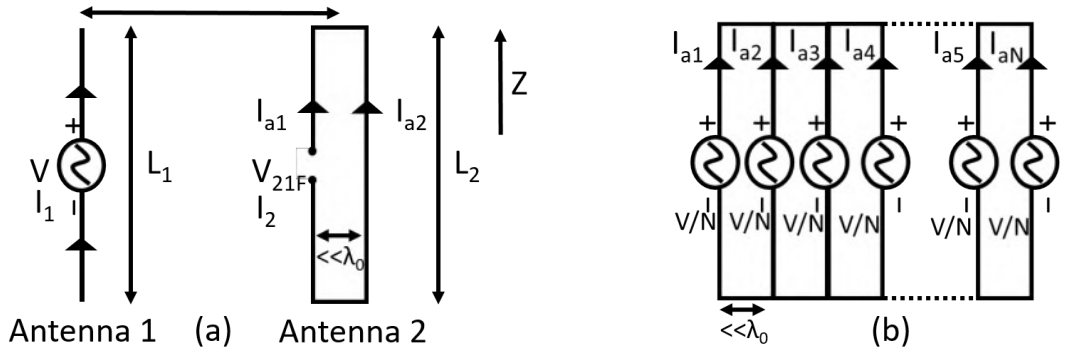

FIGURE A.1: (a) A typical dipole and a folded dipole at a distance d from each other. (b) Equivalent model of an N-arm folded dipole antenna showing the antenna mode currents.

The current $I_2(z)$ along antenna 2 comprises a combination of two types of current flow: (i) The transmission line mode currents that flow in equal amplitude and opposite phase along the two arms. Since the two arms are at a negligible distance from each other, the electric fields generated by these currents cancel out, and have no contribution to the mutual impedance, (ii) The antenna mode currents I_{a1} and I_{a2}, on the other hand, are excited with the same phase and amplitude. Therefore, one can consider the folded dipole arms as being collapsed to a filamentary current of value $2 \times I_{a1}$, following which the effective current in the second antenna as a whole is:

$$I_2(z) = I_{a1}(z) + I_{a2}(z) = 2 \cdot I_{a1} = 2 \cdot I_{2m} \sin \left[k \left(\frac{L_2}{2} - |z| \right) \right] \tag{A.3}$$

where I_{2m} is the maximum current each of the two arms of antenna 2. Sinusoidal distribution for $I_2(z)$ of course assumes that the radius of the antenna wire is far smaller that the considered wavelength. Substituting the expression for E_{z21} and equation (A.3) into equation (A.2) gives:

$$\begin{aligned} Z_{21F} = \frac{V_{21F}}{I_1} = 2 \cdot j \, \frac{\eta I_{1m} I_{2m}}{4\pi I_1 I_2} \int_{-L_2/2}^{L_2/2} \sin \left[k \left(\frac{L_2}{2} - |z| \right) \right] \left[\frac{e^{-jkR_1}}{R_1} \right. \\ \left. + \frac{e^{-jkR_2}}{R_2} - 2 \cos \left(k \frac{L_1}{2} \right) \frac{e^{-jkr}}{r} \right] dz \end{aligned} \tag{A.4}$$

where I_{1m} is the maximum current for antenna 1. The meanings of other terms can be found in [73]. The expression following the factor of 2 in equation (A.4) is the standard expression for the mutual impedance between two typical half-wavelength dipole antennas, and may simply be denoted as Z_{21}. Therefore,

$$Z_{21F} = Z_{dipole\ to\ folded\ dipole} = 2 \cdot Z_{21} \tag{A.5}$$

Following the principle of reciprocity,

$$Z_{folded\ dipole\ to\ dipole} = 2 \cdot Z_{21} \tag{A.6}$$

Therefore,

$$Z_{folded\ dipole\ to\ folded\ dipole} = 2 \cdot (2 \cdot Z_{21}) \tag{A.7}$$

Generalization: The equivalent model of an N-arm folded dipole antenna indicating the antenna mode currents is shown in Fig. A.1 (b). Given the wire radius and overall width of the antenna are negligible, $I_{a1}(z) = I_{a2}(z) = \ldots = I_{aN}(z) = I_m \sin \left[k \left(\frac{L_2}{2} - |z| \right) \right]$. If this antenna were antenna 2 in Fig. A.1 (a), then the multiplying factor in equation (A.3) and subsequently equation (A.4) would be N instead of 2. Following the same arguments thereafter, this would lead to the generalized result:

$$Z_{folded\ dipole\ to\ folded\ dipole} = N \cdot (NZ_{21}) = N^2 \cdot Z_{21} \tag{A.8}$$

Appendix B

Bibliography

[1] McKinsey & Company, "Competing for the connected customer – perspectives on the opportunities created by car connectivity and automation," Tech. Rep., 2015.

[2] GSMA, "2025 every car connected: Forecasting the growth and opportunity," GSM Association, Tech. Rep., 2012.

[3] 5GAA Distributed vehicular antenna system. [online]. Available: https://5gaa.org/wp-content/uploads/2022/01/5GAA_Distributed_vehicular_antenna%C2%AD_system_TR.pdf, accessed: 12 June 2022.

[4] E. Safin, R. Valkonen and D. Manteuffel, "Reconfigurable LTE MIMO automotive antenna system based on the characteristic mode analysis," *2015 9th European Conference on Antennas and Propagation (EuCAP)*, Lisbon, 2015, pp. 1-3.

[5] E. Condo Neira, J. Carlsson, K. Karlsson and E. G. Ström, "Combined LTE and IEEE 802.11p antenna for vehicular applications," 2015 9th European Conference on Antennas and Propagation (EuCAP), Lisbon, 2015, pp. 1-5.

[6] S. Hasturkoglu and S. Lindenmeier, "A wideband automotive antenna for actual and future mobile communication 5G/LTE/WLAN with low profile," 2017 11th European Conference on Antennas and Propagation (EUCAP), Paris, 2017, pp. 602-605, doi: 10.23919/EuCAP.2017.7928669.

[7] J. H. Lee, S. H. Lee, D. Kim, and C. W. Jung, "Transparent antenna using a μ-metal mesh on the quarter glasses of an automotive for DMB service receiving," *Microw. Opt. Technol. Lett.*, vol. 60, no. 12, pp. 3009-3014, 2018.

[8] J. H. Lee, S. H. Lee, D. Kim, and C. W. Jung, "Transparent dual-band monopole antenna using a μ-metal mesh on the rear glass of an automobile for frequency modulation/digital media broadcasting service receiving," *Microw. Opt. Technol. Lett.*, vol. 61, no. 2, pp. 503-508, 2019.

[9] Victor Rabinovich, Nikolai Alexandrov and Basim Alkhateeb, "Audio broadcasting antennas", in *Automotive Antenna Design and Applications*, 1^{st} ed., CRC Press, 2010, ch. 4, pp. 63-103.

[10] H. Toriyama, J. Ohe, H. Kondo and H. Yotsuya, "Development of printed-on glass TV antenna system for car," *37th IEEE Vehicular Technology Conference*, Tampa, Florida, USA, 1987, pp. 334-342, doi: 10.1109/VTC.1987.1623567.

[11] M. Brzeska et al., "New generation of in-mirror integrated antennas," *2009 3rd European Conference on Antennas and Propagation*, Berlin, 2009, pp. 2704-2707.

[12] Min-Seong Kim, Kyeong-Sik Min and D. Park, "Directivity Design of RFID Tag Antenna Using Side-view Mirror for Vehicle," *2008 Asia-Pacific Microwave Conference*, Macau, 2008, pp. 1-4, doi: 10.1109/APMC.2008.4957980.

[13] W. Menzel and A. Moebius, "Antenna Concepts for Millimeter-Wave Automotive Radar Sensors," in *Proceedings of the IEEE*, vol. 100, no. 7, pp. 2372-2379, July 2012, doi: 10.1109/JPROC.2012.2184729.

[14] J. Dickmann et al., "Making Bertha See Even More: Radar Contribution," in *IEEE Access*, vol. 3, pp. 1233-1247, 2015, doi: 10.1109/ACCESS.2015.2454533.

[15] R. J. Marhefka, B. A. Baertlein, M. Rao and K. Prakah-Asante, "Modeling the performance of automotive bumper mounted antennas," *IEEE Antennas and Propagation Society International Symposium (IEEE Cat. No.02CH37313)*, San Antonio, TX, USA, 2002, pp. 316-319 vol.3, doi: 10.1109/APS.2002.1018218.

[16] Y. Liu, Z. Ai, G. Liu and Y. Jia, "An Integrated Shark-Fin Antenna for MIMO-LTE, FM, and GPS Applications," in *IEEE Antennas and Wireless Propagation Letters*, vol. 18, no. 8, pp. 1666-1670, Aug. 2019, doi: 10.1109/LAWP.2019.2927019.

[17] C. Demien and R. Sarkis, "Design of Shark Fin Integrated Antenna Systems for Automotive Applications," *2019 Photonics & Electromagnetics Research Symposium - Spring (PIERS-Spring)*, Rome, Italy, 2019, pp. 620-627, doi: 10.1109/PIERS-Spring46901.2019.9017479.

[18] O. Kwon, R. Song and B. Kim, "A Fully Integrated Shark-Fin Antenna for MIMO-LTE, GPS, WLAN, and WAVE Applications," in *IEEE Antennas and Wireless Propagation Letters*, vol. 17, no. 4, pp. 600-603, April 2018, doi: 10.1109/LAWP.2018.2805681.

[19] Juha Korhonen, "History of mobile telecommunications", in *Introduction to 4G Mobile Communications*, 1st ed., Artech House, 2014, ch. 2, pp. 5-28.

[20] ETSI, "Digital cellular telecommunications system (phase 2+); GSM release 1999 specifications," European Telecommunications Standards Institute, Sophia Antipolis, France, ETSI TS 101 805, 1999. 28

[21] M. Sauter, *Communication Systems for the Mobile Information Society*, Wiley, 2006.

[22] 3GPP, "Requirements for the UMTS terrestrial radio access (UTRA) system," 3rd Generation Partnership Project, Sophia Antipolis, France, 3GPP TS 21.01U, 1997.

[23] Y. Zaki, *Future Mobile Communications: LTE Optimization and Mobile Network Virtualization*, ser. Advanced Studies Mobile Research Center Bremen. Springer Fachmedien Wiesbaden, 2012.

[24] 3GPP, "Evolved universal terrestrial radio access (E-UTRA); user equipment (UE) radio transmission and reception," 3rd Generation Partnership Project, Sophia Antipolis, France, 3GPP TS 36.101, 2015.

[25] S. K. Datta, R. P. F. Da Costa, J. Härri and C. Bonnet, "Integrating connected vehicles in Internet of Things ecosystems: Challenges and solutions," *2016 IEEE 17th International Symposium on A World of Wireless, Mobile and Multimedia Networks (WoWMoM)*, 2016, pp. 1-6, doi: 10.1109/WoWMoM.2016.7523574.

[26] R. Hussain and S. Zeadally, "Autonomous Cars: Research Results, Issues, and Future Challenges," in *IEEE Communications Surveys & Tutorials*, vol. 21, no. 2, pp. 1275-1313, Secondquarter 2019, doi: 10.1109/COMST.2018.2869360.

[27] H. Inoue, "Research into ADAS with driving intelligence for future innovation," *2014 IEEE International Electron Devices Meeting*, 2014, pp. 1.3.1-1.3.7, doi: 10.1109/IEDM.2014.7046962.

[28] Etsi. "302 663 (V1. 2.1)(11-2012):" Intelligent Transport Systems (ITS)". In: *Access layer specification for Intelligent Transport Systems operating in the 5 GHz frequency band* 5.

[29] "IEEE Standard for Information technology– Local and metropolitan area networks– Specific requirements– Part 11: Wireless LAN Medium Access Control (MAC) and Physical Layer (PHY) Specifications Amendment 6: Wireless Access in Vehicular Environments". In: *IEEE Std 802.11p-2010 (Amendment to IEEE Std 802.11-2007 as amended by IEEE Std 802.11k-2008, IEEE Std 802.11r-2008, IEEE Std 802.11y2008, IEEE Std 802.11n-2009, and IEEE Std 802.11w-2009)* (July 2010), pp. 1-51.

[30] *3GPP TS 36.300, v 14.4.0, Technical Specification Group Radio Access Network; Evolved Universal Terrestrial Radio Access (E-UTRA and Evolved Terrestrial Radio Access Network (E-UTRAN)*. url: https://www.3gpp.org/release-14.

[31] *3GPP TR 36.213 v15.3.0, "Technical specification Group Radio Access Network. Evolved Universal Terrestrial Radio Access (E-UTRA); Physical layer procedures, Rel. 15"*. url: https://www.3gpp.org release-15.

[32] U. Tayyab, A. Kumar, Y. Li, R. Stephan, M. A. Hein and J. Singh, "Plastic-embedded Patch Antenna Array for Automotive Satellite Communication in the Ka-band," *2021 1st International Conference on Microwave, Antennas & Circuits (ICMAC)*, 2021, pp. 1-4, doi: 10.1109/ICMAC54080.2021.9678254.

[33] B. Evans, O. Onireti, T. Spathopoulos and M. A. Imran, "The role of satellites in 5G," 2015 *23rd European Signal Processing Conference (EUSIPCO)*, 2015, pp. 2756-2760, doi: 10.1109/EUSIPCO.2015.7362886.

[34] M. E. Asghar, F. Wollenschläger, A. Asgharzadeh, J. Singh and M. A. Hein, "Influence of antenna mounting location on the radiation pattern of an automotive antenna," *12th European Conference on Antennas and Propagation (EuCAP 2018)*, London, 2018, pp. 1-5, doi: 10.1049/cp.2018.1000.

[35] Warren L. Stutzman and Gary A. Thiele, "Low-profile antennas and personal communication antennas", in *Antenna Theory and Design*, 3^{rd} ed., Wiley, 2012, ch. 11, pp. 502-503.

[36] *"CST Studio Suite"*. Accessed on: March 27, 2022. [Online]. Available: https://www.3ds.com/products-services/simulia/products/cst-studio-suite/

[37] *"Ansys HFSS"*. Accessed on: March 27, 2022. [online]. Available: https://www.ansys.com/products/electronics/ansys-hfss

[38] *"Altair Feko"*. Accessed on: March 27, 2022. [online]. Available: https://altair.com/feko

[39] T. Weiland, M. Timm and I. Munteanu, "A practical guide to 3-D simulation," in *IEEE Microwave Magazine*, vol. 9, no. 6, pp. 62-75, December 2008, doi: 10.1109/MMM.2008.929772.

[40] David B. Davidson, "An overview of computational electromagnetics for RF and microwave applications", in *Computational Electromagnetics for RF and Microwave Engineering*, 2nd edition, New York: Cambridge, 2011.

[41] J. Singh, A. Asgharzadeh, R. Stephan and M. A. Hein, "Influence of Car Body Modeling on the Gain Patterns of Automotive Antennas," *2017 IEEE 85th Vehicular Technology Conference (VTC Spring)*, 2017, pp. 1-5, doi: 10.1109/VTC-Spring.2017.8108214.

[42] S. Imai, K. Taguchi, T. Kashiwa and T. Kawamura, "Effects of car body on radiation pattern of car antenna mounted on side mirror for inter-vehicle communications," 2014 IEEE Antennas and Propagation Society International Symposium (APSURSI), 2014, pp. 601-602, doi: 10.1109/APS.2014.6904631.

[43] Muhammad Ehtisham Asghar, "Antenna Measurement Data Analysis", Master Thesis, RF and Microwave Research Group, TU Ilmenau, 2016.

[44] Sunita Silwal, "Comparative Analysis of different Antenna Measurement Facilities", Master Thesis, RF and Microwave Research Group, TU Ilmenau, 2017.

[45] P. Berlt, C. Bornkessel and M. Hein, "Over-the-air emulation of a two-path model for automotive LTE system performance testing," *2019 IEEE International Conference on Connected Vehicles and Expo (ICCVE)*, 2019, pp. 1-5, doi: 10.1109/ICCVE45908.2019.8965223.

[46] W. Hofmann, C. Bornkessel and M. A. Hein, "Influence of Electrically Large Structures on the EMC-Compliance of a Semi-Anechoic Chamber," *2018 IEEE MTT-S International Conference on Microwaves for Intelligent Mobility (ICMIM)*, 2018, pp. 1-4, doi: 10.1109/ICMIM.2018.8443499.

[47] M. E. Asghar, C. Bornkessel and M. A. Hein, "Experimental Determination of the Total Radiated Power of Automotive Antennas in the Installed State," *2020 14th European Conference on Antennas and Propagation (EuCAP)*, 2020, pp. 1-5, doi: 10.23919/EuCAP48036.2020.9135647.

[48] G. Deschamps and W. Sichak, "Microstrip microwave antennas", *Proc. 3rd Symp. USAF Antenna Research and Development Program*, Oct. 18-22, 1953.

[49] R. B. Waterhouse, "Introduction" in *Microstrip Patch Antennas: A Designer's Guide*, Boston, MA, USA:Springer, p. 9, 2003.

[50] Constantine A. Balanis, "Antennas", in *Antenna Theory Analysis and Design*, 3^{rd} ed., Wiley, 2005, ch. 1, p. 20.

[51] F. Kuo, H. Chou, H. Hsu, H. Chou and P. Nepa, "A Novel Dipole Antenna Design With an Over 100% Operational Bandwidth," in *IEEE Transactions on Antennas and Propagation*, vol. 58, no. 8, pp. 2737-2741, Aug. 2010, doi: 10.1109/TAP.2010.2050434.

[52] Constantine A. Balanis, "Microstrip Antennas", in *Antenna Theory Analysis and Design*, 3rd edition, John Wiley & Sons, 2005, ch. 14, pp. 826 - 842.

[53] "Strahlungselement", by J. Singh, M. A. Hein, R. Stephan. (2021, Oct. 28), Patent DE102017011225A1 [online]. Available: https://patents.google.com/patent/DE102017011225A1/de

[54] J. Singh, R. Stephan and M. A. Hein, "Low-Profile Wideband Differentially Fed Di-Patch Antenna Closely Above Metallic Ground", in *IEEE Antennas and Wireless Propagation Letters*, vol. 18, no. 5, pp. 976-980, May 2019, doi: 10.1109/LAWP.2019.2906825.

[55] J. Singh, A. Neumann, T. Wack, T. Koppe, R. Stephan and M. A. Hein, "Novel conformal automotive di-patch antenna verified through car door frame measurements", *IET Conference Proceedings*, Birmingham, November 2019, doi: 10.1049/cp.2019.0700.

[56] S. H. Idris and C. M. Hadzer, "Analysis of the radiation resistance and gain of a full-wave dipole," in *IEEE Antennas and Propagation Magazine*, vol. 36, no. 5, pp. 45-47, Oct. 1994, doi: 10.1109/74.334923.

[57] Constantine A. Balanis, "Integral Equations, Moment Method, and Self and Mutual Impedances", in *Antenna Theory Analysis and Design*, 3rd ed., Wiley, 2005, ch. 8, pp. 466-467.

[58] Yu-Mei Guo, Ying-Zeng Yin, Jing-Li Guo, Jin-Ping Ma and Hui-Li Zheng, "Wideband patch dipole antenna," 2005 IEEE Ant. and Propag. Soc. Intl. Symp., Washington, DC, 2005, pp. 561-564 vol. 2A.

[59] Jeong Il Kim, Byung Moo Lee and Young Joong Yoon, "Wideband printed dipole antenna for multiple wireless services," Proc. RAWCON 2001. 2001 IEEE Radio and Wireless Conf. (Cat.No.01EX514), Waltham, MA, USA, 2001, pp. 153-156.

[60] Z. N. Chen, Y. Juan, X. Qing and W. Che, "Enhanced radiation from a horizontal dipole closely placed above a PEC ground plane using a parasitic strip," in IEEE Trans. on Anten. and Propag., vol. 64, no. 11, pp. 4868-4871, Nov. 2016. doi: 10.1109/TAP.2016.2594842

[61] Full-wave di-patch antenna, by Michael Gregory Pettus. (2011, Jan. 11). US7868841B2 [Online]. Available: https://patents.google.com/patent/US7868841B2/en

[62] Antenna and electronic device equipped with the same, by Nagahisa Furutani, Manabu Kai and Satoru Nogami. (2013, Sep. 17). US8537052B2 [Online]. Available: https://patents.google.com/patent/US8537052B2/en

[63] Warren L. Stutzman and Gary A. Thiele, "Low-Profile Antennas and Personal Communication Antennas", in *Antenna Theory and Design*, 3rd ed., Wiley, 2013, ch. 11, pp. 470-471.

[64] Constantine A. Balanis, "Linear Wire Antennas", in *Antenna Theory Analysis and Design*, 3rd ed., Wiley, 2005, ch. 4, pp. 197-204.

[65] Warren L. Stutzman and Gary A. Thiele, "Simple Radiating Systems", in *Antenna Theory and Design*, 3rd ed., Wiley, 2013, ch. 3, pp. 76-78.

[66] Jiang-Ming Jin, "Electromagnetic Theorems and Principles", in *Theory and Computation of Electromagnetic Fields*, 2nd ed., Wiley, 2015, ch. 3, pp. 94.

[67] R. King and F. G. Blake, "The Self-Impedance of a Symmetrical Antenna," in Proceedings of the IRE, vol. 30, no. 7, pp. 335-349, July 1942, doi: 10.1109/JRPROC.1942.231332.

[68] G.H. Brown and Ronold King, "High-Frequency Models in Antenna Investigations", in *Proceedings of the Institute of Radio Engineers*, Volume 22, Number 4, April 1934.

[69] Ronold King and Charles W. Harrison, "Mutual and Self-Impedance tor Coupled Antennas", in *Journal of Applied Physics*, vol. 15, 1944.

[70] R. King and Tai Tsun Wu, "Currents, Charges, and Near Fields of Cylindrical Antennas", in *RADIO SCIENCE Journal of Research NBS/USNC-URSI*, Vol. 69D, No. 3, March 1965

[71] P. Hazdra, M. Capek, J. Eichler and M. Mazanek, "The Radiation Q-Factor of a Horizontal $\lambda/2$ Dipole Above Ground Plane," in *IEEE Antennas and Wireless Propagation Letters*, vol. 13, pp. 1073-1075, 2014, doi: 10.1109/LAWP.2014.2329421.

[72] Warren L. Stutzman and Gary A. Thiele, "Wire Antennas", in *Antenna Theory and Design*, 3^{rd} ed., Wiley, 2013, ch. 6, pp. 161-166.

[73] A. R. Clark and A. P. C. Fourie, "Mutual impedance and the folded dipole," *1994 Second International Conference on Computation in Electromagnetics*, 1994, pp. 347-350, doi: 10.1049/cp:19940088.

[74] Best, "Improving the performance properties of a dipole element closely spaced to a PEC ground plane," in *IEEE Ant. and Wireless Propag. Lett.*, vol. 3, pp. 359-363, 2004. doi: 10.1109/LAWP.2004.840722

[75] C. T. Tai, "Coupled Antennas", in *Proceedings of the I.R.E.*, 1948.

[76] David Middleton, Ronold King, "The thin cylindrical antenna: a comparison of theories"in *Journal of Applied Physics*, vol. 17, 1946, https://doi.org/10.1063/1.1707714

[77] C. Butler, "The equivalent radius of a narrow conducting strip," in *IEEE Transactions on Antennas and Propagation*, vol. 30, no. 4, pp. 755-758, July 1982, doi: 10.1109/TAP.1982.1142839.

[78] https://www.lpkf.com/en/industries-technologies/research-in-house-pcb-prototyping/produkte/lpkf-protomat-s104, accessed 31 March 2022.

[79] Wuerth Multilayer Chip-Balun transformer, 2400...2500 MHz 50 ohm, 0805 SMD 6-pin, 2004. [Online]. Available: https://de.rs-online.com/web/p/ chip-balun-ubertrager/8813217/, accessed 31 March 2022.

[80] https://www.wiegand-tec.de/home.html, accessed 31 March 2022.

[81] 'DE104 laminate and prepreg datasheet', http://www.isola-group.com/wp-content/uploads/DE104-Laminate-and-Prepreg-Data-Sheet-0317.pdf, accessed 14 July 2019.

[82] P. Kumar, G. Singh, S. Bhooshan and T. Chakravarty, "Gap-coupled microstrip antennna," Intl. Conf. on Comp. Intel. and Mult. Apps. (ICCIMA 2007), Sivakasi, Tamil Nadu, 2007, pp. 434-437.

[83] G. Kumar and K.C. Gupta, "Broad-band microstrip antennas using additional resonators gap-coupled to the radiating edges," in *IEEE Transactions on Antennas and Propagation*, vol. 32, no. 12, pp. 1375-1379, December 1984.

[84] G. Kumar and K.C. Gupta, "Nonradiating edges and four edges gap-coupled multiple resonator broad-band microstrip antennas," in *IEEE Transactions on Antennas and Propagation*, vol. 33, no. 2, pp. 173-178, February 1985.

[85] G. Kumar and K.C. Gupta, "Directly coupled multiple resonator wideband microstrip antenna," in *IEEE Transactions on Antennas and Propagation*, Vol. 33, pp. 588–593, June 1985.

[86] K. F. Lee, K. M. Luk and Hau Wah Lai, "Broadbanding techniques I - General principles, probe compensation, coplanar parasitic patches, stacked parasitic patches", in *Microstrip Patch Antennas*, 2^{nd} ed., Singapore: World Scientific Publishing, 2018, ch. 9, sec. 9.5, pp. 232-235.

[87] R. Garg, P. Bhartia, I. Bahl and Apisak Ittipiboon, "Broadbanding of microstrip antennas", in *Microstrip Antenna Design Handbook*, 1^{st} ed., Boston: Artech House, 2001, ch. 9, sec. 9.5.2, pp. 570-575.

[88] G. Kumar and K.P. Ray, "Planar Multiresonator Broadband MSAs", in *Broadband Microstrip Antennas*, 1^{st} ed., Boston: Artech House, 2003, ch. 3, pp. 89-127.

[89] S. Maci and G. B. Gentili, "Dual-frequency patch antennas", *IEEE Antennas and Propagation Magazine*, vol. 39, no. 6, pp. 13-20, Dec. 1997.

[90] J-S Chen and K-L Ray, "A Single-Layer Dual-Frequency Rectangular Microstrip Patch Antenna Using a Single Probe Feed", *Microwave and Optical Technology Letters*, vol. 11, Issue 2, pp. 83-84, 1996.

[91] G. Artner, R. Langwieser, C.F. Mecklenbräuker, "Concealed CFRP Vehicle Chassis Antenna Cavity", *IEEE Antennas and Wireless Propagation Letters*, vol. 16, pp. 1415-1418, 2017.

[92] G. Artner, W. Kotterman, G. D. Galdo and M. A. Hein, "Conformal Automotive Roof-Top Antenna Cavity With Increased Coverage to Vulnerable Road Users", *IEEE Antennas and Wireless Propagation Letters*, vol. 17, no. 12, pp. 2399-2403, Dec. 2018.

[93] K. Carver and J. Mink, "Microstrip antenna technology", in *IEEE Transactions on Antennas and Propagation*, vol. 29, no. 1, pp. 2-24, January 1981.

[94] J. Singh, R. Stephan and M. A. Hein, "Low-Profile Penta-Band Automotive Patch Antenna Using Horizontal Stacking and Corner Feeding," in *IEEE Access*, vol. 7, pp. 74198-74205, 2019, doi: 10.1109/ACCESS.2019.2919730.

[95] Victor Rabinovich, Nikolai Alexandrov and Basim Alkhateeb, "Automotive antennas overview: patents, papers, and products", in *Automotive Antenna Design and Applications*, 1^{st} ed., CRC Press, 2010, ch. 1, pp. 2.

[96] J. Singh, K. S. Alam, R. Stephan and M. A. Hein, "Metal Chassis Tolerant Conformal High Impedance Surface Based LTE-2600 Automotive Antenna," 2018 IEEE MTT-S International Conference on Microwaves for Intelligent Mobility (ICMIM), 2018, pp. 1-4, doi: 10.1109/ICMIM.2018.8443545.

[97] D. Sievenpiper et al., *High-Impedance Electromagnetic Surfaces with a Forbidden Frequency Band*, IEEE Transactions on Microwave Theory and Techniques, 1999.

[98] R. E. Diaz, J. T. Aberle and W. E. McKinzie, "TM mode analysis of a Sievenpiper high-impedance reactive surface," *IEEE Antennas and Propagation Society International Symposium. Transmitting Waves of Progress to the Next Millennium. 2000 Digest. Held in conjunction with: USNC/URSI National Radio Science Meeting* (C, 2000, pp. 327-330 vol.1, doi: 10.1109/APS.2000.873829.

[99] F. Yang, A. Aminian, and Y. Rahmat-Samii, "A novel surface wave antenna design using a thin periodically loaded ground plane," *Microwave Optical Tech. Lett.*, vol. 47, no. 3, 240–5, 2005

[100] Long Li et. al., "Surface-wave suppression band gap and plane-wave reflection phase band of mushroomlike photonic band gap structures", in *Journal of Applied Physics*, January 2008.

[101] Mario Schuhler et al., *Impedance Measurement of a Dipole Above a Periodically Structured Reflective Surface*, IEEE AWPL, 2008.

[102] A. Sanada, C. Caloz, T. Itoh, *Planar Distributed Structures With Negative Refractive Index*, IEEE Transactions on Microwave Theory and Techniques, 2004.

[103] Fan Yang and Y. Rahmat-Samii, "Reflection phase characterizations of the EBG ground plane for low profile wire antenna applications," in *IEEE Transactions on Antennas and Propagation*, vol. 51, no. 10, pp. 2691-2703, Oct. 2003, doi: 10.1109/TAP.2003.817559.

[104] Fan Yang and Y. Rahmat-Samii, "Low profile wire antennas on EBG ground plane", in *Electromagnetic Band Gap Structures in Antenna Engineering*, 1st ed., Cambridge University Press, 2009, ch. 6, pp. 158-161.

[105] M. F. Abedin and M. Ali, "Effects of EBG reflection phase profiles on the input impedance and bandwidth of ultrathin directional dipoles", in *IEEE Transactions on Antennas and Propagation*, vol. 53, no. 11, pp. 3664-3672, Nov. 2005, doi: 10.1109/TAP.2005.858584.

[106] VISTA. [online]. Available: http://www.mobilitaet-thueringen.de/, accessed 31 March 2022.

[107] Rohde & Schwarz CNW500. [online]. Available: https://www.rohde-schwarz.com/de/produkte/messtechnik/mobilfunktester-netzwerkemulator/rs-cmw500-wideband-radio-communication tester_63493-10844.html, accessed 05 May 2022.

[108] iperf. [online]. Available: https://iperf.fr/, accessed 05 May 2022.

[109] SISYVOS. [online] Available: https://www.tu-ilmenau.de/aktuelles/sisyvos-smarte-integrierte-funksysteme-fuer-vernetzte-mobilitaet-und-logistik, accessed: 05 May 2022.

[110] Bernhard Schulz, "Testing LTE-A Releases 11 and 12", Rohde & Schwarz, 2019 [online]. Available: https://scdn.rohde-schwarz.com/ur/pws dl_downloads/dl_application/application_notes 1ma272/1MA272_2e_Testing_LTE_Rel_11_12.pdf, accessed: 16 May 2022.

[111] Chiumento, A., Bennis, M., Desset, C. et al. Adaptive CSI and feedback estimation in LTE and beyond: a Gaussian process regression approach. *J Wireless Com Network 2015*, 168 (2015). https://doi.org/10.1186/s13638-015-0388-0

[112] H. Chayon, K. Dimyati, H. Ramiah, and A. Reza, "Enhanced Quality of Service of Cell-Edge User by Extending Modified Largest Weighted Delay First Algorithm in LTE Networks," Symmetry, vol. 9, no. 6, p. 81, May 2017, doi: 10.3390/sym9060081.

[113] O. Liberg, M. Sundberg et. al., "NB-IoT", in *Cellular Internet of Things*, 1st ed., Elsevier, 2018, ch. 7, pp. 230.

[114] O. Liberg, M. Sundberg et. al., "LTE-M", in *Cellular Internet of Things*, 1st ed., Elsevier, 2018, ch. 5, pp. 141.

[115] Jerry R. Hampton, "Practical MIMO examples", in *Introduction to MIMO communications*, 1^{st} ed., Cambridge University Press, 2014, ch. 11, pp. 260-263.

[116] Huawei E8372 USB LTE model. [online]. Available: https://consumer.huawei.com/en/routers/e8372/, accessed: 05 May 2022.

[117] Bernhard Schulz, "LTE Transmission Modes and Beamforming", Rohde & Schwarz, July 2015 [online]. Available: https://cdn.rohde-schwarz.com/pws/dl_downloads/dl_application/application_notes 1ma186/1MA186_2e_LTE_TMs_and_beamforming.pdf, accessed: 16 May 2022.

[118] Antennentechnik Bad Blankenburg. [online]. Available: https://www.attb.de/, accessed 31 March 2022.

[119] S. Zhu et al., "Probability Distribution of Rician *K*-Factor in Urban, Suburban and Rural Areas Using Real-World Captured Data," in *IEEE Transactions on Antennas and Propagation*, vol. 62, no. 7, pp. 3835-3839, July 2014, doi: 10.1109/TAP.2014.2318072.

[120] J. Singh, B. Altinel, C. Bornkessel, R. Stephan and M. A. Hein, "V2V communication performance of conformal plastic-embedded side-mount antennas investigated with field-operational tests," *2021 IEEE 93rd Vehicular Technology Conference (VTC2021-Spring)*, 2021, pp. 1-5, doi: 10.1109/VTC2021-Spring51267.2021.9448811.

[121] Adrian Posselt, "Design and Analysis of Multi-Element Antenna Systems and Agile Radiofrequency Frontends for Automotive Applications", Ph. D dissertation, Leibniz Universitaet Hannover, 2019. [online]. Available: https://www.tu-ilmenau.de/fileadmin/Bereiche/EI/1_Fak_EI/dokumente/PRO-AB-aend_10_Lesefassung.pdf

[122] Harri Holma, Antti Toskala, and Takehiro Nakamura, "Introduction", in *5G Technology: 3GPP New Radio*, 1st ed., Wiley, 2020, ch. 1, pp. 3-6.

[123] Aman Kumar Gulia, "A Simulation Study on the Performance Comparison of the V2X Communication Systems: ITS-G5 and C-V2X", Master Thesis, School of Electrical Engineering and Computer Science, KTH Royal Institute of Technology, February 2020.

[124] Andrew Turley, Kees Moerman et. al., "C-ITS: Three observations on LTE-V2X and ETSI ITS-G5-A comparison", NXP, 2018 [online]. Available: https://www.nxp.com/docs/en/white-paper/CITSCOMPWP.pdf, accessed: 12 June 2022.

[125] 5GAA Timeline for deployment of C-V2X – Update. [online]. Available: https://5gaa.org/wp-content/uploads/2019/01/5GAA_White-Paper-CV2X-Roadmap.pdf, accessed: 12 June 2022.

[126] R. King and C. W. Harrison, "The Distribution of Current along a Symmetrical Center-Driven Antenna," in *Proceedings of the IRE*, vol. 31, no. 10, pp. 548-567, Oct. 1943, doi: 10.1109/JRPROC.1943.233034.

[127] J.D. Kraus, "Self and mutual impedance", in *Antennas For All Applications*, 2nd ed., McGraw-Hill, 1988, ch. 10, pp. 411-428.

[128] Fan Yang and Y. Rahmat-Samii, "EBG characterizations and classifications," in *Electromagnetic Band Gap Structures in Antenna Engineering*, 1st ed., Cambridge University Press, 2009, ch. 3, pp. 70-74.

[129] A. Asgharzadeh, J. Singh, P. Hofmann, G. Reichert and M. A. Hein, "Design approach towards automotive FM broadcast antennas based on characteristic modes," *2017 IEEE-APS Topical Conference on Antennas and Propagation in Wireless Communications (APWC)*, 2017, pp. 57-60, doi: 10.1109/APWC.2017.8062240.